New-Generation Hyperspectral Sensors Improve Crop Characterization
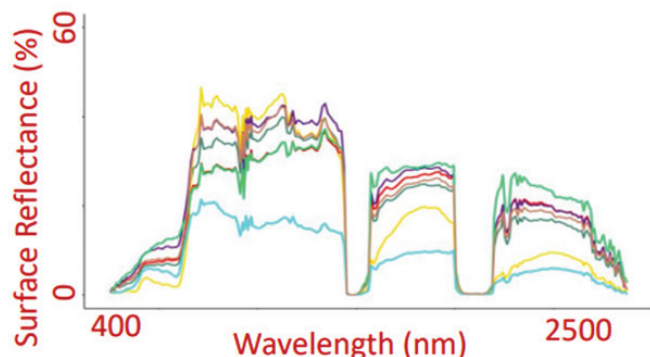
Figure 1. Crop Types for PRISMA
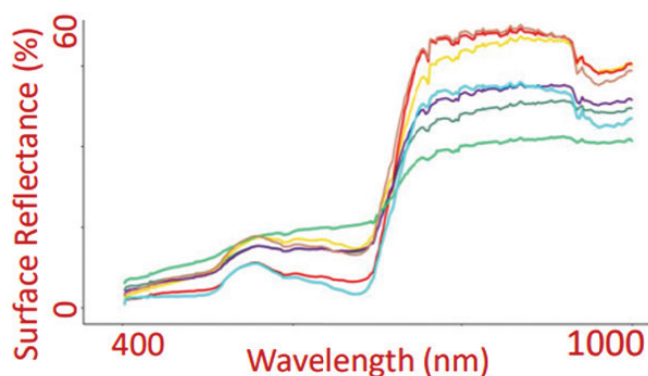

Figure 2. Crop Types for DESIS
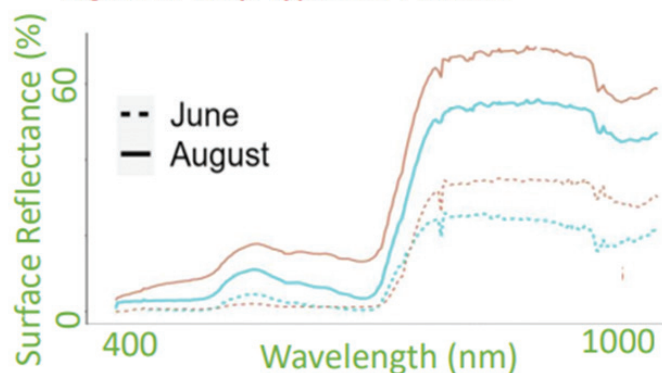

Figure 3. Crop Growth Stages for DESIS

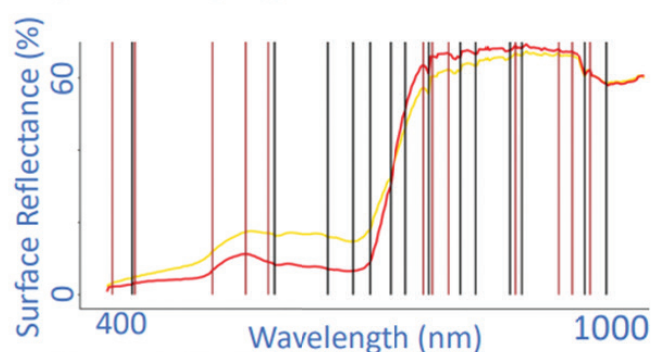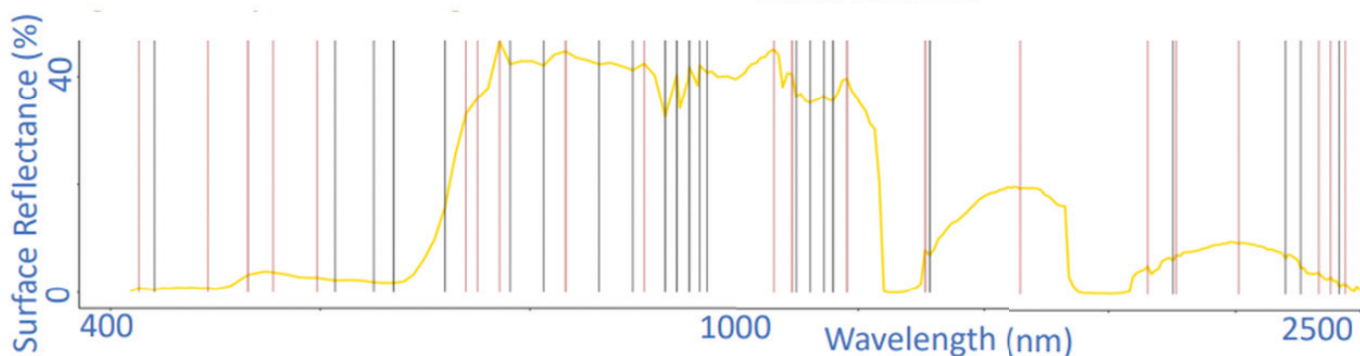**Figure 4. Optimal Hyperspectral Narrow Bands for DESIS**

Figure 5. Optimal Hyperspectral Narrow Bands for PRISMA

Almonds
Corn
Cotton
Grapes
Pistachios
Rice
Tomatoes

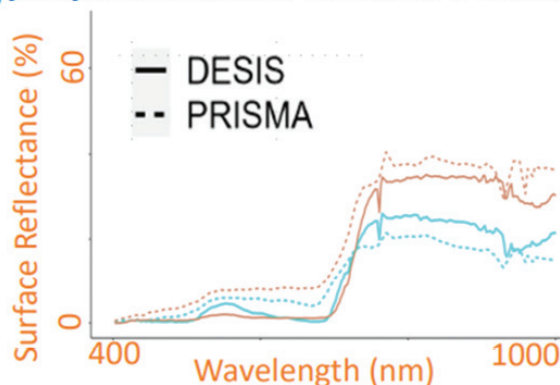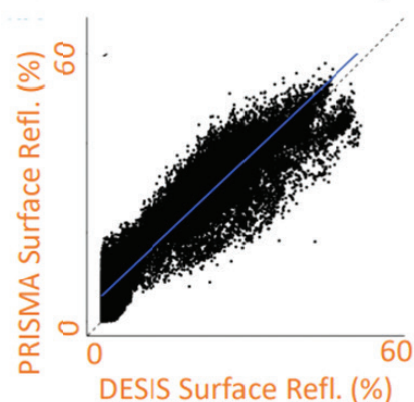**Figure 6. Spectral matching**

Figure 7. Correlation analysis

Digital Elevation Model Technologies and Applications:
The DEM Users Manual, 3rd Edition

Edited by David F. Maune, PhD, CP
and Amar Nayegandhi, CP, CMS

**To order, visit
https://www.asprs.org/dem**

The 3rd edition of the DEM Users Manual includes 15 chapters and three appendices. References in the eBook version are hyperlinked. Chapter and appendix titles include:

1. Introduction to DEMs
   David F. Maune, Hans Karl Heidemann, Stephen M. Kopp, and Clayton A. Crawford

2. Vertical Datums
   Dru Smith

3. Standards, Guidelines & Specifications
   David F. Maune

4. The National Elevation Dataset (NED)
   Dean B. Gesch, Gayla A. Evans, Michael J. Oimoen, and Samantha T. Arundel

5. The 3D Elevation Program (3DEP)
   Jason M. Stoker, Vicki Lukas, Allyson L. Jason, Diane F. Eldridge, and Larry J. Sugarbaker

6. Photogrammetry
   J. Chris McGlone and Scott Arko

7. IfSAR
   Scott Hensley and Lorraine Tighe

8. Airborne Topographic Lidar
   Amar Nayegandhi and Joshua Nimetz

9. Lidar Data Processing
   Joshua M. Novac

10. Airborne Lidar Bathymetry
    Jennifer Wozencraft and Amar Nayegandhi

11. Sonar
    Guy T. Noll and Douglas Lockhart

12. Enabling Technologies
    Bruno M. Scherzinger, Joseph J. Hutton, and Mohamed M.R. Mostafa

13. DEM User Applications
    David F. Maune

14. DEM User Requirements & Benefits
    David F. Maune

15. Quality Assessment of Elevation Data
    Jennifer Novac

    Appendix A. Acronyms

    Appendix B. Definitions

    Appendix C. Sample Datasets

This book is your guide to 3D elevation technologies, products and applications. It will guide you through the inception and implementation of the U.S. Geological Survey's (USGS) 3D Elevation Program (3DEP) to provide not just bare earth DEMs, but a full suite of 3D elevation products using Quality Levels (QLs) that are standardized and consistent across the U.S. and territories. The 3DEP is based on the National Enhanced Elevation Assessment (NEEA) which evaluated 602 different mission-critical requirements for and benefits from enhanced elevation data of various QLs for 34 Federal agencies, all 50 states (with local and Tribal input), and 13 non-governmental organizations.

The NEEA documented the highest Return on Investment from QL2 lidar for the conterminous states, Hawaii and U.S. territories, and QL5 IfSAR for Alaska.

Chapters 3, 5, 8, 9, 13, 14, and 15 are "must-read" chapters for users and providers of topographic lidar data. Chapter 8 addresses linear mode, single photon and Geiger mode lidar technologies, and Chapter 10 addresses the latest in topo-bathymetric lidar. The remaining chapters are either relevant to all DEM technologies or address alternative technologies including photogrammetry, IfSAR, and sonar.

As demonstrated by the figures selected for the front cover of this manual, readers will recognize the editors' vision for the future – a 3D Nation that seamlessly merges topographic and bathymetric data from the tops of the mountains, beneath rivers and lakes, to the depths of the sea.

Co-Editors

David F. Maune, PhD, CP and
Amar Nayegandhi, CP, CMS

PRICING

Student (must submit copy of Student ID)	$50 +S&H
ASPRS Member	$80 +S&H
Non-member	$100 +S&H
E-Book (only available in the Amazon Kindle store)	$85

To have your press release published in *PE&RS*, contact Rae Kelley, rkelley@asprs.org.

INDUSTRYNEWS

ANNOUNCEMENTS

URISA is pleased to announce the newest members of its Vanguard Cabinet. The Vanguard Cabinet (VC) is a URISA initiative (which debuted in 2011) to engage young GIS practitioners, increase their numbers in the organization, and better understand the concerns facing these future leaders of the GIS community. The VC is an advisory board who represent the young membership of the organization. The Cabinet's mission is to collaborate with URISA's Board of Directors and Committees in creating and promoting programs and policies of benefit to young professionals.

Comprised entirely of passionate young members selected from different geospatial disciplines, the Cabinet aims to position URISA as the center of opportunities for ambitious young professionals who are committed to improving URISA and the geospatial profession via innovation, collaboration, networking, and professional development. Each will serve a three-year term. 2023-2025 URISA Vanguard Cabinet Members:

- Andrew Berens, GISP, Senior GIS Projects Coordinator, Peraton at CDC/ATSDR, Baton Rouge, Louisiana
- Kelsey Calvez, Environmental Scientist /GIS Analyst, Freese and Nichols, Inc., Austin, Texas
- Samantha "Sam" Dinning, GIS Analyst, Douglas County, Castle Rock, Colorado
- Brooke Hatcher, Senior Geospatial Consultant, New Light Technologies, Seattle, Washington
- Wanmei Liang, GIS Technician, Infrastructure Management Services, Los Angeles, California
- Ethan McGhee, GIS Specialist, City of San Luis Obispo, San Luis Obispo, California
- Matt Worthy, Program Manager, Optimal GEO, Huntsville, Alabama
- Sydney Young, GIS Technician, Chatham County Engineering Department, Savannah, Georgia

Cabinet members are selected through an application process, with interviews by the URISA Leadership Development Committee. The application process for the next class of Vanguard Cabinet members will open during the Summer of 2023. Learn more about VC activities here: https://www.urisa.org/vanguardcabinet.

‾‿‾

Phase One, a leading developer of digital imaging technologies, has announced the successful launch and orbital deployment of an imaging sensor based on the Phase One iXM Series 150MP frame camera. Launched into low Earth orbit (LEO) earlier this year by a U.S. customer, the Phase One sensor system is performing as planned aboard a smallsat Earth observation mission.

"With our first sensor now in orbit, Phase One is pleased to announce the commercial release of a space-hardened camera system designed specifically for satellite-based Earth observation programs," said Dov Kalinski, Phase One Vice President of Security & Space. "The new imaging system will be available shortly."

The Phase One iXM Series is a commercial off-the-shelf (COTS) 150-megapixel camera commonly used for high-demand mapping in the globally deployed line of Phase One aerial imaging systems.

The client selected the Phase One camera for its groundbreaking technology. With a single large-format CMOS sensor composed of 3.76 micron pixels, the iXM camera provides high-resolution imagery over a large field of view. The Phase One camera system is available for a fraction of the cost of traditional satellite imaging sensors, allowing the client to obtain and integrate the iXM Series sensor within the aggressive schedule required by the mission.

For more information, visit www.phaseone.com.

ACCOMPLISHMENTS

Leica Geosystems, part of Hexagon, is pleased to announce that the Carl Pulfrich Award 2022 has been presented to Prof. Dr. Charles Toth for his outstanding contribution in the field of geospatial science and engineering. The Carl Pulfrich Award honours cutting-edge innovations and developments in geodesy, photogrammetry and Earth sciences.

"I am deeply grateful to receive the Carl Pulfrich Award among so many notable nominees and to join a distinguished group of prior recipients. This accomplishment is a significant milestone in my professional life, and I want to express my heartfelt gratitude to the team who selected me to receive this award," said Dr. Toth.

The seven-member jury selected Toth out of a number of qualified nominations. Toth works as a research professor at the Department of Civil, Environmental and Geodetic Engineering at the Ohio State University, United States.

Toth was born in Hungary, where he earned his Master of Science and PhD degrees in electrical engineering from the Technical University of Budapest in 1977 and 1980, respectively. In 1997, he completed his second PhD at the same university in geoinformation sciences. Toth has made several significant contributions to geospatial science and engineering. Most importantly, he is known worldwide for his visionary advancements to mobile mapping, and his seminal contributions to research in sensor georeferencing and digital imaging technologies. Publishing more than 400 journal and conference papers, and several book chapters, Toth has an outstanding scholarly record. He also received numerous awards, including the 2009 APSRS Photogrammetric Award, 2005 and 2015 United States Geospatial Intelligence Foundation Academic Achievement Award, the 2016 ISPRS Schwidefsky Medal, Ohio State College of Engineering Lumley Research Awards, and various best papers awards.

The chairman of the 2022 jury, Prof. Dr.-Ing. Uwe Sörgel says, "I am pleased about the recognition of the important work of Prof. Dr. Charles Toth in the fields of photogrammetry, laser scanning and mobile mapping. He has made major contributions to the geospatial industry and academia. In addition, he has served our scientific community for many years in leadership positions of the ASPRS and the ISPRS." The tribute was given at the Carl Pulfrich Award Ceremony 2022 during the Photogrammetric Week at the University of Stuttgart.

The academic Earth imaging community was encouraged to submit nominations for the biennial award. Nominees were considered based on their experience in photogrammetry, remote sensing activities and contributions to advancing all aspects of the Earth imaging field. Applied work involving hardware systems, software solutions or innovative service activities was also considered.
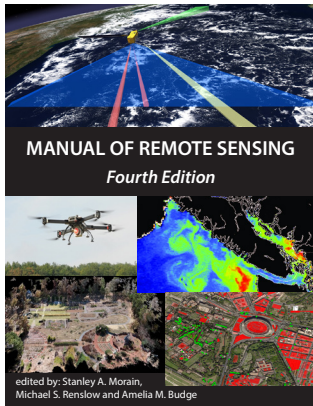
The Carl Pulfrich Award is prestigious for recognizing cutting-edge innovations, hardware and software developments, and integrated systems design in geodesy, photogrammetry and the Earth sciences. Launched in 1968, it is announced biennially and attracts nominations and recommendations for candidates from all over the world. The biennial award honors the memory of Dr. Carl Pulfrich, a scientific staff member at Carl Zeiss from 1890 to 1927. During his tenure, Pulfrich directed the design of the first stereo photogrammetric and surveying instruments from Zeiss. Initially launched by Carl Zeiss, Oberkochen, then relaunched by Z/I Imaging and Intergraph, it was adopted by Leica Geosystems in 2011. For more than four decades, the Carl Pulfrich Award has recognised the many contributions of scientists worldwide.

CALENDAR

- 6-9 February 2023, Coastal GeoTools, Charleston, South Carolina. For more information, visit https://coastalgeotools.org.

677
Digital Twins
Key to 21st-Century City Planning and Operations, Smart City Evolution
By Qassim Abdullah, Ph.D., CP, PLS,
Woolpert Vice President and Chief Scientist

See the Cover Description on Page 676

facebook.com/ASPRS.org   linkedin.com/groups/2745128   twitter.com/ASPRSorg   youtube.com/user/ASPRS

COVER DESCRIPTION

Using the California Central Valley as an example, the cover depicts how data from two new-generation spaceborne hyperspectral sensors, PRISMA and DESIS, were used to study agricultural crops. The figures illustrate hyperspectral agricultural crop characteristics of seven major world crops derived from: 1. the Italian ASI's PRISMA (400-2500 nm), launched in 2019, acquiring data in 238 hyperspectral narrowbands (HNBs), and 2. the German DLR's DESIS (400-1000 nm), launched in 2018 and onboard the International Space Station (ISS), acquiring data in 235 bands. Hyperspectral signatures of the same crops for the 2020 growing season are illustrated for PRISMA (Figure 1) and DESIS (Figure 2). Similarly, crop growth stages for crops in different growth stages, collected at different months within the growing season are shown in Figure 3. The optimal HNBs in the study of agricultural crops for DESIS (Figure 4) and PRISMA (Figure 5) were established in this study. Comparisons of spectral signatures derived from DESIS and PRISMA, in the 400-1000 nm range, are illustrated through spectral matching (Figure 6), and correlation analysis (Figure 7). Spectral data used in this study are available at: https://www.sciencebase.gov/catalog/item/62a91cc2d34ec53d2770f06d

For details read the article by Itiya Aneece and Prasad Thenkabail in this issue.

Cover page credits: Dr. Itiya Aneece and Dr. Prasad S. Thenkabail, U.S. Geological Survey (USGS).

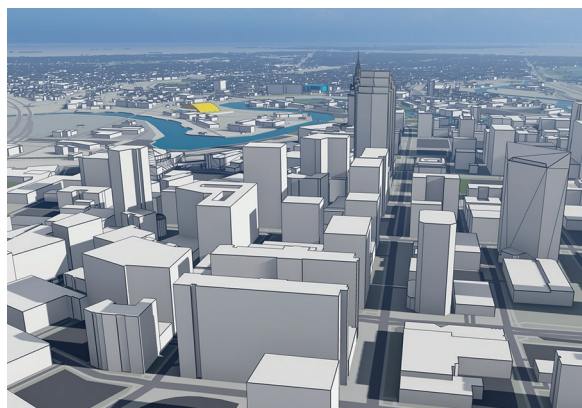Contact: ianeece@usgs.gov; pthenkabail@usgs.gov or thenkabail@gmail.com.

DIGITAL TWINS

KEY TO 21ST-CENTURY CITY PLANNING AND OPERATIONS, SMART CITY EVOLUTION

By Qassim Abdullah, Ph.D., CP, PLS
Woolpert Vice President and Chief Scientist

The concept of the digital twin originated in the manufacturing industry around 2002, and it has been gaining momentum in the geospatial industry since around 2016. Digital twin and 3D models are often confused because they are both virtual representations of the physical environment. The digital twin however, distinguishes itself from the static 3D model by its ability to incorporate data and information from other systems and to evolve over time to support all facets of an asset or ecosystem, from planning through operations.

Because of this dynamic capability, digital twin applications have reproduced quickly over the last handful of years, with industries from manufacturing to supply chain to health care capitalizing on the value of this geospatial tool. But one of the most promising applications is as multifaceted as the concept itself: city planning and management.

According to a recent report by Guidehouse Insights, a global technology consultancy, due to relatively low costs and high utilities, the incorporation and benefits from municipal digital twins are expected to grow immensely over the next decade. The group estimates that revenue generated from digital twins will rise from more than $331 million in 2022 to $2.5 billion by 2031, representing an annual growth rate of more than 25%. The primary limiting factor to this growth is expected to be lack of knowledge about the technology and its applications.

That's where we come in.

DIGITAL TWINS, 3D MODELING AND SMART CITIES

Digital twins and 3D models have contrasting applications in a city setting. It is the difference between a highway overpass model and a digital and dynamic replication of a highway. A 3D model is the best platform for presenting a realistic environment for the interpretation of integrated data. That model then provides the base that can be fed architecture and engineering designs, real-time environmental measurements, and daily operation data to make it a living, breathing digital twin.

Immense amounts of data are collected daily by local, state and federal agencies to support the planning and operations of cities. These data support infrastructure, water and sewer services; energy and utilities; transportation; property management; health care; social services; education; parks and recreation; police and rescue; etc.—pretty much everything that contributes to city facilities and functions.

In most cities, each of these databases are siloed. If those databases are integrated into a digital twin, city officials gain access across city departments to make individual and
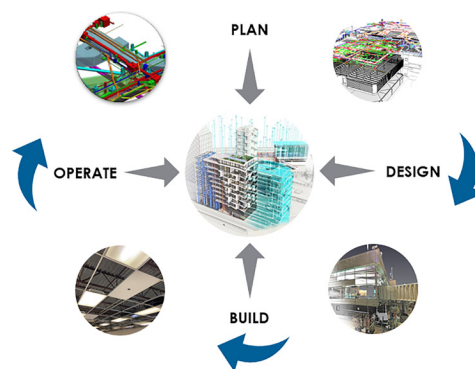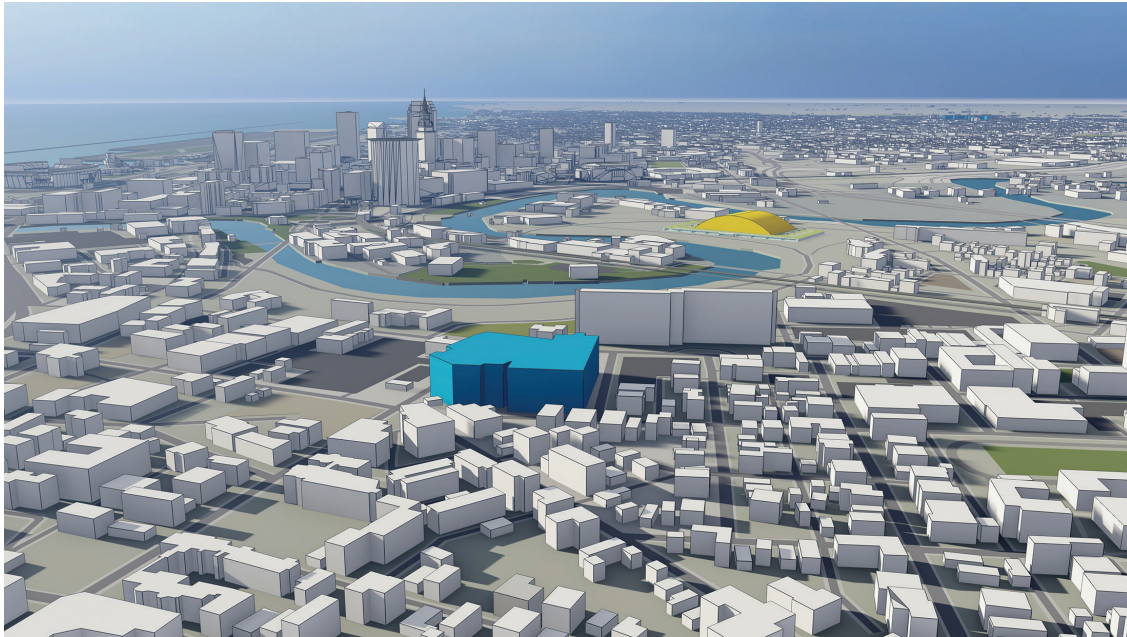
collaborative decisions. This not only helps realize synergies to advance each department and service, but it provides the framework to identify opportunities to improve that city's overall operations, research, planning, resilience and emergency response.

Although a digital twin can be created without it, building information modeling (BIM) plays an integral role in creating an accurate digital twin for industrial facilities and the urban environment. BIM is a collaborative work method for structuring and managing assets by utilizing data accrued throughout each asset's life cycle. BIM employs augmented and virtual reality to envision a project so changes can be discussed, and next steps can be determined. The integration of data sources from multiple BIM sources, alongside other data and information accrued, creates a digital twin that increases access to that information, forging connections for improved and defensible decision-making.

Specific to a municipal digital twin, BIM is essential. Every city structure represented in that BIM should include a complete development history, from planning to construction to operations, before it is added to the digital twin to accurately reflect those assets within the virtual environment.

The implementation of a digital twin is highlighted in the goal of a smart city, which is to use digitally managed infrastructure to achieve a more sustainable and livable municipality. This is accomplished by improving the quality of life of citizens by ensuring that available resources are functioning correctly and are utilized efficiently. The real-time, integrated data of the digital twin enables that city to optimally manage and operate its assets. The combination of these concepts can effectively serve current city development projects, informing data-rich multidisciplinary models to manage valuable resources through visualization and analytical modeling.

CITY APPLICATIONS, ROI

Due to the readily available municipal data and the adoption of evolving technologies around the world, city GIS and IT managers have been taking the lead on the integration and management of these data. Many cities are building 3D models with increased dimension and detail, including the integration of building interiors. These models are supported by the current capabilities of the geospatial industry, including high-accuracy and high-resolution lidar data and imagery that are acquired, from satellite to drone. These city models represent a cornerstone for the municipal digital twin, enhancing shared information among all levels of governments to address traditional and emerging municipal issues.

According to experts in the field, roughly 70% of the return on the digital twin investment comes from facility operation and management after construction is completed because it supports the life cycle of the project. This digital access to the physical structure is then extended and shared with city and departmental managers. While an economic development officer will want to know how many people live in a building, the fire marshal will want to know immediately where his crew can find access to those people, the utility company will want to know how those people are utilizing various energy resources to support grid reliability, etc. A digital twin combined with artificial intelligence can provide a city's engineering and maintenance team with an early warning about a routine maintenance schedule and can warn the team of a defect in any segment of the utilities network.

Correct digital twin implementation requires a massive investment in digital twin infrastructure, data governance, stakeholders' coordination and collaboration, through agreed upon frameworks and processes. It also changes workflows and requires the work force to gain new skills. The continuing drop in the cost of IT infrastructure coupled with affordable cloud data storage and processing will contribute to the affordability of the digital twin, as will the fact that costs associated with the technology can be shared across departments. Additional savings can be realized by reducing physical security and maintenance personnel.

A mature digital twin platform can be extended to connect the wider community of citizens with their government using smart city concepts. Citizens can login to the platform to learn about health and environmental issues and regulations, review their energy use and how it compares to the neighborhood usage, check in on city development plans and how they affect their neighborhoods, etc. You may have noticed here, much of this citizen interaction happens through a smart hub, representing elements of a smart city that are encompassed within the digital twin ecosystem.

As its benefits are more widely understood, the application of digital twins will continue to expand and improve the management of assets in multiple environments. The geospatial industry expects increasing demand for these technologies and the corresponding opportunities they present. The geospatial industry needs to pay close attention to forthcoming opportunities in the digital twin market for multiple reasons:

- Geospatial data and information are critical enablers for smart cities and therefore digital twins.
- Geospatial data and information form the framework for the digital infrastructure needed for digital twin implementation.
- Digital twins do not exist in isolation; they exist in an ecosystem of systems that are interconnected and interwoven. Many of these interconnected systems are based on geospatial data components.

In addition to AI and deep learning, data analytics and modeling fields will prosper from the tremendous amount of data generated from operating an asset within a digital twin that needs to be converted to knowledge.

We need to continue to expand these technologies and advance their applications, while educating those who can most benefit. As the Guidehouse Insights study noted, the learning curve is the biggest impediment to municipal digital twin technology and applications. It is our job to fix that.

###

This article is also being published in Lidar Magazine.

GIS
Tips & Tricks

Al Karlin, Ph.D. CMS-L, GISP

Need a special GIS Tool? Here are some options.

INTRODUCTION

No matter whether you are a GIS-newbie or a seasoned professional, there will come a time when you search through the hundreds of GIS tools in whatever GIS software you are using, whether it is one of the Esri packages, QGIS, GlobalMapper, etc., and just not find the right tool to do what you need done. Of course, if you are a newbie it might just be that you don't know the name of the tool to enter into your search engine, but sometimes, the tool is simply not available. So… what to do? Believe it or not, you have options.

Three options come to mind;

Option 1 – Buy the tools from a commercial off the shelf (COTS) ready-made GIS package, or

Option 2 – Find the tool in an open-source (or shareware) toolkit; don't forget… GOOGLE knows everything, and

Option 3 – Make it yourself.

So, your finances and/or programming skillset are the limiting factors to getting the GIS tool.

This month's tip provides some details on these options. (*The tools identified below are not to be taken as endorsements, personal recommendations, or even a complete listing of those available.*)

So… here are a few starting places when you need a GIS tool:

OPTION 1 – BUY THE TOOL

If you are an Esri ArcGIS Desktop or ArcGIS Pro user, you have already purchase over 25 Toolboxes; the Spatial Analyst toolbox alone contains over 200 tools. So, it may be a daunting task just to know what tool is located where, even with the Geoprocessing "Search" in Desktop and the Find Tools in ArcGIS Pro that I discussed in the April 2022 column. If you still want more help finding the tools that you already own, there are "Cheat Sheets" available for free (http://s3.amazonaws.com/arena-attachments/1483540/1e582e391e6e24ae34754e36210b03a4.pdf?1512435403) that may provide some clues. Also, there are additional toolsets that are available for purchase from the Esri MarketPlace (https://www.esri.com/arcgis-blog/products/arcgis-pro-net/announcements/arcgis-pro-add-ins-on-the-arcgis-marketplace/.)

Probably the most popular COTS toolkit, XTools (https://xtools.pro/), is available for both ArcGIS Desktop and ArcGIS Pro. Licensing is available in both "you own it" and "annual subscription" modes. This package is advertised as a "Productivity Package" with over 100 additional tools for ArcGIS users. A listing of the tools and their functions is available on the website.

Then, of course, there are multiple COTS GIS software packages. Here is a raking of the top 30 GIS software packages (https://gisgeography.com/best-gis-software/) with links to their websites. Most of the COTS options include a "try before you buy" option, so you can "try" the tool, albeit with limited functionality, to see if it is the right one for you.

OPTION 2 – FIND THE TOOL

If you are looking for a "Free" or "ShareWare" option, a good start would be to search through the Wikipedia listing of GIS packages (https://en.wikipedia.org/wiki/List_of_spatial_analysis_software). While this listing is not all-inclusive, it does contain the major

options, availability, and their dependencies. Many tools are "free" but require ArcGIS (not free), so this is a case of user-beware.

While discussing ShareWare and OpenSource, do not forget that the entire GRASS and SAGA toolsets are included with the QGIS distributions along with options for over 1100 additional tools. You may need to activate/manage the tools/plugins using the Plugins Manager (Figure 1) in QGIS. Warnings: (1) With over 1100 plugins available, you can install one, select multiples, or there is an option to install all of them, so be careful, (2) some plugins are identified as "experimental" as in Figure 1, so you may get unexpected results, and (3) I have found that some combinations of tools
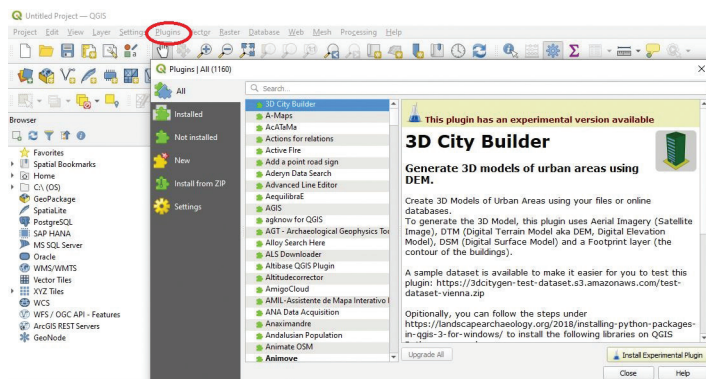
Figure 1. QGIS Plugin Manager. Note that some plugins are identified as "experimental".

result in interference, cause the software to crash and will require a complete re-installation without the plugins.

A complete list of all QGIS plugins can be viewed and downloaded at the QGIS Pythons Plugins Respository (https://plugins.qgis.org/plugins). This repository contains all previous and new plugins, as in this example in Figure 2 below which was uploaded just recently as of this writing.

There are several toolkits that come as pre-packaged Esri Toolboxes and stand-alone tools. The WhiteBox Geospatial Analysis tools (https://www.whiteboxgeo.com/) from the University of Guelph's Geomorphonmetry and Hydrogeomatics Research Group are an open-source platform containing over 500 tools. The tools can be downloaded (user contribution encouraged but not required) as a basic or extended (donation required) toolset. The ready-packaged ArcGIS toolbox is found at Github (https://github.com/giswqs/WhiteboxTools-ArcGIS) and a similar toolbox for QGIS versions 3 and above is found at the Plugins Repository (https://plugins.qgis.org/plugins/wbt_for_qgis/) sited above .

Figure 2. A new QGIS plugin available on the QGIS Plugin Respository website.

OPTION 3 - MAKE THE TOOL

Depending on your programming skills, constructing the tool yourself may be an option. For Esri users, if your need is a workflow-tool, you may be able to use ModelBuilder in either Desktop or Pro to construct a custom workflow using Toolbox components. Jupyter Notebooks, (https://www.dataquest.io/blog/jupyter-notebook-tutorial/) used for developing and presenting data science projects, have also proven valuable for GIS workflows and data development. Jupyter Notebooks can make use of exposed Esri, GRASS and SAGA tools and there are several Guides, Tutorials and YouTubes available. Just use GOOGLE!

When all else fails, there are multiple programming languages available to build your own tool, but Python and R are probably the most popular, especially as they work well in combination with Jupyter Notebooks.

Python: There are several spatially compatible programming tools available for those proficient in programming. Perhaps the most readily available library for Python. Python GIS Libraries can be found at: https://gisgeography.com/python-libraries-gis-mapping/ and of course, a wealth of information for Esri ArcPy at: https://www.esri.com/en-us/arcgis/products/arcgis-python-libraries/overview. Hint: Included with the "Help" for each Esri tool, you can find the Python code that you can copy/paste for your use. There are lots of Python tutorials on the web, just GOOGLE "Python GIS Tutorial" to find them.

R: Another spatially aware programing packages are the "R" and "RStudio" libraries. As with Python, these libraries are opensource, robust and come with lots of web support (https://gisgeography.com/r-programming-gis/) and tutorials. R contains an expansive list of over 45 packages for spatial analysis (https://www.gislounge.com/r-packages-for-spatial-analysis/) and, like Python, works well in Jupyter Notebooks and has robust support, tutorials and YouTube videos.

These tips are just starters and are not meant to be inclusive. But when you need a tool and don't know where to start, these are all good places.

A special thanks to James Parker, GISP, PMP (Senior Project Manager, Dewberry) and Colin Flynn (GIS Developer, Dewberry) for their input on Option 3 – Make the Tool.

GRIDS & DATUMS

BY Clifford J. Mugnier, CP, CMS, FASPRS

INDEPENDENT STATE OF PAPUA NEW GUINEA

The Grids & Datums column has completed an exploration of every country on the Earth. For those who did not get to enjoy this world tour the first time, *PE&RS* is reprinting prior articles from the column. This month's article on Independent State of Papua New Guinea was originally printed in 2005 but contains updates to their coordinate system since then.

During the 16th century, Portuguese and Spanish navigators visited the island. Annexed by Queensland in 1883, the region became a British Protectorate in 1884 and was annexed by Great Britain in 1888 as British New Guinea. Administration was passed to Australia in 1905, and the name was changed to the Territory of Papua. In 1949, it was united with the Territory of New Guinea to form Papua New Guinea.

The Independent State of Papua New Guinea became independent in 1975. The country is comprised of the Eastern part of New Guinea, the island of Bougainville, and the Bismarck Archipelago: a total area of 462,840 km² which is slightly larger than the State of California. The land area totals 820 km² and is mostly mountains with coastal lowlands and rolling foothills. The lowest point is the Pacific Ocean, and the highest point is Mount Wilhelm (4,509 m). According to the *CIA Factbook*, the "natural hazards include active volcanism; situated along the Pacific 'Ring of Fire'; the country is subject to frequent and sometimes severe earthquakes; mud slides; tsunamis. On 18 July 1998, a tsunami took the lives of 2,200 north shore residents of Papua New Guinea.

The first Australian Engineer Officer for mapping was posted to Rabaul on New Britain in 1914. Topographic mapping of the area began during World War II, and consisted mainly of one inch to the mile compilations with classical triangulation control. The Australian military mapping installations consisted of drafting and computation sections quartered in tents. Map printing services in Queensland were transferred to the U.S. Army 69th Engineer Topographic Battalion's lithographic detachment in Port Moresby. Supplemented by reconnaissance aerial photo mosaics, additional mapping control continued through the 1950s with assistance from the Royal Australian Survey Corps and the U.S. Army (Australia's Military Map-Makers, 2000).

The oldest "Astro station" serving as a local datum is Paga Hill 1939 near Port Moresby where: $\Phi_O = 9°\ 29'\ 00.31"$ S, $\Lambda_O = 147°\ 08'\ 21.66"$ E of Greenwich, and the ellipsoid of reference is the Bessel 1841 where: $a = 6,378,397.155$ m., and $1/f = 299.1528$. The grid system commonly associated with the Paga Hill Datum of 1939 is the 1943 Southern New Guinea Lambert Zone where the Latitude of Origin, $\varphi_O = 8°$ S, Central Meridian, $\lambda_O = 150°$ E, Scale Factor at Origin, $m_O = 0.9997$, False Northing = 1,000 km, False Easting = 3,000 km. The original limits of the Zone were for the North: Parallel of 7° S, east to 153° 30' E, thence north along this meridian to 5° S, thence east along this parallel to 165° E. East: Meridian of 165° E. South: Parallel of 12° S, west to 145° E, thence west along this parallel to 141° E, thence south along this meridian to 11° S, thence west along this parallel to 137° E. West: Meridian of 137° E. Recent source data for Paga Hill Datum of 1939 now state the ellipsoid of reference as: International 1924 where: $a = 6,378,388$ m and $1/f = 297$. When this supposed change occurred is unknown.

Thanks to John W. Hager for the following: other astro positions in Papua New Guinea include: Brown Island, East New Britain Province $\Phi_O = 5°\ 01'\ 40"$ S, $\Lambda_O = 151°\ 58'\ 54"$ E; Cay, Panaeati & Deboyne Island, Milne Bay Province $\Phi_O = 14°\ 41'$ S, $\Lambda_O = 152°\ 22'$ E; Dedele Point, Central Province $\Phi_O = 10°\ 14'$ S, $\Lambda_O = 148°\ 45'$ E; Dobodura Astro Fix, Northern Province, $\Phi_O = 8°\ 45'\ 50.13"$ S, $\Lambda_O = 148°\ 22'\ 38.8"$ E; Dumpu. Madang Province, $\Phi_O = 5°\ 50'\ 34.4"$ S, $\Lambda_O = 145°\ 44'\ 29.55"$ E; Guadagasal Astro Fix, Gulf Province, $\Phi_O = 7°\ 15'\ 33.6"$ S, $\Lambda_O = 146°\ 58'\ 42.0$ E; Guasopo B. Woodlark Island, Milne Bay Province, $\Phi_O = 9°\ 13'\ 39"$ S, $\Lambda_O = 152°\ 57'\ 03"$ E; Hetau Island Naval Astro, Buka Island, North Solomons Province, $\Phi_O = 5°\ 09'\ 57"$ S, $\Lambda_O = 154°\ 31'\ 12"$ E;

Hong Astro (1947), Manus Island, Manus Province, West Base, Φ_0 = 1° 58' 03.930" S, Λ_0 = 147° 22' 03.320" E, azimuth α_0 = 111° 55' 58.00" to Azimuth Mark from north, Clarke 1866 ellipsoid, elevation = 6.0 ft.; Jammer Bay, Milne Bay Province, Φ_0 = 9° 58' 28" S, Λ_0 = 152° 11' 15" E; Kavieng, New Ireland Province, Φ_0 = 2° 36' S, Λ_0 = 150° 50' E; Keila Island Astro, East New Britain Province, Φ_0 = 4° 48' 28" S, Λ_0 = 152° 11' 15" E; Kieta, North Solomons Province, Ashton, Φ_0 = 6° 12' 42.68" N, Λ_0 = 155° 37' 43.69" E; Koiaris, North Solomons Province, Koiaris Astro 1947, Φ_0 = 6° 18' 06.11" S, Λ_0 = 155° 11' 47.32" E, azimuth a_0 = 322° 19' 42.4" to Azimuth Mark #1 from south, International ellipsoid, established by 657th Engineering Astronomic Determination, March 1947; Losuia, Milne Bay Province, Losuia, Φ_0 = 8° 32' 33.825" S, Λ_0 = 151° 03' 59.466" E; Matupi, East New Britain Province, Matupi Astronomic Station 1957, Φ_0 = 4° 14' 12.210" S, Λ_0 = 152° 11' 26.54" E, International ellipsoid, Elevation = 2.4 meters; Popondetta, Astro fix, Φ_0 = 8° 46' 07.76" S, Λ_0 = 148° 12' 51.55" E; St. Matthais, New Ireland Province, South Base, Φ_0 = 1° 40' 30" S, Λ_0 = 149° 54' 54" E; Salankaua, Morobe Province, Φ_0 = 6° 33' 28.4" S, Λ_0 = 147° 51' 07.2" E; Torokina, North Solomons Province, Naval Astronomic Station, Φ_0 = 6° 12' 18" S, Λ_0 = 155° 02' 02.5" E; Wabutina, Milne Bay Province, Wabutin (spelling may be Wabutima), Φ_0 = 8° 30' 54.628" S, Λ_0 = 151° 03' 24.947" E; Wau, Morobe Province, Φ_0 = 7° 20' 28.12" S, Λ_0 = 146° 42' 55.6" E; Wewak. Φ_0 = 3° 32' 52" S, Λ_0 = 143° 37' 37" E.

The various local astro datums listed above represent the fixes used for navigational charts. In regard to how these various datums are related to the WGS 84 Datum, the Australian Maritime Safety Authority comments: "For some charts, particularly in Papua New Guinea, the correction to be applied to GPS cannot be calculated and these charts display a specific warning to this effect. Use of GPS alone on these charts is hazardous."

For the most part, cartographic products of Papua New Guinea have been on the Australian Geodetic Datum of 1966 with its origin at Johnston Cairn where: Φ_0 = 25° 56' 54.5515" S, Λ_0 = 133° 12' 30.0771" E, h_0 = 571.2 m., and the ellipsoid of reference is the Australian National Spheroid: a = 6,378,160 m, and $1/f$ = 298.25. A new system is the Papua New Guinea Geodetic Datum 1994 (PNG94), which is a geocentric datum defined by a widespread network of geodetic stations around PNG. There are three permanent GPS base stations operating in PNG. The Papua New Guinea Map Grid 1994 (PNGMG) is the UTM grid on the GRS80 ellipsoid. According to the Department of Surveying and Land Studies of the Papua New Guinea University of Technology, "A very approximate relationship between AGD66 and PNG94 coordinates is as follows: PNG94 Latitudes are approximately 5" north of AGD66 latitudes, PNG94 Longitudes are approximately 4" east of AGD66 longitudes, PNGMG Eastings are approximately 120 m greater than AMG66 Eastings, and PNGMG Northings are approximately 160 m greater than AMG66 Northings."

There is a caveat to this approximate relation between AGD66 and PNG94. Again, according to the Department of Surveying and Land Studies, "Tectonic motion is unaccounted for in the realization of the datum. Relative motion between different tectonic regions in PNG is often in excess of 8 cm per year. There are inconsistencies of up to 12 m between tabulated PNG94 coordinates and those derived from high precision GPS survey network adjustments…."

Thanks to John W. Hager for his patience with my requests and his generous help.

Update

"Existing PNG94 already 21+ years old now (i.e. Possibly past its coming of age) PNG2020? (ITRF2014 at epoch 2020.0) would remove any uncertainty arising from 26 years of earthquakes (coseismic and postseismic deformation). Coordinates closer to current ITRF, but up to 2 m different to PNG94. Requires gridded distortion model for PNG94 to PNG2020 transformations (e.g. legacy data such as DCDB, project datums, GIS data).. 50 Years (and +) of Geodesy in PNG, Richard Stanaway, 2016.

The Association of Surveyors of Papua New Guinea, Inc. has numerous technical papers and notes available for download in pdf format at: http://www.aspng.org/techinfo.htm

Geodetic and Vertical Datums Used in Papua New Guinea – An Overview
https://www.searchanddiscovery.com/pdfz/documents/2020/70410stanaway/ndx_stanaway.pdf.html

A Semi-Dynamic Geodetic Datum For Papua New Guinea
https://www.semanticscholar.org/paper/A-SEMI-DYNAMIC-GEODETIC-DATUM-FOR-PAPUA-NEW-GUINEA-Stanaway/49f1c8a765a39ddf672da0c89a4109a0b6df9f79

ASPRS SAC IS FALLING INTO A NEW SCHOOL YEAR!

As we move into the new school year, your Student Advisory Council would like to inform you of some exciting new happenings within the Council: fun events, new members, and more. Make sure you don't miss out on these exciting opportunities!

Exciting Events in November!

- **GIS Day Map Contest**

Every year the geospatial community celebrates all things GIS and Remote Sensing on GIS Day (November 16th). Your SAC celebrates this special time with a fun, student map contest!

Submit your best map to the SAC to be voted on! The five maps with the most votes will win fun prizes and bragging rights! Must be a student member of ASPRS to enter. Watch the weekly newsletter or email us at Sac@asprs.org for contest information.

Need inspiration? Check out the maps and winners from the 2021 contest: https://tinyurl.com/ASPRSSAC2021MAPCONTEST

- **SAC Elections and a New SAC Chair**

The SAC is currently looking for new Councilors to join our team! Positions include Deputy Chair, Educational & Professional Development Councilor, Deputy Educational & Professional Development Councilor, Communications Councilor, Deputy Communications Councilor, and SAC & ECPC Liaison.

All ASPRS student members are eligible to be nominated and to vote in the election on November 30. The SAC Elections will take place in a virtual meeting on November 30, 2022. Student members of ASPRS must be present at this virtual meeting to vote! SAC Councilor terms are one year, beginning and ending at the ASPRS Annual Meeting at Geo Week.

To submit a nomination, please fill out the form here https://tinyurl.com/ASPRSSACVOTE.

Nominations are due by 11:59 PM Eastern time on November 28, 2022.
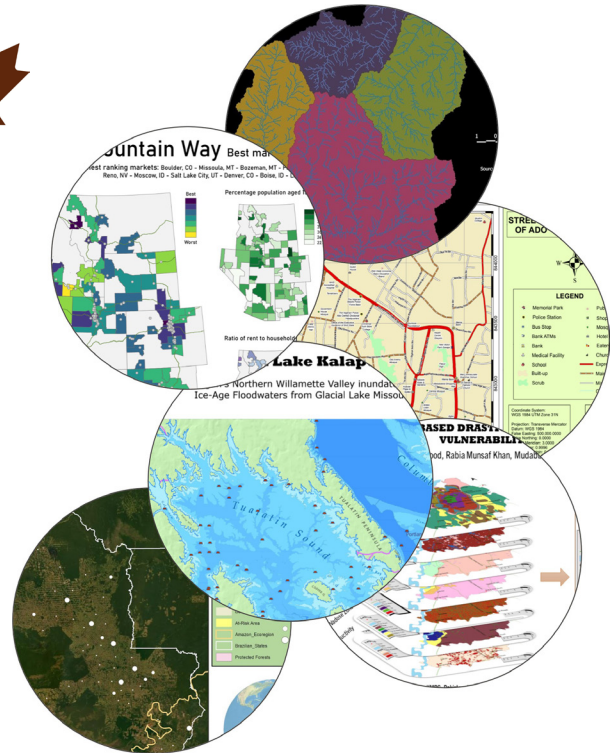
Also, the SAC welcomes the new Chair, Oscar Duran and sincerely thanks outgoing Chair Lauren McKinney-Wise for her service to the SAC and to the ASPRS student community!

- **Student Scholarships**

ASPRS scholarships are available for students and the application deadline is November 11, 2022! Scholarships will be awarded at the 2023 ASPRS Annual Meeting at Geo Week. The total award pool for the current year is over $40,000. Don't miss out on this amazing opportunity and APPLY. Check out this link for more details: https://www.asprs.org/education/asprs-awards-and-scholarships

---

If you are interested in participating in SAC activities:

Join us via Zoom every other Wednesday from 12–1 pm Pacific Time! To get the Zoom link, email us at sac@asprs.org.

ASPRS STUDENT ADVISORY COUNCIL

OSCAR DURAN COUNCIL CHAIR	**TBD** EDUCATION & PROFESSIONAL NETWORKING CHAIR	**RABIA MUNSAF KHAN** COMMUNICATIONS COUNCIL CHAIR
TBD DEPUTY COUNCIL CHAIR	**ALI ALRUZUQ** EDUCATION & PROFESSIONAL NETWORKING COUNCILOR	**KENNETH EKPETERE** CHAPTERS COMMITTEE CHAIR
CHUKWUMA JOHN OKOLIE COMMUNICATIONS COUNCIL MEMBER	**TESINI PRECIOUS DOMBO** COMMUNICATIONS COUNCIL MEMBER	**FREDA ELIKEM DORBU** COMMUNICATIONS COUNCIL MEMBER

ASPRS NEWS

ASPRS ANNUAL ELECTION ANNOUNCMENT

Amendments to the ASPRS Bylaws (www.asprs.org/governance/current_bylaws), adopted by the Board of Directors on July 19, 2022, resulted in changes to annual election procedures. Election balloting will now take place annually between November 1 – 30. Individuals who are elected will be installed at the next Annual Meeting of the Society, which for 2023 will take place in February at Geo Week.

In accordance with the Bylaws, all ballots shall be cast electronically. The upcoming election will be conducted using SurveyMonkey. All Individual Members of the Society in good standing as of November 1 are eligible to vote. Ballots will be sent to the primary email address in each Member's MyASPRS profile. Please take a moment to login and update your profile. If you have any questions or need assistance to login, please contact office@asprs.org.

The Bylaws provide for additional nominations to be presented by petition. The deadline for petitions was October 10, after this edition of *PE&RS* had already gone to the printer. Please review the electronic ballot carefully for possible additional candidates. Full candidate biographies and vision statements will be also included in the electronic ballot. For further description of the duties of the officers and details of the election process, please refer to the ASPRS Bylaws.

NEW ASPRS MEMBERS

ASPRS would like to welcome the following new members!

At Large
Hadi Karimi

Cascadia
Friedrich Knuth
Jack Rosenblit

Eastern Great Lakes
Aaron Michael Gonick
Jian Wang

Florida
Shane Williams

Gulf South
Mathew Abraham Chennikara
Jose Galvan, III
Karla M. Negron Loubriel
Shaun Piepkorn

Northeastern
Christine Bunyon

Pacific Southwest
Glenn Ingram

Potomac
Rachel Hixson
Larry Eldred Kirkpatrick
Steven Painter

Rocky Mountain
Adeoti Basheerah Akinbode-Olalere
Jonathan Stanford Keller
Dennis McCarville
Jared Robertson

Western Great Lakes
Quentin Ikuta
Jae Sung Kim

FOR MORE INFORMATION ON ASPRS MEMBERSHIP, VISIT
HTTP://WWW.ASPRS.ORG/JOIN-NOW

ASPRS ANNUAL ELECTION ANNOUNCMENT *continued*

The candidates for ASPRS Vice President for 2023 are:

Dr. Amr Abd-Elrahman
Associate Professor of Geomatics,
University of Florida

Dr. Caixia Wang
Associate Professor of Geomatics,
University of Alaska, Anchorage

The candidates for Assistant Director of the Primary Data Acquisition Division for 2023–2024 are:

Mike Baranowski
Senior Geospatial Analyst,
Dewberry

Ravi Soneja
Geospatial Services Technician,
Ayres Associates

The candidates for Assistant Director of the Professional Practice Division for 2023–2024 are:

Matthew Elious
Senior Project Manager,
KCI Technologies

Christian Stallings
Director of Operations,
Alynix

The candidates for Assistant Director of the Remote Sensing Applications Division for 2023–2024 are:

Dr. Indumathi Jeyachandran
Assistant Professor of Civil and
Environmental Engineering,
San Jose State University

Dr. Michael Starek
Assistant Professor of GISc
and Geospatial Survey Engineering,
Texas A&M University

Call for *PE&RS* Special Issue Submissions

Innovative Methods for Geospatial Data using Remote Sensing and GIS

Internationally comparable data is a global need for managing resources, monitoring current trends and taking actions for sustainable living. Even though there has been a significant progress on geospatial data availability, extensive data gaps are still a major problem for general assessment and supervise the progress through the years. According to United Nations 2022 The Sustainable Development Goals Report, while health and energy sectors have the highest data available, limited data available for climate action.

The COVID-19 crisis has also shown that there are innovative data collection methods utilizing information and computer technologies. However, only 5% of the countries have benefit from remote sensing technologies to measure the impact of COVID-19. Additionally, novel approaches such as artificial intelligence should be used in conjunction with assessments to make sure they are put to use for critical situations.

The recent developments in remote sensing, geographic information systems and ICT have provided a wide accessibility to create geospatial data for various purposes. The proposed special issue focuses on *"Innovative Methods for Geospatial Data using Remote Sensing and GIS" for wide range of applications. This special issue aims to bring researchers to share knowledge and their expertise about innovative methods to contribute to fill data gaps around the world for a better future.*

The proposed special issue aims to contributes ASPRS's key mission on 'Simplify and promote the use of image-based geospatial technologies for the end-user', 'Promote collaboration between end users and geospatial experts to match data and technology to applications and solutions' and 'promote the transfer of geospatial data and information technology to developing nations' by providing innovative methods to create geospatial data using remote sensing and geographic information systems utilizing state-of-the-art developments and solutions.

Deadline for Manuscript Submission—July 1, 2023

Submit your Manuscript to http://asprs-pers.edmgr.com

Guest Editors

Dr. Tolga Bakirman, bakirman@yildiz.edu.tr , *Yildiz Technical University, Department of Geomatic Engineering*, Davutpasa Campus, 34220 Esenler-Istanbul/Turkey

Dr. George Arampatzis, garampatzis@pem.tuc.gr, *Technical University Crete, School of Production Engineering & Management*, 73100 Chania – Crete/Greece

Development of Technique for Vehicle Specific Off-Road Trafficability Assessment Using Soil Cone Index, Water Index, and Geospatial Data

Sunil Kumar Pundir and Rahul Dev Garg

Abstract

Nowadays, the type of vehicles, either tracked or wheeled in the Army has increased considerably and every decision maker wants the current details of off-road trafficability for operation planning. Therefore, vehicle-specific trafficability maps are the need of the hour. Emphasis should be given on soils capable of bearing the moving load of a vehicle and it is an important factor to be considered. Soil variability in spatial and temporal dimensions affects the assessment of off-road trafficability. Genetically, it is assumed that similar soil types behave similarly at a regional scale to reduce the complexity due to its variability. Remolding Cone Index (RCI) of Soil is the indicator of its capability and for generic solution; its value can be related to gravimetric moisture of soil for getting a general idea. In this paper, a logics-based, new concept has been introduced to rationalize the RCI values of these moist areas. Most significantly, moisture- and water-bound areas play an important role in the assessment of off-road trafficability. Therefore, to cover larger areas, a grid-based approach was taken as a base and, to get a preliminary idea of prevailing moisture, Normalized Difference Water Index was also mapped. Every vehicle has fixed vehicle cone index based on its vehicular characteristics and can be related with RCI for trafficability purpose. This new technique will save time and field work and is immensely useful for the trafficability assessment of any specific vehicle.

Introduction

Off-road trafficability mapping is a very important tool for strategic planning for battlefield operations; therefore, advanced techniques and tools should be developed for its assessment. A technique was developed by using not only soil properties but also other geo-parameters like landform, land use, slope, and moisture. New ways were found out in the form of logics using domain knowledge and complemented by extensive use of advance remote sensing tools. Therefore, trafficability analysis of any particular vehicle was done for a larger area within a limited time and it was the main objective of the present study. Numerous geographic factors are responsible for off-road trafficability (Rybansky 2014). Whereas, to avoid complexity and biasness, a rule-based approach was also used for trafficability assessment by considering only four factors like slope in six ranges (0–7; 8–14; 15–21; 22–28; 29–35, >35°), land use, soil moisture, and soil type (Pundir and Garg 2020b). However, out of four, variability of slope, land use, and soil type are less in spatial and temporal domain and can be extracted precisely with established methods, while soil moisture is highly variable in both domains (Owe *et al.* 1989). It is directly related with weather, water bodies, and its peripheral topography of study area. Soil texture is inversely affected by moisture in the current scenario as the larger

the grain size, the lesser is the effect of moisture for off-road trafficability. Trafficability can be assessed with soil remolding cone index (RCI) based on soil characteristics and vehicle cone index (VCI) based on vehicular characteristics (Hubacek *et al.* 2014). A vehicle based experimental study of terrain accessibility was also carried out to assess the obstacles in maneuvering (Jagirdar and Trikande 2019). In an earlier attempt, map overlay was used to prepare desert terrain analog for quantification of desert areas using remote sensing data and methods (Van Lopik and Kolb 1959). Remote sensing-based thematic integration for terrain characterization was also tried for different purposes. In this direction, a way ahead, qualitative trafficability data was converted into various quantitative zones based on assessment of obstacles produced by contributing factors (Pundir and Garg 2020a).

Recent advancement of geographic information systems (GIS) and image processing tools have facilitated the extraction of direct or indirect information in the form of thematic maps or measurement from digital topographic and satellite data. Extracted information depends on the skill and experience of the interpreter to convert the information as per the requirements (Collins 1975). To make the information more specific as per requirement, information from various sources can be integrated with remote sensing techniques (Anderson 1977).

Nowadays, plenty of satellite data in a wide range of spectrum are available and several GIS (Baijal *et al.* 2002; Taloor *et al.* 2020) and image processing software are also available to process the data in desired shape. Initially, efforts were made to improvise the method in terms of speed, precision, and ease (Wright and Burns 1968). A study on unmanned ground vehicles was also done to predict the suitability of terrain for off-road movement (Pokonieczny and Rybanský 2018).

Pioneer work on prediction of seasonal forecasts of mobility using water budget models was also a landmark in this direction (Kennedy *et al.* 1988). A model was also developed between soil strength and soil moisture using generalized relationships (Sullivan *et al.* 1997). Further, estimation of RCI for different soils and its linkage with California Bearing Ratio was established for trafficability (Mason and Baylot 2016).

The Normalized Difference Water Index (NDWI) measures liquid water molecules in vegetation canopies produced with interaction of solar radiation. It is sensitive to changes in the water content and spongy mesophyll in vegetation canopies (Gao 1996). This is conceptualized for the estimation of soil moisture and canopy water content (Jackson *et al.* 2004). Water presence in the area depends upon local climate and soil properties, which in turn can be related with NDWI. This index uses short-wave infrared (SWIR)-1 bands M10, which is sensitive to changes in liquid water. The spectra region having green vegetation is affected by water absorption and can capture information on temporal change of water (Sanchez-Ruiz *et al.* 2014). An empirical relation was also developed to assess the spatial variability of off-road trafficability based on experiments on analogous sites (Pundir and Garg 2021). Meanwhile, an approach was also presented by developing of

Sunil Kumar Pundir is with the Defence Geoinformatics Research Establishment, Defence Research and Development Organization (DRDO), Chandigarh, India (sunilremotesensing@gmail.com).

Rahul Dev Garg is with the Department of Civil Engineering, Indian Institute of Technology, Roorkee, Uttarakhand, India.
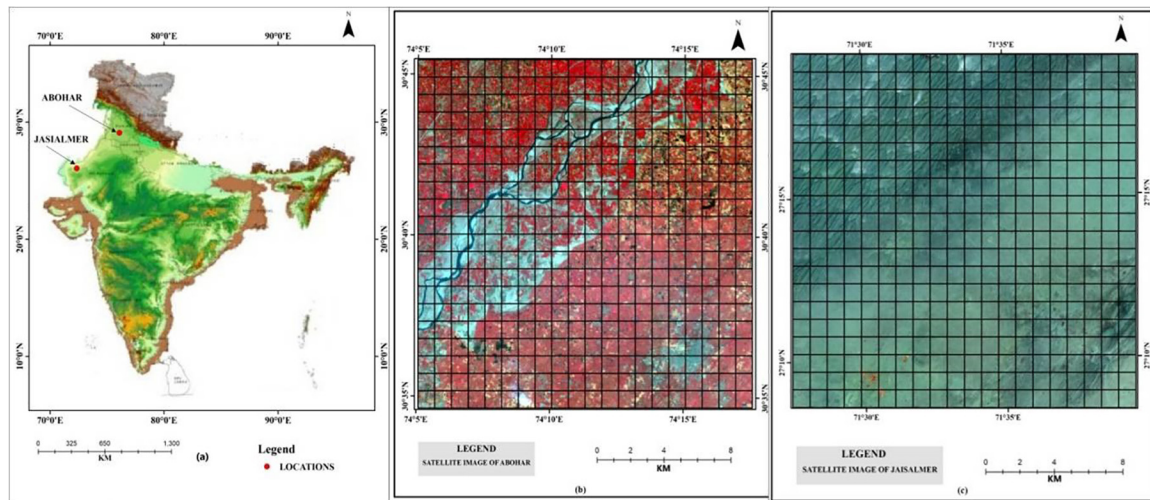
Figure 1. (a) Location map of India showing the location of study areas; (b) satellite data-based map of Abohar; (c) satellite data-based map of Jaisalmer.

modified equation for estimation of RCI using geospatial technology (Pundir and Garg 2022).

Study Area

Two study areas are selected for off-road trafficability assessment, and their geographical extent is given in Table 1. Location map and satellite data are shown in Figure 1a–c. These two areas were selected based on utility of study as planning for off-road trafficability. From an off-road trafficability point of view, the desert and plain areas are more suitable for operation; therefore, the two selected areas fulfill this criterion. The study areas have been named by a major city present in the vicinity of an area chosen. Thus, the first area is Abohar and second area is Jaisalmer.

Data and Methodology

The main scope of this study is to develop the technique for the generation of a vehicle-specific trafficability map with extensive use of remote sensing data and its high-tech tools. The five main parameters responsible for trafficability like landform, land use, slope; soil, and moisture are used for its assessment. *Landsat-8* (Operational Land Imager (OLI) sensor) satellite data with an accuracy of 30 m, georeferenced topographic maps, Shutter Radar Topography Mission Digital Elevation Model (SRTM-DEM) of 30 m accuracy, available soil texture information, ancillary and field data are used as input data. The details of input data are shown in Table 2. The flow chart of methodology is depicted in Figure 2.

Four multispectral bands (blue, green, red, and near-infrared (NIR)) of *Landsat-8* (OLI sensor) were used for preparing various maps like land use/land cover and NDWI map at scale of 1:50 000. The qualitative assessment of moisture on regional basis was also inferred by calculating the NDWI from satellite data and further in situ observations or generalized values (Sullivan *et al.* 1997) were used to fill the gap, if any.

Thematic Maps and Products

The thematic information was extracted with the help of input data to prepare intermediate thematic maps, which helped to achieve the outcomes, i.e., vehicle specific trafficability maps.

Land Use/Land Cover Map

Land use/land cover is directly captured from the space borne sensor; therefore, its demarcation to various, similar categories can be done with available interpretation tools and techniques (Anderson 1977). Land use information of different categories was extracted using a post-classification scheme, where the numbers of categories were chosen after preliminary survey for better accuracy. Further, supervised

Table 1 Extent of study areas.

S. No	Study area	Elevation range (m)	Area (Km²)	Extent of area	
				Latitude	Longitude
1	Abohar	93 to 464	374.30	30°34.52′ to 30°45.30′N	74°5′ to 74°17.5′E
2	Jaisalmer	105 to 202	375.00	27°8.6′ to 27°19.4′N	71°27.5′ to 71°40′E

Table 2 Input data source and type.

S.No	Agency	Data
1	USGS website	LANDSAT 8 data
2	Bhuvan website(ISRO-NRSC)	Soil texture information
3	National Bureau of Soil Survey and Land Use Planning, Nagpur (NBSS & LUP)	Soil texture & land use information
4	IIT, Roorkee	Sieve analysis for determination of soil texture of field samples
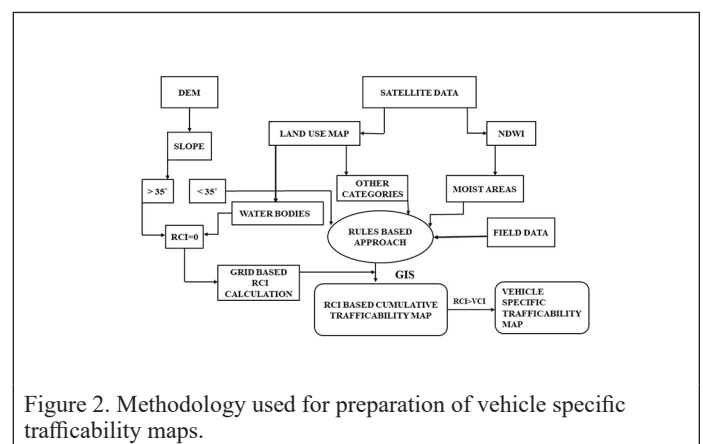
Figure 2. Methodology used for preparation of vehicle specific trafficability maps.

classification was performed using ERDAS IMAGINE software and Maximum Likelihood Classifier algorithm. Accuracy assessment was done with the help of an error matrix and overall accuracy was evaluated. For every class, a minimum of six training samples were created and ground validation was done physically with the help of a Global Positioning System. The overall accuracy for Abohar and Jaisalmer was found to be 91.59% and 93.16%, respectively. The error matrix for the Abohar area is shown in Table 3.

Slope

Every vehicle has its own capability to negotiate the slope of terrain. The highest negotiable value of a slope for that vehicle is the threshold; beyond this value, no movement is possible (Collins 1975). A tracked vehicle has a maximum capability to negotiate the slope, and threshold value is 35°, and for a wheeled vehicle, the threshold value is 31°. The slope map was obtained by processing the SRTM data using ERDAS IMAGINE software. In the absence of continuous data, a low pass filter was used to fill the gaps.

Soil Texture

Soil consists of mainly three constituents like clay, silt, and sand, but various classification systems exist and are defined in different forms. Satellite data, in combination with land use and field data, can provide the useful information about soil (Wong *et al.* 1977). Preliminary survey findings of the study area indicate the relation between land use and soil type, but often, it is observed that the same soil is covered with different land use categories and vice versa. The soil types prevailing in the area per textural classification of the United States Department of Agriculture (USDA) is by having different compositions of clay, silt, and sand and are listed in Table 4. The above soil types are converted from USDA classification to Unified Soil Classification System (USCS) (Ayers *et al.* 2011; Frankenstein 2014) as tabulated in Table 5.

Soil Moisture

The soil strength is highly sensitive towards moisture and varies accordingly. Qualitative assessment can be made by analyzing the optical satellite data (Singh *et al.* 2017), while for quantitative assessment, microwave satellite data or instrument-based measurement should be taken in the field (Flores *et al.* 2014; Stevens *et al.* 2017). The moisture is taken in qualitative terms as dry, moist, and saturated for the rule-based approach (Pundir and Garg 2020a), while for RCI calculation, either the generalized values given by researchers were used or in the next level, field observations were rationalized with NDWI map findings. This approach worked well because the study is required to produce output for regional-level planning and not for strategic planning. The moist terrain patches are demarcated from the NDWI map or by comparing the appearance of the lighter tone of soil to the darker tone of saturated soil.

Normalized Difference Water Index (NDWI): The NDWI uses GREEN and NIR or NIR and SWIR bands to display moisture. In the present study, the main requirement is to delineate the water bodies and moist areas, which will ultimately help in rejecting the outlier values of RCI calculated based on soil parameters. In the past, (McFeeters 1996) GREEN and NIR wavelengths were used to monitor changes related to water content in water bodies and moisture present on the surface in place of NIR and SWIR.

Preparation of Combined Trafficability Maps

To assess the complex terrain behavior and variability of cone index and soil moisture in spatial domain, the area was divided into cells. Each area consists of 400 cells and there indexing is done from upper left (1, 1) to lower right (20, 20). The various parameters responsible for off-road trafficability were evaluated by assuming similar behavior in a cell. All the observations and interpretations were executed on the basis of a cell. Due to the large extent of the study area and to avoid a

Table 3. Error matrix for accuracy assessment of land use of Abohar area.

Actual class	Predicted Class					
	Sandy area	Built up	Fallow land	Agriculture land	Water bodies	Total
Sandy area	363	28	26	16	0	433
Built up	24	226	0	0	0	250
Fallow land	0	0	972	48	0	1020
Agriculture land	0	0	188	1776	0	1964
Water bodies	0	0	0	0	259	259
Total	387	254	1186	1840	259	3926

Table 4. Soil textures prevailing in study areas.

S. No.	Study area	Major soil textures
1	Abohar	Sand, sandy loam, loam, sandy clay loam, clay loam
2	Jaisalmer	Sand, loamy sand, sandy loam, loam and sandy clay loam

Table 5 USDA classification equivalency in USCS classification.

USDA classification	USCS classification	
	Most Probable	Possible
Sand	SW, SP	-
Loamy sand	SM	SC
Sandy loam	SM	-
Loam	ML	-
Sandy clay loam	SC	-
Clay loam	CL, MH	-

detailed manual survey, the method of calculating RCI at the first level was by observing the soil type as per USCS classification, and gravimetric moisture (Mason and Baylot 2016) was used to fill the gaps. Secondly, a new concept of logics-based analysis was used for categorization of terrain into different trafficability zones. This approach will accelerate the process for preparing the trafficability maps. Except for extreme ends of USCS soil classification (gravels and peat), the following equation (Knight 1961) represents the results satisfactorily:

$$\text{RCI} = \exp[a' - b' \, ln(\text{MC})],$$

where a' and b' are coefficients specified for respective soils as given in Table 6 (Sullivan 1997; Clapp and Hornberger 1978; Sellers 1986) and MC (%) is the soil moisture content by weight, MC = MV($\rho w / \rho s$) × 100%, whereas ρw and ρs are water density and soil density, while MV is volumetric soil moisture and defined as the ratio of water volume to soil volume.

Based on the above criteria, RCI values were obtained for each cell of both study areas; however, to show the procedure, 10 cell values of each area are shown in Tables 7 and 8.

Water bodies produce the highest level of obstacle to both type of vehicles, either tracked or wheeled; therefore, null value of RCI was

Table 6. Values of soil parameters & Coefficients.

USDA soil classification	USCS soil classification	RCI coefficients a'	RCI coefficients b'	Average value of Dry density (lb/ft³)	Gravimetric moisture (%)
Sand	SP	3.987	0.815	93.6	34.70
Loamy sand	SM	12.542	-2.955	93.7	40.80
Sandy loam	SM	12.542	-2.955	93.7	40.80
Loam	ML	11.936	-2.407	73.7	53.70
Sandy clay loam	SC	12.542	-2.955	97.4	41.90
Clay loam	CL	15.506	-3.530	86.8	46.90

Table 7. RCI calculation based on soil parameters & NDWI values for Abohar area.

Grid reference	NDWI value	USCS soil classification	NDWI >0.3 Yes/No	Water body Yes/ No	Dry Density (lb/ft³)	Volumetric moisture (%)	RCI	RCI assigned in case of water body
(1,14)	0.80	Sand	Yes	Yes	93.6	2.32	75.61	0.0
(2,2)	0.18	Loam	No	No	73.7	27.53	77.94	77.94
(2,13)	0.55	Sand	Yes	Yes	93.6	3.03	93.99	0.0
(2,14)	0.56	Sand	Yes	Yes	93.6	2.96	92.22	0.0
(3,3)	0.26	Sand clay loam	No	No	97.4	26.69	62.08	62.08
(3,12)	0.55	Sand	Yes	Yes	93.6	3.68	110.13	0.0
(3,13)	0.64	Sand	Yes	Yes	93.6	3.62	108.66	0.0
(10,14)	0.14	Sandy clay loam	No	No	97.4	26.48	65.04	65.04
(15,15)	0.17	Clay loam	No	No	86.8	32.87	76.79	76.79
(18,4)	0.19	Clay loam	No	No	86.8	33.10	74.93	74.93

Table 8. RCI calculation based on soil parameters & NDWI values for Jaisalmer area.

Grid reference	NDWI value	USCS soil classification	NDWI >0.3 Yes/No	Water body Yes/ No	Dry Density (lb/ft³)	Volumetric moisture (%)	RCI	RCI assigned in case of water body
(2,2)	0.11	Sand	No	No	93.6	02.68	85.05	85.05
(4,2)	0.08	Sand	No	No	93.6	02.91	90.95	90.95
(5,19)	0.07	Sand	No	No	93.6	02.04	68.09	68.09
(7,4)	0.10	Sand	No	No	93.6	02.94	91.71	91.71
(7,12)	0.09	Sand	No	No	93.6	03.55	106.12	106.12
(13,15)	0.05	Sandy loam	No	No	93.7	24.62	71.94	71.94
(13,17)	0.09	Sandy loam	No	No	93.7	20.42	125.03	125.03
(16,16)	0.11	Sand	No	No	93.6	02.96	92.22	92.22
(18,3)	0.08	Sand	No	No	93.6	02.86	89.67	89.67
(18,18)	0.07	Sand	No	No	93.6	02.84	89.16	89.16

Table 9. Data base format for Decisions Analysis.

Geomorphology	Land use/ Land cover	Slope Classes (degrees)	Soil Moisture (Volumetric)	Soil Texture (ST)	Soil Strength
Alluvial Plains	Agriculture	0-7	Dry		RCI < 40
Sand sheet	Forest	8-14	(0 to 10%)	Sand	
Sand dune	Fallow land	15-21		Sandy loam	
Inter-dunal space	Forest	22-28	Moist	Silt	40 <RCI <60
Rocky exposure	Scrub	29-35	(10 to 30%)	Silty loam	
Flood plain	Water bodies	>3		Sandy Clay	RCI >60
Wet gap	Grass/grazing		Wet	Clay	
Bad land	Barren land		(>30%)	Clay loam	60<RCI<80
				Loamy sand	
				Loam	RCI>80

Table 10. Logics based analysis.

Decision Rules	Type of vehicle	Trafficability Category
1. Alluvial plain +Agriculture) +0°-7° Slope +SM 0-10% +ST Clay Loam +RCI>45	VCI 40	Go without obstacle
2. Alluvial plain+ Fallow land+8°-14° Slope +SM 10-30%+ST Clay+RCI1 <40	VCI 40	No GO
3. Sand dune+Scrub+8°-14°Slope+SM 0-10%+ST Sandy loam+ RCI1>60	VCI60	GO, Area is Trafficable
4. Wet gap or Bad land or Water bodies or Slope > 300 or SM>30% or RCI1< 40	VCI60 & VCI40	No movement is possible

ST – Soil Texture; SM – Soil Moisture; RCI1- Remolding Cone Index after one pass of vehicle.

assigned to cells having water bodies. A new concept was framed by considering geo-morphology, land use, slope, soil texture, soil moisture, and RCI value based on the tacit knowledge and field experience (Table 9). A logic frame was also designed to analyze the impact of other contributing factors on off-road trafficability (Table 10) because the factors are inter-related with each other; for example, the type of land use depends on soil texture, slope, and the presence of moisture.

Preparation of Specific Vehicle Trafficability Maps
Cumulative trafficability maps were processed using spatial analysis tool of ArcGIS software to determine the separate trafficability maps. Basically, taking advantage of the cell-based, cumulative RCI map for tracked and wheeled vehicles, two examples of vehicles having VCI40 and VCI60 are selected to facilitate the movement of the most usable vehicles during operations: light- and medium-weight tanks per the Table 11 (Army Field manual 5-430-00-1, Ch. 7, Soils Trafficability, 1994).

Results and Discussions
Based on the above methodology, the results are presented in this section. The maps (Figure 3a and 3b) showed the land use present in the area, and the details of different land use categories, along with geographical coverage are shown in Table 12. The slope maps of both study areas for available present ranges are shown in Figure 4a and 4b. NDWI maps were prepared using greyscale images to have more information and uniform presentation (Figure 5a and 5b). Visual or digital interpretation of the output image/raster created is similar to NDWI; negative values show no water content or vegetation, whereas a positive value shows the presence of water. The NDWI > 0.3 represents the water body, and hence it is very beneficial to delineate the water bodies in the study area.

Table 11. Vehicle types and VCI ranges.

Category	Range of VCI for 50 passes	Vehicles
1	<=29	Light weight vehicle with low contact pressure (less than 2 psi)
2	30 to 49	Engineer and high speed tractors with comparatively wide tracks and low contact pressures and Very light weight tank
3	50-59	Tractor with average contact pressure, tanks with comparatively low contact pressures and some trailed vehicles with very low contact pressures
4	60-69	Most medium tanks, tractors with very high contact pressures and all-wheel drive trucks , a great number of trailed vehicles and heavy tanks
5	70-79	Most all wheel trucks, a great number of trailed vehicles and heavy tanks
6	80-99	A great number of all-wheel drive and rear wheel drive trucks and trailed vehicles intended primarily for highway use
7	>=100	Rear wheel drive vehicles and others that generally are not expected to operate off roads, especially in wet soils

Table 12. Land use/ Land cover present in study areas.

Land use/Land cover	Abohar (km²)	%	Jaisalmer (km²)	%
Agriculture land	222.63	59.48	26.77	7.14
Fallow/ barren land	87.29	23.32	-	-
Built-up area	19.46	5.20	5.29	1.41
Sandy area	33.13	8.85	339.79	90.61
Salt affected area	-	-	3.08	0.82
Water body	11.79	3.15	0.07	0.02
Total	374.30	100	375.00	100

Based on the logics and computed RCI values, cumulative trafficability maps consisting of four RCI ranges (<40; 40–60; 60–80; >80) were prepared using ArcGIS software (Figure 6).

VCI60 and VCI40 show the vehicle cone index requirement for vehicles that are 60 and 40, respectively. After that, vehicle-specific trafficability maps were prepared by putting the minimum value of RCI required, which should be greater than 60 and 40 for VCI60 and VCI40 vehicles, respectively. By this process, GIS-based trafficability maps were prepared for VCI60 (Figure 7a–d) and similarly for VCI 40 (Figure 8a–d).

In cumulative RCI trafficability maps, the advantage of using a new, logics-based concept is clearly evident. The movement is only possible when the value of RCI is greater than VCI. The flow channel of a perennial water body appeared to be a no trafficability zone for both types of vehicles. Remaining areas pose no threat to maneuvering of tracked vehicles. In addition to this, the moist patches and depression zones in the vicinity of a river channel posed obstruction to the movement of wheeled vehicles. The Jaisalmer area is sandy and provides a good base for tracked vehicle for maneuvering, while the dunes present in the north-west corner of the study area make the movement impossible for wheeled vehicles. Based on these facts, the trafficability potential can be judged based on topography, surface material characteristics, and presence of moisture.

In vehicle specific trafficability maps, for VCI 40 vehicles, the GO area is higher in comparison to the GO area in VCI 60 vehicle trafficability maps. The simple reason is that the requirement of soil capability for movement is lower in the case of the VCI 40 vehicle.

In case of cumulative maps, statistics also shows that the area is good for tracked vehicles in comparison to wheeled vehicles. Results also show that more than 70% of study area is good for both types of vehicles for off-road trafficability (Figure 9a and 9b).

For the VCI40 vehicle, the percentage coverage of the NO GO area varies between 7.5 to 23% for the Abohar and 0.5 to 17.75% for the Jaisalmer area. For the VCI60 vehicle, the percentage coverage of the NO GO area varies between 14.75 to 37% for the Abohar area and 9.5 to 25.25% for the Jaisalmer area (Figure10a and 10b). It also shows the sandy area poses less threat to maneuvering in comparison to other types of areas.

The minimum value of the NO GO area is for tracked vehicles, while maximum value is for wheeled vehicles. It clearly indicates that
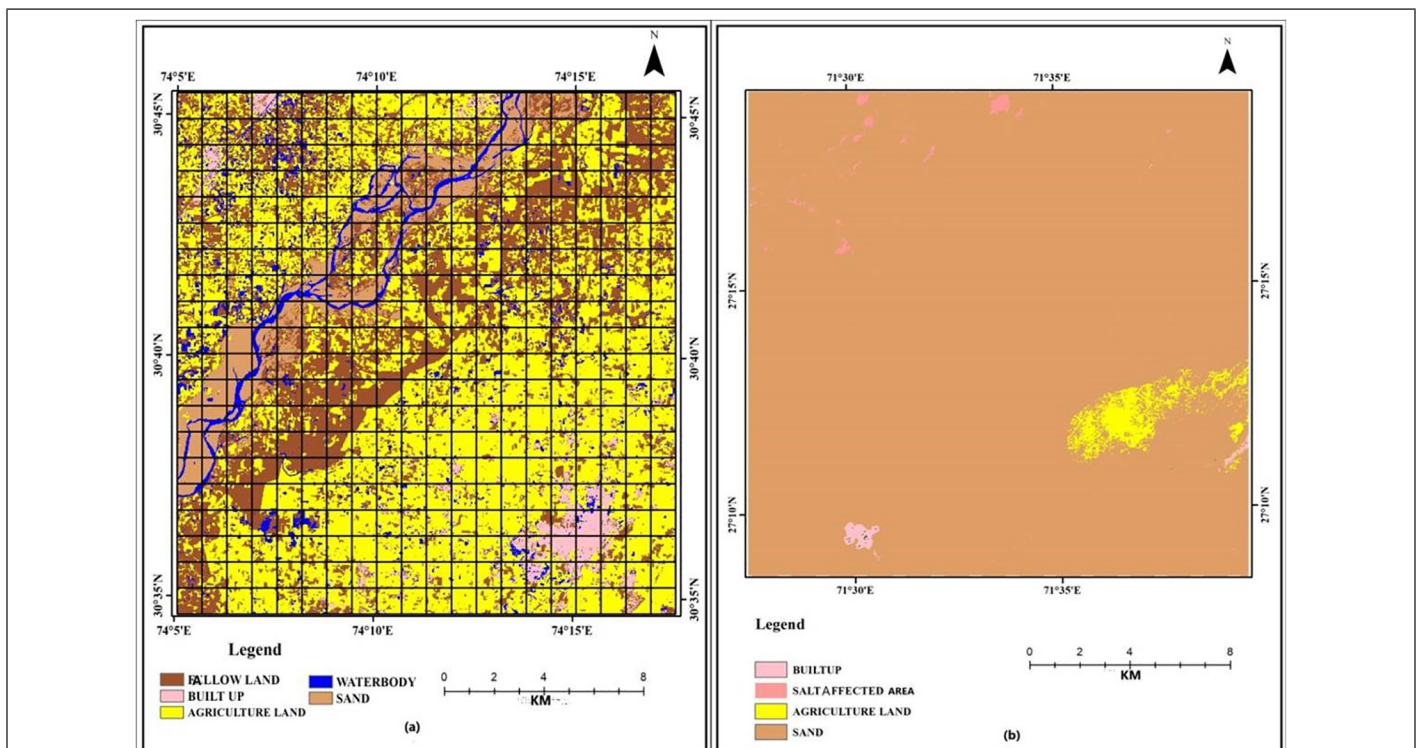
Figure 3. Land use map of (a) Abohar; (b) Jaisalmer.

tracked vehicles are preferable over wheeled vehicles for off-road trafficability operations. Secondly, with the help of data, it can be found that the value of the NO GO area increases with the increase of VCI.

Conclusions

A comprehensive solution for off-road trafficability was complex in nature due to the variability of the contributing factors. Only a top to bottom approach can handle this type of complexity. The first level evaluation takes place at landform level, and at the next level, land use, soil type, slope, soil moisture, and soil strength are considered. Based on land use, the water bodies were delineated and RCI values were assigned accordingly. The biggest challenge was to assess the variability of soil in spatial and temporal domains using remote sensing and ancillary data of such a huge area. New concepts of logics-based analysis made it simple by formulating the problem in various criteria
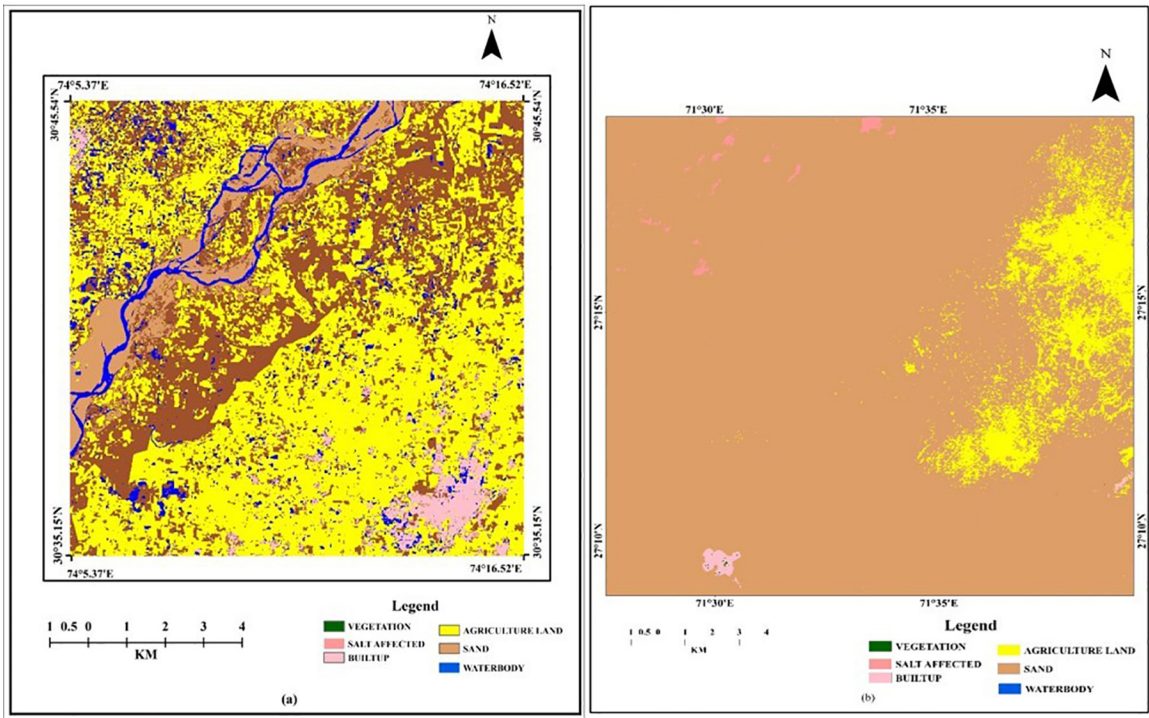
Figure 4. Slope map of (a) Abohar; (b) Jaisalmer.
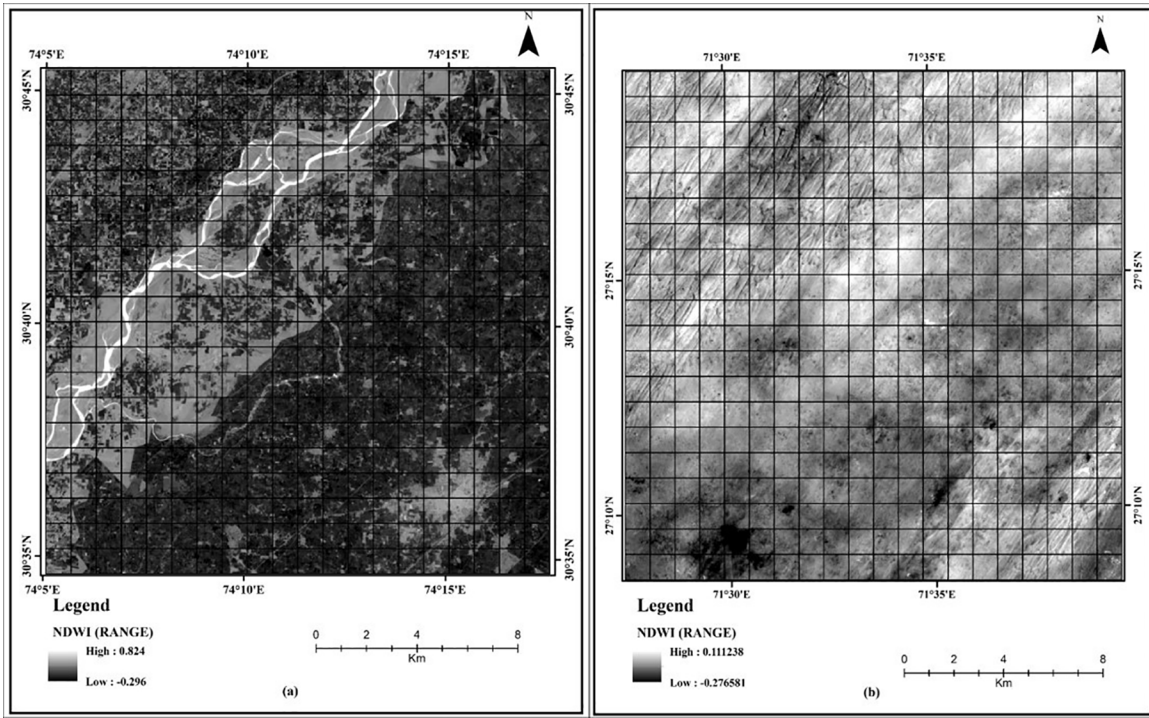
Figure 5. Normalized Difference Water Index (NDWI) greyscale map of (a) Abohar; (b) Jaisalmer.

and combinations for assessing the trafficability to the grid level. This approach provided very good results in this complex scenario.

As RCI is directly linked with VCI; therefore, categorization of cumulative RCI maps produced fruitful results. The vehicle-specific maps also matched with the terrain configuration as discussed above. Therefore, now a commander has the tool to decide the operation planning by observing the scope up to the level of a specific vehicle, either tracked or wheeled. Lots of efforts were made to have a comprehensive approach based on domain expertise and field experience, although it was a very difficult task to deal with factors and their variability. The conclusions that can be drawn from this study are:

• Preparation of vehicle specific trafficability maps
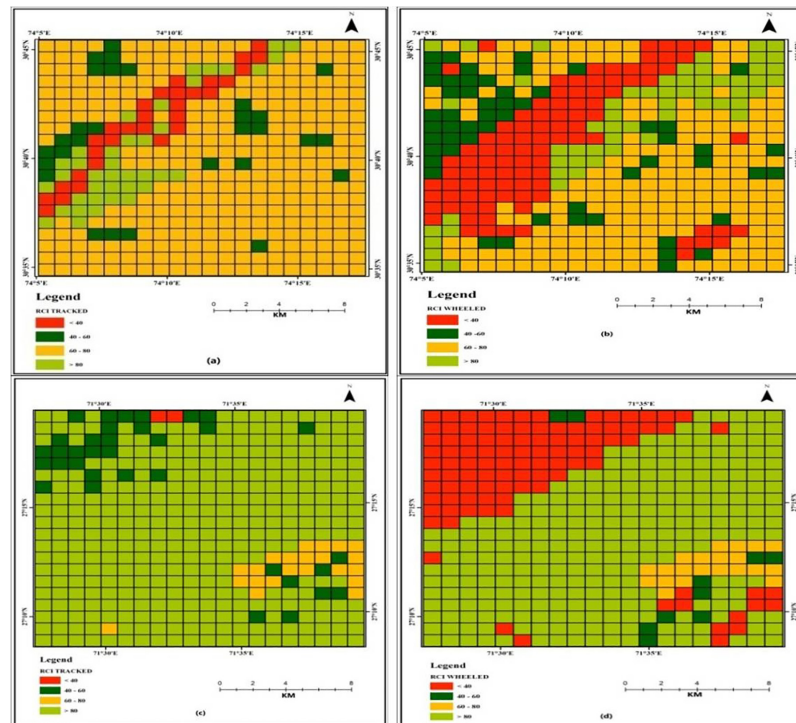
Figure 6. Cumulative remolding cone index (RCI) map of (a) Abohar-Tracked vehicle; (b) Abohar-Wheeled vehicle; (c) Jaisalmer-Tracked vehicle; (d) Jaisalmer-Wheeled vehicle.
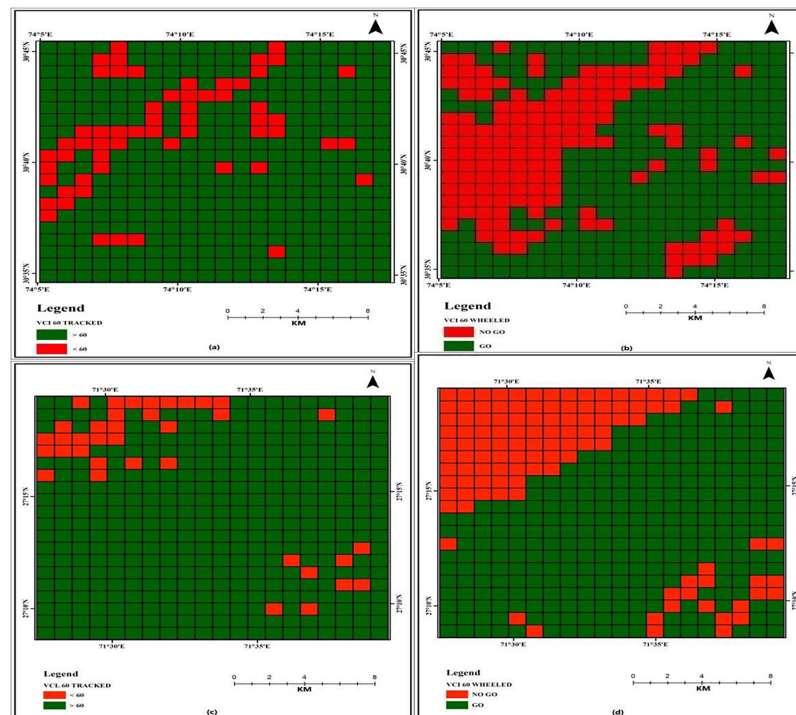
Figure 7. VCI60 vehicle specific trafficability maps of (a) Abohar-Tracked vehicle; (b) Abohar-Wheeled vehicle; (c) Jaisalmer-Tracked vehicle; (d) Jaisalmer-Wheeled vehicle.
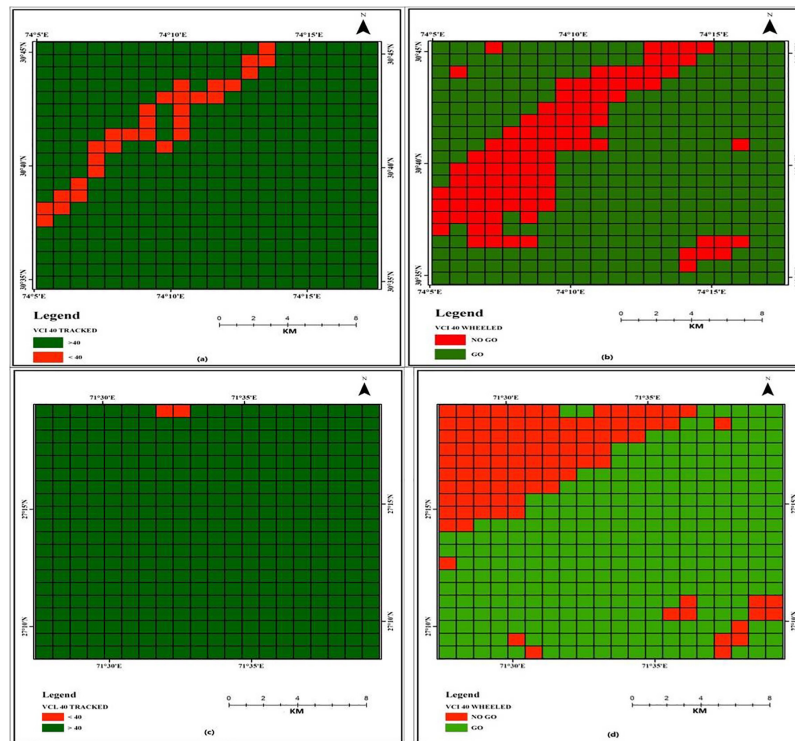
Figure 8. VCI40 vehicle specific trafficability maps of (a) Abohar-Tracked vehicle; (b) Abohar-Wheeled vehicle; (c) Jaisalmer-Tracked vehicle; (d) Jaisalmer-Wheeled vehicle.
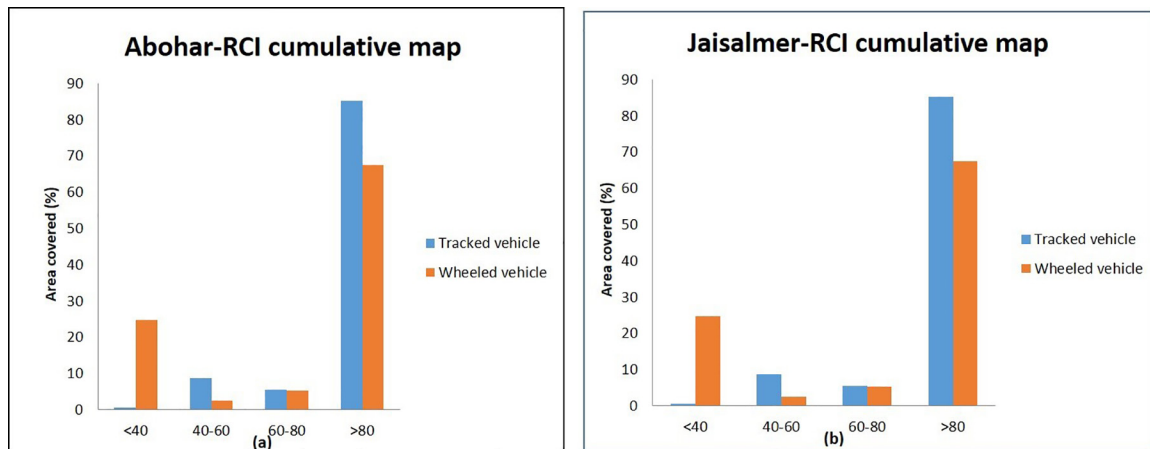
Figure 9. Trafficability area analysis for both types of vehicles of (a) Abohar; (b) Jaisalmer.

	Tracked vehicle Abohar	Wheeled vehicle Abohar	Tracked vehicle Jaisalmer	Wheeled vehicle Jaisalmer
NO GO	14.75	37	9.5	25.25
GO	85.25	63	90.5	74.75

	Tracked vehicle Abohar	Wheeled vehicle Abohar	Tracked vehicle Jaisalmer	Wheeled vehicle Jaisalmer
NO GO	7.5	23	0.5	17.75
GO	92.5	77	99.5	82.25
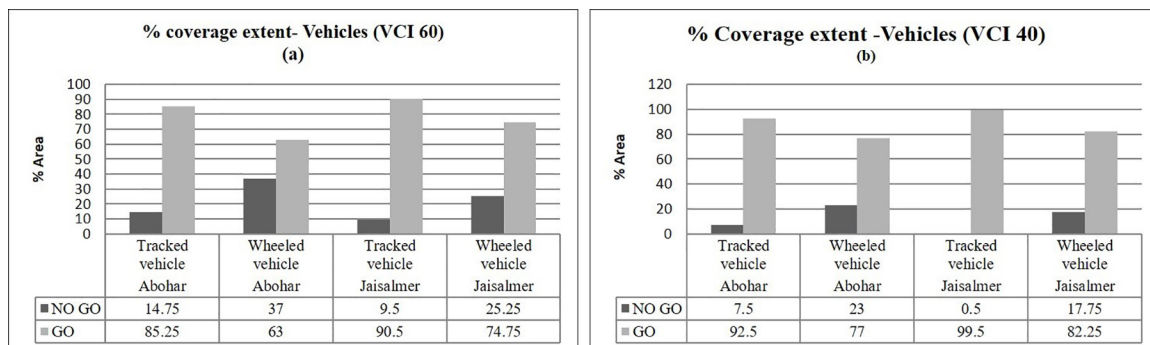
Figure 10. Vehicle specific trafficability GO or NOGO comparison in both areas: (a) Abohar; (b) Jaisalmer.

- The requirement of detailed investigations along with exhaustive field surveys can be minimized by using this study
- It will also pave the way for development of software and can provide a generic solution due to the wide horizon of consideration of maximum factors

The trafficability maps prepared for plain and desert areas also show the variation for particular vehicles, and it can be inferred that desert areas are good for off-road trafficability purposes besides non-negotiable dunes. The study will be useful for the operational purposes of Defence forces.

Acknowledgements

References

Anderson, J. R. 1977. Land use and land cover maps and statistics from remotely sensed data. *Remote Sensing of the Electromagnetic Spectrum* 4(4):193.

Ayers, P., G. Bozdech, J. Freeman, A. Reid and J. O'Kins. 2011. Development of a dynamic visco-elastic vehicle–soil interaction model for rut depth, energy and power determinations. Presentation to the U.S. Army Research, Development and Engineering Command, Army Tank Automotive Research, Development, and Engineering Center (RDECOM-TARDEC), DTIC ADA548853, held in Warren, MI, 9 June 2011.

Baijal, M. R., M. K. Arora and S. K. Ghosh. 2002. A GIS assisted knowledge-based approach for military operations. *GIS Development* 6:21–24.

Clapp, R. B. and G. M. Hornberger. 1978. Empirical equations for some soil hydraulic properties. *Water Resource Research* 14:601–604.

Collins, S. H. 1975. Terrain parameters directly from a digital terrain model. *The Canadian Surveyor* 29(5):507–518. http://doi.org/10.1139/tcs-1975-0052.

Flores, A. N., D. Entekhabi and R. L. Bras. 2014. Application of a hill-slope scale soil moisture data assimilation system to military trafficability assessment. *Journal of Terramechanics*:53–66. http://doi.org/10.1016/j.jterra.2013.11.004.

Frankenstein, S. 2014. *Fast All Season Soil Strength (FASST) Model Fact Sheet*. Hanover, N.H.: US Army Corps of Engineers, Engineer Research and Development Center. <http://www.erdc.usace.army.mil/Media/FactSheets/FactSheetArticleView/tabid/9254/Article/476752/fasst-model.aspx> Accessed 20 October 2017.

Gao, B. C. 1996. NDWI—A normalized difference water index for remote sensing of vegetation liquid water from space. *Remote Sensing of Environment* 58:257–266.

Hubacek, M., M. Rybansky, M. Brenova and L. Ceplova. 2014. The soil trafficability measurement in Czech Republic for military and civil use. In *Proceedings of the 18th International conference of the ISTV S2014*, held in Seoul, South Korea, September 2014.

Jackson, T. J., D. Chen, M. Cosh, F. Li, M. Anderson, C. Walthall, P. Doriaswamy and E.R. Hunt. 2004. Vegetation water content mapping using Landsat data derived normalized difference water index for corn and soybeans. *Remote Sensing of Environment* 92:475–482.

Jagirdar, V. V. and M. W. Trikande. 2019. Terrain accessibility prediction for a new multi-axle armored wheeled vehicle. *Defence Science Journal* 69(2):195–200. https://doi.org/10.14429/dsj.69.12076.

Kennedy, J. G., E. S. Rush, G. W. Turnage and P. A. Morris. 1988. Updated soil moisture-strength prediction (SMSP) methodology. *Technical Report GL-88-13*. Vicksburg, Miss.: US Army Engineer Waterways Experiment Station.

Knight, S. J. 1961. Some factors affecting moisture content-density-cone index relations. *Miscellaneous Paper No. 4457*, Nov. 1961. Vicksburg, Miss.: US Army Engineer Waterways Experiment Station.

McFeeters, S. K. 1996. The use of the Normalized Difference Water Index (NDWI) in the delineation of open water features. *International Journal of Remote Sensing* 7(7):1425–1432.

Mason, L. M and E. A. Baylot. 2016, Predicting soil strength in terms of cone index and California Bearing Ratio for trafficability. *ERDC/GSL TN-16-1*. Vicksburg, Miss.: Engineer Research and Development Center, Vicksburg.

Owe, M., B. Choudhury and J. Ormsby. 1989. Large area variability in climate-based soil moisture estimates and implications for remote sensing. *GeoJournal* 19(2):177–183.

Pokonieczny, K. and M. Rybanský. 2018. Method of developing the maps of passability for unmanned ground vehicles. Pages 24–25 in *Proceedings of the 9th IGRSM International Conference and Exhibition on Geospatial & Remote Sensing*, held in Kuala Lumpur, Malaysia, 24–25 April 2018.

Pundir, S. K. and R. D. Garg. 2020b. Development of rule based approach for assessment of off road trafficability using remote sensing and ancillary data. *Quaternary International*. https://doi.org/10.1016/j.quaint.2020.07.017.

Pundir, S. K. and R. D. Garg. 2020a. Development of mapping techniques for off road trafficability to support military operation. *Spatial Information Research*. https://doi.org/10.1007/s41324-019-00310-z.

Pundir, S. K. and R. D. Garg. 2021. Development of empirical relation to assess soil spatial variability for off-road trafficability using terrain similarity analysis and geospatial data. *International Journal Remote Sensing Letters* 12:3, 259–268. https://doi.org/10.1080/2150704X.2021.1880657.

Pundir, S. K. and R. D. Garg. 2022. A comprehensive approach for off-road trafficability evaluation and development of modified equation for estimation of RCI to assess regional soil variation using geospatial technology. *Quaternary Science Advances* 5(2022):100042. https://doi.org/10.1016/j.qsa.2021.100042.

Rybansky, M., A. Hofmann, M. Hubacek, V. Kovarik and V. Talhofer. 2014. The impact of terrain on cross country mobility-geographic factors and their characteristics. In *Proceedings of the 18th International Conference of the ISTVS*, held in Seoul, South Korea, 22–25 September, 2014.

Sanchez-Ruiz, S., M. Piles, N. Sanchez, J. Martinez-Fernandez, M. Vall-llossera and A. Camps. 2014. Combining SMOS with visible and near/shortwave/thermal infrared satellite data for high resolution soil moisture estimates. *Journal of Hydrology* 516:273–283.

Sellers, P. J., Y. Mintz, Y. C. Sud and A. Dalcher. 1986. A simple biosphere model (SIB) for use within general circulation models. *Journal Atmospheric Sciences* 43:505–531.

Singh, A. K., A. S. Jasrotia, A. K. Taloor, B. S. Kotlia, V. Kumar, S. Roy, P.K.C. Ray, K. K. Singh, A. K. Singh and A. K. Sharma. 2017. Estimation of quantitative measures of total water storage variation from GRACE and GLDAS-NOAH satellites using geospatial technology. *Quaternary International* 444:191–200.

Stevens, M. T., G. B. McKinley and F. Vahedifard. 2017. Full-featured ground vehicle mobility analysis using different soil moisture sources. *International Journal of Vehicle Performance* 3(1):19–35. https://doi.org/10.1504/IJVP.2017.081262.

Sullivan, P. M., N. A. Renfroe, M. R. Albert, G. G. Koening, L. Peck and K. O'Neill. 1997. Soil moisture strength prediction model version II (SMSP II). *TR GL-97-15*. Vicksburg, Miss.: US Army Engineer Waterways Experiment Station.

Taloor, A. K., R. A. Pir, N. Adimalla, S. Ali, D. S. Manhas, S. Roy and A. K. Singh. 2020.Spring water quality and discharge assessment in the Basantar watershed of Jammu Himalaya using geographic information system (GIS) and water quality Index(WQI). *Groundwater for Sustainable Development*. https://doi.org/10.1016/j.gsd.2020.100364.

US Army and US Air Force. 1994. *Army Field Manuals—Planning and Design of Roads, Airfields, and Heliports in the Theater of Operations.* FM 5-430-00-1, Ch. 7, *Soils Trafficability*. Washington DC: Headquarters of the US Army and US Air Force.

Van Lopik, J. R. and C. R. Kolb. 1959. A technique for preparing desert terrain analogues. Vicksburg, Miss.: US Army Engineer Waterways Experimental Station, Corps of Engineers, 104p.

Wong, K. W., M. Khoury and T. Thornburn. 1977. Automatic soil identification from remote sensing data. *Photogrammetric Engineering and Remote Sensing* 43(1):73–80.

Wright, R. C. and J. R. Burns. 1968. *Mobility Environmental Research Study. A Quantitative Method for Describing Terrain for Ground Mobility,* Vol. 2. Surface Composition, No. AEWES-TR-3-726-VOL-2. Vicksburg, Miss.: Army Engineer Waterways Experiment Station.

IN-PRESS ARTICLES

Yanzhe Shi, Yumin Tan, Yunxin Li, Bo Xu. Automatic registration method of multi-source point clouds based on building facades matching in urban scenes.

Muhammad Nasar Ahmad, Shao Zhengfeng, Andaleeb Yaseen, Muhammad Nabeel Khalid, Akib Javed. The simulation and prediction of Land Surface Temperature based on SCP and CA-ANN models using Remote sensing data: A case study of Lahore.

Yan Lv, Hongwei Guo, Shuanggen Jin, Lu Wang, Haiyi Bian, and Haijian Liu. Permanganate index variations and factors in Hongze Lake from Landsat-8 images based on machine learning.

Songjing Guo, Xueling Wu, Ruiqing Niu, and Wenfu Wu. Exploring spatiotemporal variations and driving factors of urban comprehensive carrying capacity in the Yangtze River Delta urban agglomeration.

Clement Akumu, Sam Dennis. Exploring the Addition of Airborne Lidar-DEM and Derived TPI for Urban Land Cover and Land Use Classification and Mapping.

Zhigang Deng, Xiwei Fan, Jian Chen. A machine learning method for building height estimation based on Sentinel-2 bi-temporal images.

Ji Won Suh, William B Ouimet. Generation of High-Resolution Orthomosaics from Historical Aerial Photographs using Structure-from-Motion (SfM) and Lidar data.

Muhammad Nasar Ahmad, Zhenfeng Shao, Akib Javed, Fakhrul Islam, Hafiz Haroon Ahmad, Rana Waqar Aslam. The Cellular Automata approach in dynamic modelling of land use change detection and future simulations based on Remote Sensing Data in Lahore Pakistan.

Firat Erdem, Nuri Erkin Ocer, Dilek Kucuk Matci, Gordana Kaplan, Ugur Avdan. Apricot Tree Detection from UAV-Images Using Mask R-CNN and U-Net.

Batuhan Sariturk, Damla Kumbasar, Dursun Zafer Seker. Comparative Analysis of Different CNN Models for Building Segmentation from Satellite and UAV Images.

The Use of Indices and Modified U-Net Network in Improving the Classification of Planting Structures

Weidong Li, Fanqian Meng, Linyan Bai, Yongbo Yu, Inam Ullah, Jinlong Duan, and Xuehai Zhang

Abstract

It was difficult to accurately obtain crop planting structure by using the spectral information of high spatial resolution and low spatial resolution multispectral images of panchromatic images at the same time. In this paper, we propose a method of planting structure extraction based on indices and an improved U-Net semantic segmentation network. Based on the original band of Landsat-8, we used an image fusion algorithm to highlight the characteristics of vegetation, water, and soil respectively by three indices added, and the improved U-Net network was used to classify the type of planting structure. The results showed that the overall accuracy of classification was more than 91.6%, and the accuracy of crops was up to 93.8%. Automated water extraction index in image fusion effectively improved the classification accuracy. This method could extract a variety of information about planting structures automatically and accurately. It provided theoretical support for adjusting and optimizing regional planting structures.

Introduction

The classification of crop planting structures based on remote sensing has the capabilities of large-area detections and rapid imaging. This type of classification is a high-tech method used to quickly determine the crop planting structure. In recent years, high-spatial resolution remote sensing satellites have developed rapidly (Wardlow and Egbert 2008; Xiong and Huang 2009; Xu *et al.* 2014; Zhang *et al.* 2014). High-spatial resolution remote sensing images can be used as data sources to more accurately detect crop planting structures (Bai *et al.* 2019; Baojia *et al.* 2019; Shuang 2018; Xiong and Zhang 2019). Traditional methods such as decision tree classifications and normalized difference vegetation index (NDVI) curves can extract only shallow features and cannot integrate multiple source images, making it impossible to effectively improve the accuracy when obtaining planting structure information (Lin *et al.* 2018; Shu-Kui *et al.* 2016; Yang *et al.* 2018). The traditional technique of remote sensing image classification firstly requires feature extraction such as texture and geometry of the ground object target (Wang 1990), and then carries out classification calculation. However, this classification method relies on feature representation, expert knowledge, and weak generalization ability, so it cannot be applied to complex large samples of high-resolution remote sensing images (Atkinson *et al.* 2000; Li *et al.* 2014).

With the development of machine learning, neural networks (NNs) (Pacifici *et al.* 2009), support vector machines (Huang and Zhang

Weidong Li, Yongbo Yu, Inam Ullah, Jinlong Duan, and Xuehai Zhang are with College of Information Science and Engineering, Henan University of Technology, Zhengzhou 450001, China (wdli@haut.edu.cn).

Fanqian Meng is with College of Marine Technology, Faculty of Information Science and Engineering, Ocean University of China, Qingdao 266100, China.

Linyan Bai is Aerospace Information Research Institute, Chinese Academy of Sciences, Beijing 100094.

2013), and other algorithms have been applied to classify high-resolution remote sensing images. Nevertheless, these are all shallow learning algorithms and cannot express complex functions well (Ball *et al.* 2017; Yang *et al.* 2017; Yuan *et al.* 2017). Therefore, these models cannot adapt to the semantic segmentation problems with large sample sizes and high complexities (Zhang *et al.* 2016). Convolutional neural networks (CNNs) have the advantages of automatic feature extraction and automatic classification, and they show significant benefits when analyzing remote sensing data (Mou *et al.* 2018a Zhao *et al.* 2017; Zhu *et al.* 2018). As critical network models in semantic segmentation research, fully convolutional neural networks (FCNs) are widely used for high-resolution remote sensing images (Fu *et al.* 2017; Long *et al.* 2015; Mou *et al.* 2018b; Shrestha *et al.* 2018). Many scholars have transformed and developed FCNs, creating a series of convolution-based segmentation models, including SegNet (Badrinarayanan *et al.* 2017), U-Net (Ronneberger *et al.* 2015), DeepLab (Chen *et al.* 2018), multi-scale FCN (Lin *et al.* 2017), among which U-Net can achieve the highest number of samples with predicted results (Flood *et al.* 2019; Haiou *et al.* 2019; Nakai *et al.* 2020; Xu *et al.* 2020; Yue *et al.* 2019). In recent years, researchers have also proposed integrating long short-term memory networks into the U-Net structure to enhance temporal information between diachronic images (Shi *et al.* 2021). In addition, a mapping network (CASNet) is constructed through a deep context-aware sub-pixel to better preserve the geometric structures in the data (He *et al.* 2022).

The subtle features of some planting structures are only visible on high-resolution panchromatic images (PANs) of the corresponding spectral images. These features are challenging to recognize using low-spatial-resolution multispectral images (MSIs). When using traditional methods to classify spectral images, it is challenging to make full use of the high spatial resolutions of PANs and the rich spectral information of MSIs to accurately obtain crop planting structures. At present, the commonly used image fusion methods are hue, luminance, and saturation transformation, Gram-Schmidt transformation (GS), principal component analysis, the nearest-neighbor diffusion fusion algorithm (NND), the UNB fusion algorithm (UNB), wavelet transform (WT), etc. The image spectral fidelity after GS fusion is high (Chen *et al.* 2019; Jiwei *et al.* 2017; Sun *et al.* 2014; Yalan *et al.* 2018; Yang *et al.* 2018), so this paper uses the GS fusion method for the image fusions.

The above research mainly used a single-spatial-resolution data source to select training images. In order to classify single crops and other ground objects, the methods of crop classification based on deep learning mostly adopt binary classification algorithms (Gilcher *et al.* 2019). Based on the above-mentioned research, indices are seldom used to increase spectral complexity (Bouguettaya *et al.* 2022), resulting in serious misclassification in marginal areas. In this paper, we propose a combined index and image fusion approach to optimize the classification of hybrid regions and improve the image spectral

complexity and spatial resolution. Meanwhile, we improve the U-Net network model, can recognize multiple types of features in one training, reduce misclassification, and raise the accuracy of crop identification. The other benefit of the improved U-Net network is decreasing the volume of weight files and raising the training efficiency. In terms of network selection, the depth and weight file size were often selected to be more in-depth. A more extensive semantic segmentation network was not conducive to being popularized.

Data
This article takes the Xiaokaihe Irrigation District in Binzhou City, Shandong Province, China (Figure 1) as an example and uses *Landsat-8* remote sensing image data acquired on May 18, 2018, to carry out a study on an index-based and improved U-Net network classification method. The latitude and longitude of the Xiaokaihe Irrigation Area are longitude: 116.04°E–118.68°E, latitude: 36.40°N–38.52°N.
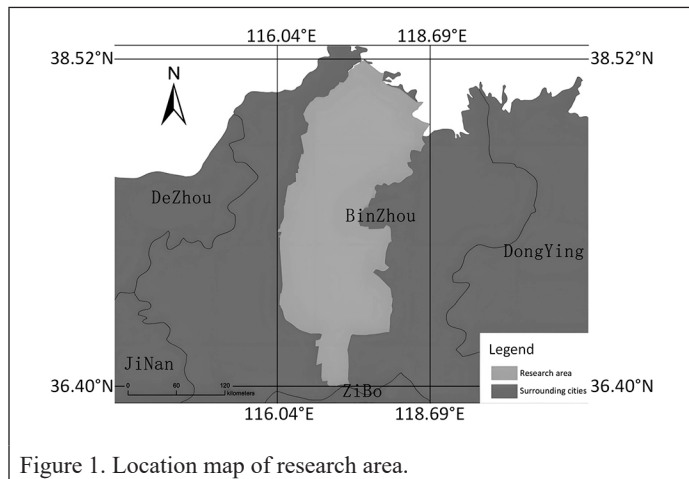
Figure 1. Location map of research area.

A field survey was conducted in the crop planting region of the study area in mid-May, and the classification data of the planting structure were manually produced according to the survey results to ensure their accuracy. The main crop types in the study area in mid-May included three types of winter wheat at the filling stage, cotton at the seedling stage, and jujube trees. According to the needs of management in the irrigation area, we need to classify the similar surface features in the area. They were divided into five categories: cotton, wheat, cities, forest, and water.

In this study, we use the real label data to make a verification set of 128 × 128 pixel slices of the training images. As training data, 80% of the verification set photographs and one-to-one correspondence are randomly selected to make the training set for training the network. The other 20%, constituting the test set data, are used to evaluate the results.

Method

Index Selection
It is difficult to accurately describe and distinguish the spectral characteristics of many types of different features based on original remote sensing image data. This paper selects NDVI, automated water extraction index (AWEI), and soil-regulated vegetation index (SAVI) to synthesize 1–7-band remote sensing images based on different index characteristics to increase the spectral complexity. Among them, NDVI and SAVI can effectively distinguish the spectral differences among vegetation types and the difference between plants and soil. AWEI can efficiently identify water. The selection of these three indices has positive significance for the classification of planting structures in irrigated areas (Curran *et al.* 1983; Huete *et al.* 1988).

Normalized Difference Vegetation Index
The NDVI is based on the characteristics of chlorophyll in vegetation. Chlorophyll has a lower reflectance in the visible light band, while its reflectance in the red band and green band are relatively high. The reflectance gradually decreases in the near-infrared (NIR) band to the mid-infrared group. The formula used to construct the most representative normalized difference vegetation index is as shown in Equation 1 (Curran *et al.* 1983):

$$NDVI = \frac{NIR-RED}{NIR+RED} \qquad (1)$$

Where NIR is the near-infrared band reflectance and RED is the red band reflectance.

NND Image Fusion Method
The AWEI improves factors such as low classification accuracies in water extractions and relatively small threshold selections. AWEInsh is an index formulated to effectively eliminate nonwater pixels, including dark built surfaces in areas with urban backgrounds, and AWEIsh is primarily formulated for further improvement of accuracy by removing shadow pixels that AWEInsh may not effectively eliminate. AWEIsh is more suitable for scenes with shadows than AWEInsh. AWEIsh is selected as the synthetic element and is hereafter referred to as AWEI (Feyisa *et al.* 2014). The expression is as shown in Equation 2 and Equation 3:

$$AWEInsh = \frac{4*(GREEN-SWIR1)}{0.25*NIR+0.75*SWIR2} \qquad (2)$$

$$AWEIsh = BLUE + 2.5 * GREEN - 1.5*(NIR-SWIR1) - 0.25*SWIR2 \quad (3)$$

Where BLUE is the blue band, SWIR1 and SWIR2 are the shortwave infrared bands, and AWEIsh is more suitable for scenes with shadows than AWEInsh. In this paper, to better distinguish the boundary pixels between the water and the ground features, AWEIsh is selected as the synthetic element and is hereafter referred to as AWEI.

Soil Regulation Vegetation Index
The SAVI introduces soil adjustment factors to improve the normalized index's identification ability under different soil backgrounds. The formula is as shown in Equation 4 (Huete *et al.* 1988):

$$SAVI = \frac{(NIR-RED)*(L+1)}{NIR+RED+L} \qquad (4)$$

where L is the vegetation cover corresponding to the soil adjustment factor, 0 is no vegetation, and 1 is complete vegetation coverage. According to the study area's situation, this paper selects the best factor value in the range of 0.3–0.8 with $L = 0.5$.

Image Fusion
A single remote sensing image cannot have both high spectral resolution and high spatial resolution. Therefore, the remote sensing image fusion technique is an effective method to solve this problem (Yue *et al.* 2019).

In this paper, the GS image fusion method (Chen *et al.* 2019) was selected since it provides more valuable spectral feature information with a deep semantic segmentation network (Figure 2). That is to improve the classification accuracy of the planting structure.

The Improved U-Net Convolutional Neural Network
The traditional U-Net network (Ronneberger *et al.* 2015) model has a long training period, a significant weight file, and a high production cost. It is not conducive to the automatic or accurate classification of planting structures. In this paper, a depth-separable convolution module is proposed to replace the full convolution method in the original network model. In order to improve the stability of training and the accuracy of optimization prediction, the Mish activation function is used instead of the ReLU activation function (Shu-Kui and Jing 2016).

Depthwise Separable Convolution

In this paper, depth-separable convolution and pointwise convolution are used to extract features (Guo *et al.* 2018). Compared with conventional convolution operations, the number of parameters and operational cost of this method is relatively low. Depth-separable convolution effectively reduces the number of required parameter calculations. The parameter values are obtained by adding the two parts, consisting of approximately one-third of the conventional convolution calculation burden. Depth-separable convolution considers both channel and regional changes, while the conventional convolution method only considers the region first and then considers the channel, separating the channel and region.

Mish Activation Function

In this article, the ReLU activation function is replaced in the U network with a smooth, unbounded Mish function to avoid saturation due to overwriting. In other words, positive values can reach any height. This continuous activation function allows better information to penetrate deep into the neural network, resulting in better accuracy and generalization abilities (Misra 2019).

Theoretically, slightly negative values allow better gradient flows compared to the hard zero boundaries applied in ReLU; this characteristic further improves the efficiency and accuracy of the operation. x is the input value. The formula of the Mish function (Misra 2019) is as shown in Equation 5:

$$\text{Mish} = x * \tanh(1 + e^x) \qquad (5)$$

The Improved U-NET Network Model

In this paper, a deep, separable convolution module is used to replace the full convolution method. A Mish activation function is used to restore the ReLU activation function to design an improved U-Net network model. Subsequent research shows that the improved network model is more classified than the traditional U-Net model when predicting the planting structure. The accuracy is further optimized, and the model structure is shown in the Figure 3 below.

Network Training Process

The entire set of pairs of images and labels is input into the U-Net model and fitted in a long iteration process that includes training the network model and predicting the classifications. The training data set is input into the network model for training, and the trained weight file is used to predict the test set to obtain the classification results. The training and prediction processes are shown in Figure 4. This article uses the Keras Python deep learning library and TensorFlow back-end driver (Abadi *et al.* 2016) to achieve the model building, training, and prediction processes.

Method of Evaluation

In this paper, the accuracy, recall rate, mean of the two reconciled values, and kappa coefficient are used as indicators of the evaluation method. These indicators are calculated based on the confusion matrix, and the Precision calculated as shown in Equation 6 (Fu *et al.* 2017):

$$\text{Precision} = \frac{1}{6}\sum_i C_{ii} \Big/ \sum_j C_{ij} \qquad (6)$$

Figure 2. Flow chart of G-S fusion.

Figure 3. The improved U-Net network model.

Figure 4. Flow chart of U-Net image prediction.

(a) **(b)** **(c)**

Figure 5. Results of U-Net and its improved models obtained from a comparison diagram (a) U-Net training accuracy rate curve; (b) Separable-UNet training accuracy rate curve; (c) Mish-Separable-UNet training accuracy rate curve.
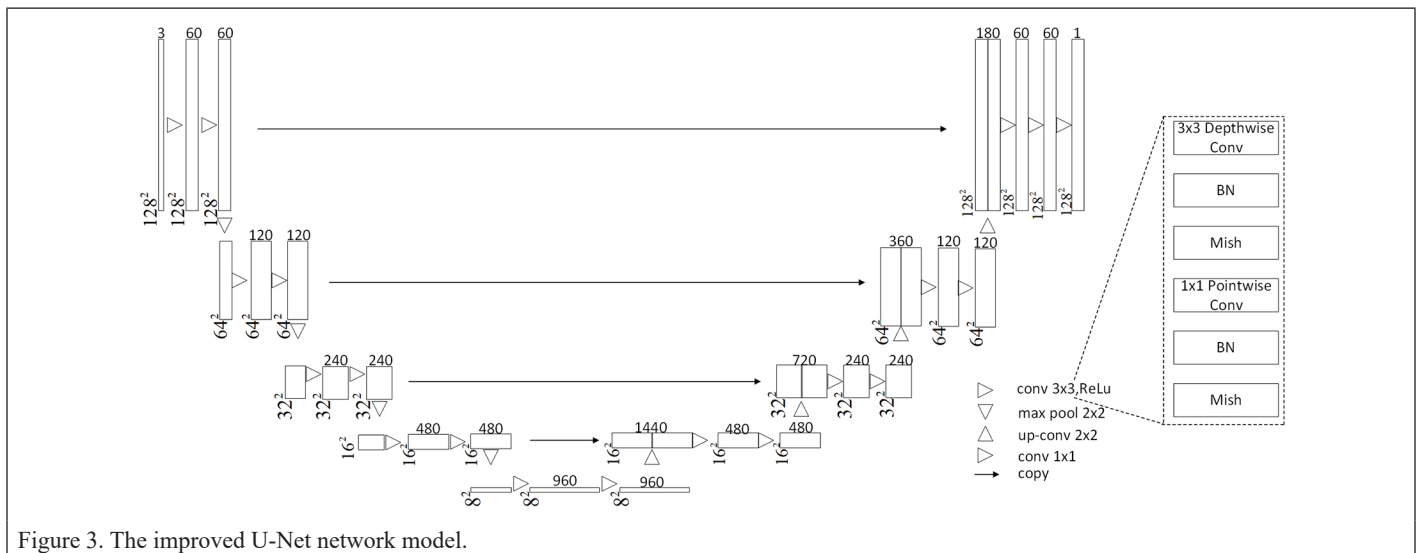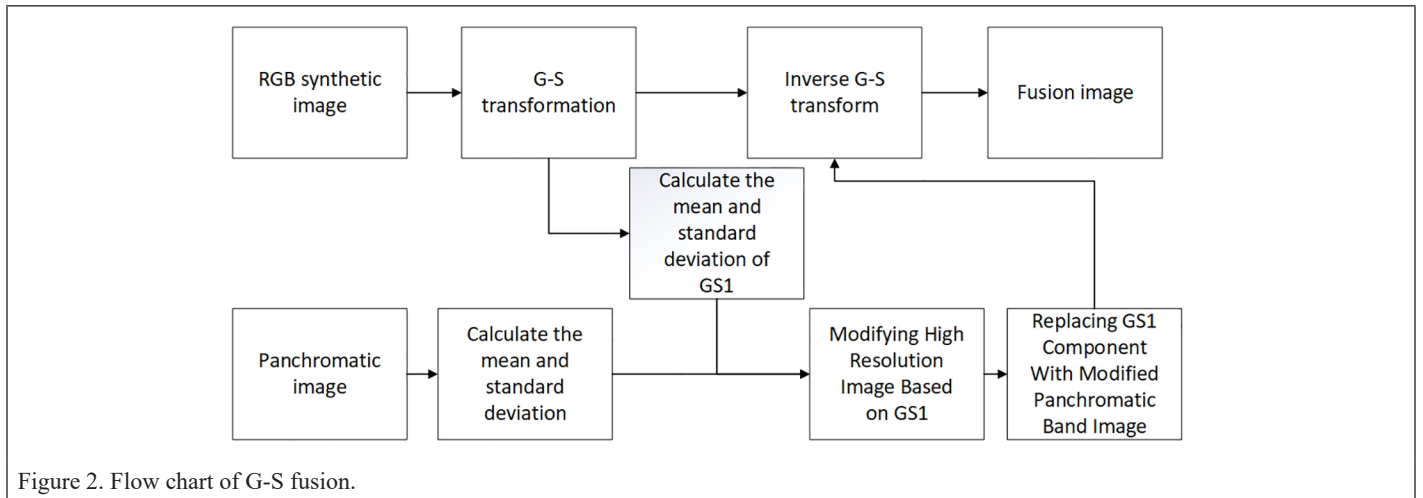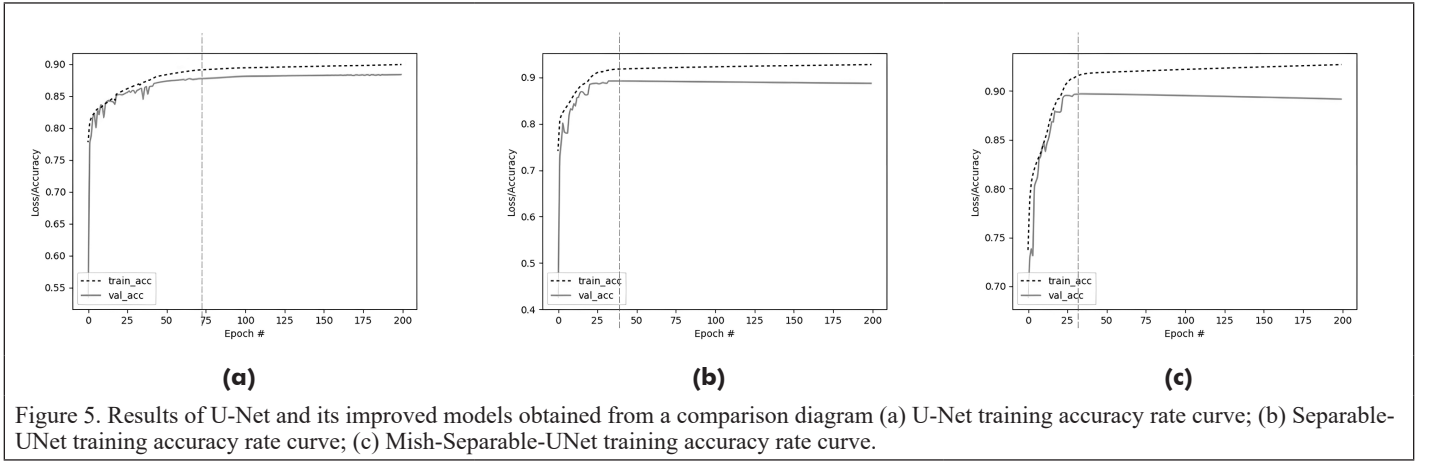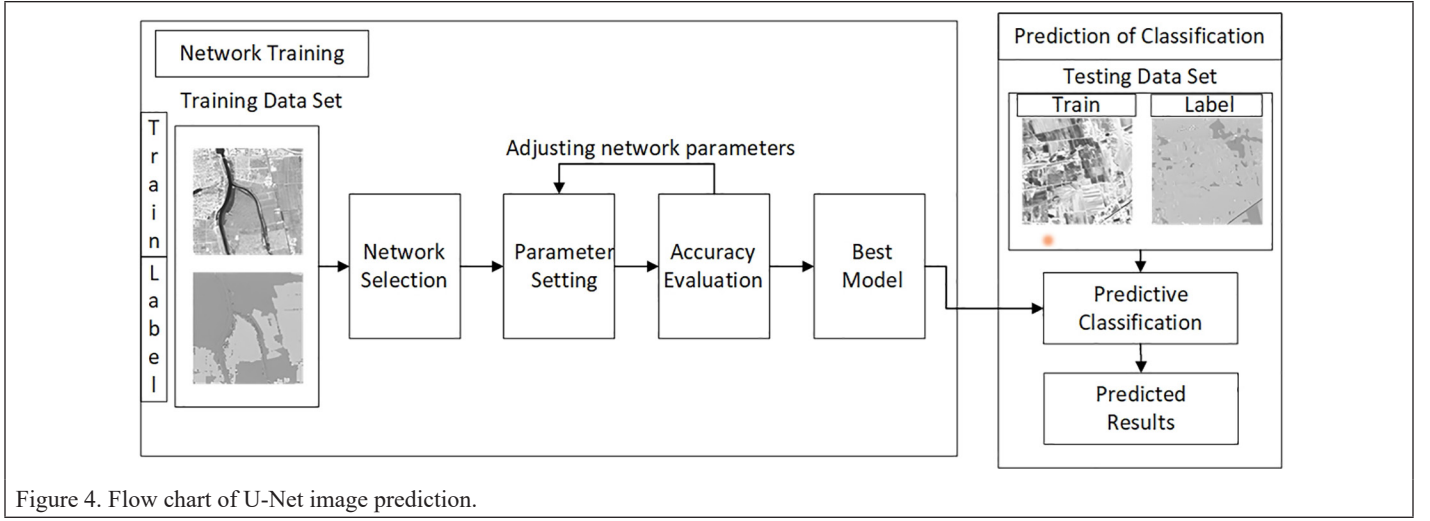
where C_{ii} indicates the number of correctly classified samples and C_{ij} suggests type-I samples that are mistaken for type J.

The recall metric represents the correct average proportion of pixels classified into a given category. The Recall is calculated as shown in Equation 7:

$$\text{Recall} = \frac{1}{6}\sum_i C_{ii} \Big/ \sum_i C_{ij} \tag{7}$$

The model can also be further evaluated by calculating the harmonic mean F1 of the F accuracy and recall rate. The F1 value is calculated as shown in Equation 8:

$$\text{F1} = 2 * \frac{\text{Precision} * \text{Recall}}{\text{Precision} + \text{Recall}} \tag{8}$$

The kappa coefficient measures the consistency between the predicted class and the artificial label. The Kappa coefficient is calculated as shown in Equation 9 (Zhang *et al.* 2018):

$$\text{Kappa} = \frac{\dfrac{\dfrac{1}{6}\sum_i c_{ii}}{\sum_{i=1}^{6}\sum_{j=1}^{6} c_{ij}} - \dfrac{\dfrac{1}{6}\sum_i c_{ii}\sum_i c_{ij}}{\left(\sum_{i=1}^{6}\sum_{j=1}^{6} c_{ij}\right)^2}}{1 - \dfrac{\dfrac{1}{6}\sum_i c_{ii}\sum_i c_{ij}}{\left(\sum_{i=1}^{6}\sum_{j=1}^{6} c_{ij}\right)^2}} \tag{9}$$

Some parameters in the formula are modified according to the actual situation.

Results and Discussion

In the current study, the classification effect of the U-Net deep semantic segmentation network on the planting structure was found to be better than those of the FCN network and the SegNet network model. Therefore, in this section, only U-Net and its improved models were compared and analyzed. Furthermore, the conventional U-Net model, the U-Net model with an added deep, separable convolution module, and the activation function network model were trained in 200 batches on the same test data set to obtain the accuracy curves shown in Figure 5.

Compared with the traditional U-Net model, after adding the depth-separable convolution module, the model reaches an overfitting batch from 70 to 30, significantly reducing the calculation cost and increasing the fitting rate (Guo *et al.* 2018). After using the Mish activation function, the accuracy and calculation rate slightly increased due to the smoothing characteristics of the function (Misra 2019). The improved network model achieves lighter parameters, and the weight file size is reduced from 303 MB to 53 MB, a reduction of 82.5%, significantly improving the production cost.

The original remote sensing images of seven bands from 1 to 7 are synthesized with 1, 2, and 3 exponents. Then, the GS method is used to fuse the panchromatic groups to further increase the spatial resolution and spectral richness of the training images and predict the results, as shown in Figure 6.

The statistical test set prediction results are compared with the label data to generate the confusion matrices (Odena 2016) shown in Figure 7 to judge the classification quality of the planting structure.

Table 1 compares the prediction results of the various methods with the actual label data to calculate the accuracy rate. After the investigation, most of the woodland area is found to comprise economic crops such as jujube trees, wheat, woodland, and cotton areas were classified as crop areas.

Figure 6. Classification Results (a) seven-band classification results; (b) synthetic normalized difference vegetation index (NDVI) classification results; (c) synthetic automated water extraction index (AWEI) classification results; (d) artificial soil-regulated vegetation index (SAVI) classification results; (e) synthetic NDVI and AWEI classification results; (f) Synthesis of NDVI and SAVI classification results; (g) Synthesis of AWEI and SAVI classification results; (h) Synthesis of three index classification results.

As shown in Table 1, the overall accuracy of the 7-band fusion image without the addition of any index reached 90.3%, and the accuracy of increasing the index image participation in the image fusion process was higher than that obtained without the index. Adding the index uses

Figure 7. Statistics of confusion types.
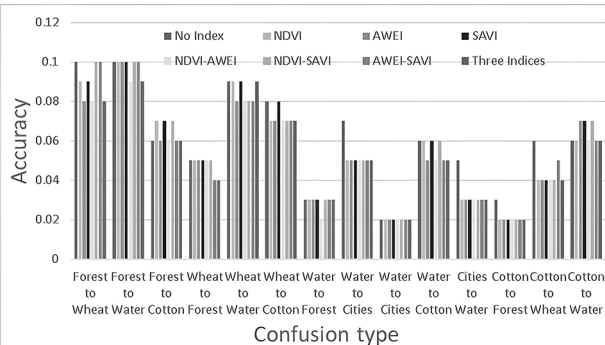
Table 1. Classification accuracy statistical table.

Index	Water (%)	Wheat (%)	Forest (%)	Cities (%)	Cotton (%)	Crops (%)	Accuracy (%)
No Indices	80.6	77.5	71.0	95.0	86.9	81.7	90.3
SAVI	80.3	84.4	69.7	93.3	85.6	82.4	91.6
NDVI	81.4	84.3	73.8	92.8	86.6	83.5	92.4
NDVI, SAVI	81.0	82.3	73.8	93.1	87.2	83.4	92.6
AWEI	81.4	83.9	74.2	93.9	88.2	84.1	92.7
AWEI, SAVI	82.1	81.8	74.4	93.5	87.5	83.9	93.3
NDVI, AWEI	81.8	85.2	74.4	93.5	87.5	84.2	93.7
Three Indices	81.5	85.3	74.1	93.0	87.8	84.1	93.8

SAVI = soil-regulated vegetation index; NDVI = normalized difference vegetation index; AWEI = automated water extraction index.

the improved U-Net network in the training process for identifying crop cultivation areas. The structural classification has a positive effect on the results.

With the addition of each of the three indices individually, all showed an increase in the overall accuracy rate, among which AWEI had the most significant impact on the classification of the planting structure. The crop identification accuracy was increased by 2.4%, and the city and water pixels were better identified. This index is superior to the other two indices, which reached accuracies of 81.4% and 93.9%, and the improvement effect is visible. The overall accuracy rate reaches 92.7%, which is the best among the three indices. However, this index tends to judge pixels as cotton when recognizing mixed pixels of wheat and cotton, and its ability to identify crops in a large mixed area remains to be discussed.

Under the condition of two-index 9-band fusion images, AWEI still plays an important role. The classification effect of training images containing AWEI is better than that of the NDVI-SAVI 9-band fusion images. The addition of NDVI further improves the crop recognition ability of AWEI and the mutual recognition ability among crops. The accuracy rates of the three types of plants, wheat, cotton, and woodland, increased to 85.2%, 74.4%, and 87.5%, respectively. At the same time, this method also guarantees that the high recognition accuracy of water and cities reaches 81.8% and 93.5%, respectively. Only the water identification efficiency is lower than that of the AWEI-SAVI method, with a difference of 0.3%, and the overall accuracy rate of this method reaches 93.7%.

Compared with the NDVI-AWEI 9-band fusion image method, the overall accuracy of the 10-band fusion image is improved by only 0.1%, and the crop classification recognition is reduced. SAVI's improvement in the fusion image is limited. Considering the production costs, the priority is lower. In summary, the NDVI-AWEI 9-band fusion image method combined with the improved U-Net network model classification planting structure method has advantages.

This paper evaluates the reliability and accuracy of the planting structure classification results of each index method combined with the improved U-Net model by calculating the kappa coefficient, precision, recall, and harmonic mean F1, as shown in Table 2 below. Compared with nonindexed images, the classification accuracy of the indexed fusion image planting structure is significantly improved. The kappa coefficient increases from 0.868 to more than 0.874 with the addition of the index, further improving the consistency between the predicted class and the artificial label. The accuracy, recall, and average value are enhanced by more than 0.02. In the new method, the NDVI-AWEI fusion method has the same accuracy as the three-index method, reaching 0.873. The kappa coefficient and F1 value are better than the three-index method, at 0.886 and 0.872, respectively; thus, this method can provide accurate and stable classification results of the crop planting structure.

Table 2. Statistics of each method.

Band	Index	Precision	Recall	F1	Kappa
7	No Indices	0.853	0.851	0.852	0.868
	NDVI	0.866	0.865	0.865	0.880
8	AWEI	0.871	0.869	0.870	0.885
	SAVI	0.861	0.856	0.858	0.874
	NDVI, AWEI	0.873	0.871	0.872	0.886
9	NDVI, SAVI	0.863	0.862	0.863	0.878
	AWEI, SAVI	0.868	0.867	0.867	0.882
10	Three Indices	0.873	0.869	0.871	0.885

SAVI = soil-regulated vegetation index; NDVI = normalized difference vegetation index; AWEI = automated water extraction index.

As shown in Figure 6, the classification confusion in the boundary areas of feature types is still the primary source of error. Figure 7 shows the statistics of the confusion types and their probabilities under various methods.

Due to the increase in spectral richness and the information contained in the training images, the feature information extracted using the improved U-Net network is enhanced to a certain extent (Flood *et al.* 2019; Fu *et al.* 2017). The overall confusion rate of the prediction results declines, but the edge is not fundamentally resolved. Regarding misclassifications, forest pixels still maintain the highest probability of confusion due to their discrete nature. Using the improved U-Net network to train the NDVI-AWEI 9-band fusion image method compared to other means, the minimum confusion level in each misjudgment type can be maintained at 2%–9%, representing the improved U-Net model planting structure classification model.

Conclusion

This paper proposes a method for planting structure classification based on exponential and improved U-Net deep semantic segmentation network. High spatial resolution GS fusion images highlighting different features are obtained by combining multiple index data and *Landsat-8* original remote sensing images, combined with improved U-Net deep semantic segmentation network realizes the classification of crop planting structure.

This study proposes a method for classifying planting structures based on an exponential and improved U-Net deep semantic segmentation network. High-spatial-resolution GS-fusion images highlighting different features are obtained by combining multiple index data and *Landsat-8* original remote sensing images with an improved U-Net deep semantic segmentation network to classify crop planting structures.

This research shows that, compared with the unfused index data, the crop classification accuracy of the proposed method is more than 82.4%, and the overall efficiency of the categorization of features (including rivers, towns, etc.) is more than 91.6%. The NDVI-AWEI method has a kappa coefficient of 0.886, and its accuracy is above 0.873. Compared with the three-index method, less synthetic data is required, the training data set is smaller, and the production cost is lower. Among the three indices, AWEI has the highest classification accuracy for images. The method based on the combined NDVI-AWEI indices and improved U-Net network is the most suitable for the automatic and accurate classification of planting structures.

Further improvements to this method are expected to continue to improve the classification accuracy of planting structures through the following two aspects: (1) we will attempt to use the CNN network to construct a fusion algorithm to optimize the image fusion process and retain more detailed spectral information; and (2) we will attempt to use other indices joined in the fusion image process to further strengthen the different images and meta-weight distributions to reduce boundary confusion and obtain a better classification performance.

References
Abadi, M., A. Agarwal, P. Barham, E. Brevdo, Z. Chen, C. Citro, G. S. Corrado, A. Davis, J. Dean, M. Devin, S. Ghemawat, I. Goodfellow, A. Harp, G. Irving, M. Isard, Y. Jia, R. Jozefowicz, L. Kaiser, M. Kudlur, J. Levenberg, D. Mané, R. Monga, S. Moore, D. Murray, C. Olah, M. Schuster, J. Shlens, B. Steiner, I. Sutskever, K. Talwar, P. Tucker, V. Vanhoucke, V. Vasudevan, F. Viégas, O. Vinyals, P. Warden, M. Wattenberg, M. Wicke, Y. Yu and X. Zheng. 2016. Tensorflow: Large-scale machine learning on heterogeneous distributed systems. arXiv preprint arXiv:1603.04467. https://doi.org/10.48550/arXiv.1603.04467.

Atkinson, P. M. and P. Lewis. 2000. Geostatistical classification for remote sensing: an introduction. *Computers and Geosciences* 26(4):361–371. https://doi.org/10.1016/S0098-3004(99)00117-X.

Badrinarayanan, V., A. Kendall and R. Cipolla. 2017. Segnet: A deep convolutional encoder-decoder architecture for image segmentation. *IEEE Transactions on Pattern Analysis Machine Intelligence* 39(12):2481–2495. https://doi.org/10.1109/TPAMI.2016.2644615.

Bai, Y., J. Gao and B. Zhang. 2019. Extraction of crop planting structure based on time-series NDVI of landsat8 images. *Arid Land Geography* 42:893–901. https://doi.org/10.12118/j.issn.1000-6060.2019.04.21.

Ball, J. E., D. T. Anderson and C. S. Chan. 2017. Comprehensive survey of deep learning in remote sensing: Theories, tools, and challenges for the community. *Journal of Applied Remote Sensing* 11(4). https://doi.org/10.1117/1.JRS.11.042609.

Baojia, D. U., J. Zhang, Z. Wang, D. Mao, M. Zhang and W. U. Bingfang. 2019.Crop mapping based on Sentinel-2a NDVI time series using object-oriented classification and decision tree model. *Journal of Geo-Information Science* 21(5):740–751. https://doi.org/10.12082/dqxxkx.2019.180412.

Bouguettaya, A., H. Zarzour, A. Kechida and A. M. Taberkit. 2022. Deep learning techniques to classify agricultural crops through UAV imagery: A review. *Neural Computing and Applications* 34(12):9511–9536. https://doi.org/10.1007/S00521-022-07104-9.

Chen, L., G. Papandreou, I. Kokkinos, K. Murphy and A. L. Yuille. 2018. Deeplab: Semantic image segmentation with deep convolutional nets, atrous convolution, and fully connected CRFS. *IEEE Transactions on Pattern Analysis Machine Intelligence* 40(4):834–848. https://doi.org/10.1109/TPAMI.2017.2699184.

Chen, M., A. N. Puyang, J. Zhou and S. O. Geomatics. 2019. Gf-1 remote sensing image fusion and quality evaluation based on mountain area. *Beijing Surveying and Mapping* 3(6):249–254. https://doi.org/10.19580/j.cnki.1007-3000.2019.03.003.

Curran, P. 1983. Multispectral remote sensing for the estimation of green leaf area index. *Philosophical Transactions of the Royal Society of London. Series A, Mathematical and Physical Sciences* 309(1508):257–270. https://doi.org/10.1098/rsta.1983.0039.

Feyisa, G. L., H. Meilby, R. Fensholt and S. R. Proud. 2014. Automated water extraction index: A new technique for surface water mapping using Landsat imagery. *Remote Sensing of Environment* 140:23–35. https://doi.org/10.1016/j.rse.2013.08.029.

Flood, N., F. Watson and L. Collett. 2019. Using a U-Net convolutional neural network to map woody vegetation extent from high resolution satellite imagery across Queensland, Australia. *International Journal of Applied Earth Observation and Geoinformation* 82:101897. https://doi.org/10.1016/j.jag.2019.101897.

Fu, G., C. Liu, R. Zhou, T. Sun and Q. Zhang. 2017. Classification for high resolution remote sensing imagery using a fully convolutional network. *Remote Sensing* 9(6):498. https://doi.org/10.3390/rs9050498.

Guo, J., Y. Li, W. Lin, Y. Chen and J. Li. 2018. Network decoupling: From regular to depthwise separable convolutions. In *Proceedings 29th British Machine Vision Conference (BMVC 2018)*, held in Newcastle, UK, 3–6 September 2018. arXiv preprint arXiv:1808.05517.

Haiou, W., L. Hui, G. Qiang, D. Kai and C. Zhang. 2019. Design of Superpiexl U-Net network for medical image segmentation. *Journal of Computer-Aided Design and Computer Graphics* 31(6):1007–1017. https://doi.org/10.3724/SP.J.1089.2019.17389.

He, D., Q. Shi, X. Liu, Y. Zhong and L. Zhang. 2022. Generating 2m fine-scale urban tree cover product over 34 metropolises in China based on deep context-aware sub-pixel mapping network. *International Journal of Applied Earth Observation and Geoinformation* 106:102667. https://doi.org/10.1109/TGRS.2021.3085870.

Huang, X. and L. Zhang. 2013. An SVM ensemble approach combining spectral, structural, and semantic features for the classification of high-resolution remotely sensed imagery. *IEEE Transactions on Geoscience Remote Sensing* 51(1):257–272. https://doi.org/10.1109/TGRS.2012.2202912.

Huete, A. R. 1988. A soil-adjusted vegetation index (SAVI). *Remote Sensing of Environment* 25(3):295–309. https://doi.org/10.1016/0034-4257(88)90106-X.

Jiwei, C., S. Qian, Z. Li and W. Shuangting. 2017. Influence of different fusion methods based on GF images on the spectral fidelity of urban water. *Journal of Beijing Polytechnic University* 677(682):43. https://doi.org/10.11936/bjutxb2016070064.

Li, M., S. Zang, B. Zhang, S. Li and C. Wu. 2014. A review of remote sensing image classification techniques: The role of spatio-contextual information. *European Journal of Remote Sensing* 47(1):389–411. https://doi.org/10.5721/EuJRS20144723.

Lin, H., Z. Shi and Z. Zou. 2017. Maritime semantic labeling of optical remote sensing images with multi-scale fully convolutional network. *Remote Sensing* 9(5):480. https://doi.org/10.3390/rs9050480.

Lin, Y., S. Li and Z. Meng. 2018. Scene classification of multi-feature fusion remote sensing image based on clustering analysis. *Electronic Measurement Technology* https://doi.org/CNKI:SUN:DZCL.0.2018-22-019.

Liu, C., L. Hong, J. Chen, S. Chu and M. Deng. 2015. Fusion of pixel-based and multi-scale region-based features for the classification of high-resolution remote sensing image. *Journal of Remote Sensing* 19(2):228–239. https://doi.org/10.11834/jrs.20154035.

Long, J., E. Shelhamer and T. Darrell. 2015. Fully convolutional networks for semantic segmentation. Pages 3431–3440 in *Proceedings of the IEEE Conference on Computer Vision and Pattern Recognition*, held in Boston, Mass., 7–12 June 2015. https://doi.org/10.1109/CVPR.2015.7298965.

Gilcher, M., T. Ruf, C. Emmerling and T. Udelhoven. 2019. Remote sensing based binary classification of maize. Dealing with residual autocorrelation in sparse sample situations. *Remote Sensing* 11(18):2172. https://doi.org/10.3390/rs11182172.

Misra, D. 2019. Mish: A self regularized non-monotonic activation function. arXiv preprint arXiv:1908.08681. https://doi.org/10.48550/arXiv.1908.08681.

Mou, L. and X. X. Zhu. 2018a. RiFCN: Recurrent network in fully convolutional network for semantic segmentation of high resolution remote sensing images. arXiv preprint arXiv:1805.02091. https://doi.org/10.48550/arXiv.1805.02091.

Mou, L. and X. X. Zhu. 2018b. Vehicle instance segmentation from aerial image and video using a multitask learning residual fully convolutional network. *IEEE Transactions on Geoscience and Remote Sensing* 56(11):6699–6711. https://doi.org/10.1109/TGRS.2018.2841808.

Nakai, H., M. Nishio, R. Yamashita, A. Ono, K. K. Nakao, K. Fujimoto and K. Togashi. 2020. Quantitative and qualitative evaluation of convolutional neural networks with a deeper u-net for sparse-view computed tomography reconstruction. *Academic Radiology* 27(4):563–574. https://doi.org/10.1016/j.acra.2019.05.016.

Odena, A. 2016. Semi-supervised learning with generative adversarial networks. arXiv preprint arXiv:1606.01583. https://doi.org/10.48550/arXiv.1606.01583.

Pacifici, F., M. Chini and W. J. Emery. 2009. A neural network approach using multi-scale textural metrics from very high-resolution panchromatic imagery for urban land-use classification. *Remote Sensing of Environment* 113(6):1276–1292. https://doi.org/10.1016/j.rse.2009.02.014.

Ronneberger, O., P. Fischer and T. Brox. 2015. U-net: Convolutional networks for biomedical image segmentation. In *International Conference on Medical Image Computing and Computer-Assisted Intervention*, 234–241. Berlin, Heidelberg: Springer. https://doi.org/10.1007/978-3-662-54345-0_3.

Shi, Q., M. Liu, S. Li, X. Liu, F. Wang and L. Zhang. 2021. A deeply supervised attention metric-based network and an open aerial image dataset for remote sensing change detection. *IEEE Transactions on Geoscience and Remote Sensing* 60: 1–16. https://doi.org/10.1016/j.jag.2021.102667.

Shrestha, S. and L. Vanneschi. 2018. Improved fully convolutional network with conditional random fields for building extraction. *Remote Sensing* 10(7):1135. https://doi.org/10.3390/rs10071135.

Shu-Kui, B. O. and Y. J. Jing. 2016. One-class information extraction from remote sensing imagery based on nearest neighbor rule. *Computer Science* 43(Z6):217–218, 259. https://doi.org/10.11896/j.issn.1002-137X.2016.6A.052.

Shuang, Z. 2018. *Precise Mapping and Spatiotemporal Analysis of Paddy Rice Area in Complex Surface Landscape*. Ph.D. thesis, China University of Geosciences.

Sun, W., B. Chen and D. Messinger. 2014. Nearest-neighbor diffusion-based pansharpening algorithm for spectral images. *Optical Engineering* 53(1):013107. https://doi.org/10.1117/1.OE.53.1.013107.

Wardlow, B. D. and S. L. Egbert. 2008. Large-area crop mapping using time-series Modis 250 m NDVI data: An assessment for the U.S. central great plains. *Remote Sensing of Environment* 112(3):1096–1116. https://doi.org/10.1016/j.rse.2007.07.019.

Wang, F. 1990. Improving remote sensing image analysis through fuzzy information representation. *Photogrammetric Engineering and Remote Sensing* 56(8):1163–1169.

Xiong, Y. K. and Q. L. Zhang. 2019. Cropping structure extraction with NDVI time-series images in the Northern Tianshan economic belt. *Arid Land Geography* (5):1105–1114. https://doi.org/10.12118/j.issn.1000-6060.2019.05.16.

Xiong Q. X. and J. F. Huang. 2009. Estimation of autumn harvest crop planting area based on NDVI sequential characteristics. *Agricultural Engineering* 25(1):5. https://doi.org/CNKI:SUN:NYGU.0.2009-01-034.

Xu, Q., G. Yang, H. Long, C. Wang, X. Li and D. Huang. 2014. Crop information identification based on Modis NDVI time-series data. *Transactions of the Chinese Society of Agricultural Engineering* 30(11):134–144. https://doi.org/10.3969/j.issn.1002-6819.2014.11.017.

Xu Hongwei, Yan Peixin, W. M. X. Z. S. Y. 2020. Automated segmentation of cystic kidney in CT images using residual double attention motivated U-Net. *Computer Application Research* 37(07):2237–2240. https://doi.org/doi:10.19734/j.issn.1001-3695.2019.03.0092.

Yalan, Z., W. Leiguang and L. Xiang. 2018. Comparison of image fusion methods for gaofen-2 panchromatic-multispectral. *Journal of Southwest Forestry University (Natural Sciences)* 38(02):103-110. http://en.cnki.com.cn/Article_en/CJFDTotal-YNLX201802017.htm.

Yang, F., J. Guo, H. Tan, J. Wang, S. O. Geomatics and L. T. 2017. University. Image segmentation based on gray histogram and k-nearest neighbors algorithm. *Science of Surveying and Mapping* 42(3):7–11. https://doi.org/10.16251/j.cnki.1009-2307.2017.03.002.

Yang, P., X. Liao, H. Cheng, M. Shuai and Y. Xie. 2018. A comparative study of remote sensing image fusion methods based on spectral gradient angle and spectral information divergence index. *Engineering of Surveying and Mapping* 27(11):51–55. https://doi.org/10.19349/j.cnki.issn1006-7949.2018.11.010.

Yang, R., L. Su, X. Zhao, H. Wan and J. Sun. 2017. Representative band selection for hyperspectral image classification. *Journal of Visual Communication and Image Representation* 48(Oct.):396–403. https://doi.org/10.1016/j.jvcir.2017.02.002.

Yuan, Y., J. Lin and W. Qi. 2017. Hyperspectral image classification via multitask joint sparse representation and stepwise MRF optimization. *IEEE Transactions on Cybernetics* 46(12):2966–2977. https://doi.org/10.1109/TCYB.2015.2484324.

Yue, X., F. Mengru, P. Jiatian and C. Yong. 2019. Remote sensing image segmentation method based on deep learning model. *Journal of Computer Applications* 39(10):2905. https://doi.org/10.11772/j.issn.1001-9081.2019030529.

Zhang, C., S. Gao, X. Yang, F. Li, M. Yue, Y. Han, H. Zhao, Y. Zhang and K. Fan. 2018. Convolutional neural network-based remote sensing images segmentation method for extracting winter wheat spatial distribution. *Applied Sciences* 8(10):1981. https://doi.org/10.3390/app8101981.

Zhang, J., L. Feng and F. Yao. 2014. Improved maize cultivated area estimation over a large scale combining Modis–EVI time series data and crop phenological information. *ISPRS Journal of Photogrammetry Remote Sensing* 94(Aug.):102–113. https://doi.org/10.1016/j.isprsjprs.2014.04.023.

Zhang, L., L. Zhang and D. Bo. 2016. Deep learning for remote sensing data: A technical tutorial on the state of the art. *IEEE Geoscience Remote Sensing Magazine* 4(2):22–40. https://doi.org/10.1109/MGRS.2016.2540798.

Zhao, W., S. Du and W. J. Emery. 2017. Object-based convolutional neural network for high-resolution imagery classification. *IEEE Journal of Selected Topics in Applied Earth Observations and Remote Sensing* 10:3386–3396. https://doi.org/10.1109/JSTARS.2017.2680324.

Zhu, X. X., D. Tuia, L. Mou, G. S. Xia, L. Zhang, F. Xu and F. Fraun-Dorfer. 2018. Deep learning in remote sensing: A comprehensive review and list of resources. *IEEE Geoscience Remote Sensing Magazine* 5(4):8–36. https://doi.org/10.1109/MGRS.2017.2762307.

Managing Earth Hazards Using the Deep Reinforcement Learning Algorithm for the Industrial Internet of Things Network

Weiwei Liu

Abstract

Wireless networks using resource management with the enormous number of Internet of Things (IoT) users is a critical problem in developing networks for the fifth generation. The primary aim of this research is to optimize the use of IoT network resources. Earth surface features can be identified and their geo-biophysical properties estimated using radiation as the medium of interaction in remote sensing techniques (RST). Deep reinforcement learning (DRL) has significantly improved traditional resource management, which is challenging to model. The Industrial Internet of Things (IIoT) network has to be carried out in real time with excess network resources. Conventional techniques have a significant challenge because of the extensive range and complexity of wireless networks. The DRL method has been used in several areas, including management and allocation of resources, dynamic channel access, mobile downloading, unified edge computing, caching and communication, and fog radio access networks. DRL-IIoT is more successful than the Q-learning technique for a single agent. The design and analysis of the DRL-based approach in stationary base stations to solve the typical assignment of resources issues have been mostly restricted. The DRL is used as a clustering technique to construct the primary model of the system with k-means. This article discusses optical and microwave sensors in RST techniques and applications, examines the areas where there are gaps, and discusses Earth hazards. Furthermore, a comprehensive resource-based strengthening learning system is developed to ensure the best use of resources. Simulation results show that the suggested method efficiently (97.24%) allocates available spectrum, cache, and computer resources to deep deterministic policy gradient benchmarks.

Overview of Resource Management Using Deep Reinforcement Learning

In resource management, deep learning approaches in Internet of Things (IoT) networks are applied in resource management (Amudha 2021). Machine learning– and deep learning–based resource management in wireless IoT environments is currently available between communications and networks (Shakeel *et al.* 2020). The directions in the use of the deployment and management of these resources plays an important role in IoT networks (Pham *et al.* 2020). The blending of the physiological, virtual, and natural realms is referred to as the fourth industrial revolution. Three-dimensional printing, genetic modification, and quantum entanglement are a few of the cutting-edge technologies that have come together to form this powerful new tool for monitoring Earth hazards with remote sensing techniques (RST).

When many devices use a communication path at the same time, a channel can become overloaded (Gao *et al.* 2020a). As IoT devices proliferate, they pose new issues in terms of congestion control, smart device networking and storage architecture, and effective data exchange protocol design (Manogaran *et al.* 2018). IoT device access channel bottlenecks can be alleviated using various access probability and targeting distinct connected devices (Elgendy *et al.* 2021). Resources for cellular distributed systems require resource sharing and access control methods to support larger bandwidths or connections with various network resources (Jan *et al.* 2020). The existing problems resulting from deep reinforcement learning (DRL) significantly improved traditional resource management, which is challenging to model (Gunasekaran and Narayanasamy 2018). It is becoming increasingly difficult for information technology professionals to keep up with the increasing number of devices in use, which necessitates a lot of time-consuming day-to-day tasks to monitor hazards by RST methods. The Industrial Internet of Things (IIoT) network has to be carried out in real time with excess network resources. Using low-cost IoT devices for reliable unsupervised localization is difficult (Shakeel *et al.* 2018). As a result, this study provides an unsupervised wireless-location approach based on DRL (Ranjan *et al.* 2020). DRL-based distributed control planning performed effectively in an observable IIoT scenario (Gao *et al.* 2020b). The major goal of this article is to highlight the methods for enhancing the IIoT using machine learning (Abdel-Basset *et al.* 2019). Deep learning manages resource approaches in IoT networks, which use deep learning. It is currently possible to use machine learning– and deep learning–based resource management in wireless RST environments. In monitoring Earth hazards, these resources can be deployed and managed in various ways.

Mobile networks with wide coverage are becoming increasingly important for the IIoT to achieve the goal of the fourth industrial revolution (Abd EL-Latif *et al.* 2020). In general, the 5G wireless mesh network will serve as a unifying network, connecting billions of IIoT devices to support sophisticated IIoT operations (Awuson-David *et al.* 2021). This research describes a distributed Q-learning supported channel assignment technique for two distinct IIoT networks (Chi *et al.* 2015). The quality of service of femtocell and conventional cellular blockchain-based IoT gear or impartiality is considered when building incentive functions (Bachmann *et al.* 2018). Fixed and dynamic learning rates and various types of multivalent cooperation modes are examined (Ren and Bao 2020). DRL is used as a clustering technique to construct the primary model of the system with k-means (Ding *et al.* 2020). In the sphere of wireless sensor networks, minimizing network delay and increasing network longevity are always major concerns (Yassine *et al.* 2020). Data, information, and physical hardware that can be easily reached from a remote computer via a local area network or corporate intranet are known as shared resources to monitor hazards by RST methods.

In this research, the cell outage situation in ultradense networks (UDN) aims to improve customers' throughput even while maintaining service quality criteria for each mobile user (Zhang *et al.* 2020). The k-means clustering approach assigns compensated users to neighbors and then uses a deep neural network to estimate the implementation

Weiwei Liu is with the School of Computer Science, Wuhan University, Wuhan 430072, People's Republic of China (wwliu2022@126.com).

relationship (Yang *et al.* 2020). It tests the DRL-based framework's efficiency and efficacy in achieving user rate requirements and dealing with cell interrupt compensation (Li *et al.* 2019). DRL-IoT is implemented to produce efficiency and overcome the disadvantages (Dhanachandra *et al.* 2015). Cell outages in UDN are being studied to see if they can increase customer throughput while maintaining service quality standards for individual mobile users to monitor Earth hazards by RST. K-means clustering assigns compensated users to their neighbors and then estimates the implementation relationship using deep neural networks.

The main contributions of this article are the following:

- Resource management is used to generate tasks dynamically, and it is essential to optimize the delay of produced activities over time for monitoring the Earth hazards process by RST.
- A key feature for Q-learning is to evaluate the benefit of various actions without assuming a modeling approach for monitoring Earth hazards.
- To ensure optimum usage, a thorough resource-based reinforcement learning structure is implemented by RST.

The remainder of this article is structured as follows. The next section discusses existing resource management models and allocation using DRL algorithms for IIoT networks to monitor the Earth hazards process by RST. Following this, the DRL-IIoT is implemented. Numerical results are then presented and concluding remarks given.

Analysis of Existing Methods on Reinforcement Learning Method

Due to the different industries and perspectives involved, the reviewed literature has suggested different methods to implement this paradigm Nieto *et al.* (2019) define managing resources for a behavioral-cognitive IoT based on DRL and energy efficiency (DRL-EE). Many people are interested in this since it has many applications, such as pervasive computing, manufacturing, and health care. The previous issue is turned into a Markov decision process, reducing the long-term average latency of the activities. Using social networking properties, perceptual and emotional IoT can enhance system performance.

Wang *et al.* (2019) stated that an alternative approach to unsupervised wireless localization (UWL) is deep reinforcement learning (DRL-UWL). Proximity is crucial when specializing in IoT data collection and analysis. Unsupervised localization using low-cost IoT devices, on the other hand, is a challenge (i.e., localization without training data with known location labels). Industries such as manufacturing and transportation have benefited greatly from IoT applications, and the IIoT is described as the convergence of advanced manufacturing systems with IoT.

Yao *et al.* (2019) defined sensors and platforms for UAVs, which are now used in nearly every industry that relies on data collected from top or oblique views. Remote sensing statistical data analysis methods are tailored mostly to specific applications, even though they are general remote sensing tools. UAV-based remote sensing in farmland, ecologic, urban, and risk assessment applications can be summarized using these solutions. By describing their useful possibilities, researchers share their suggestions for future research and draw definitive conclusions.

Yang *et al.* (2019) proposed a relationship between energy-efficient IIoT (EE-IIoT),and decentralized Q-learning assisted network communication. Achieving a wide-coverage cellular network has become more crucial for the IIoT. To enable advanced IIoT businesses, the 5G network is planned to be a cohesive link that enables billions of devices. A heterogeneous network design is a good way to achieve broad, seamless information coverage. IoT application scenarios are expanding as smart mobile devices become more common, and 5G networks typically emerge rapidly.

Lei *et al.* (2020) noted that UDN has been among the significant technologies allowing 5G communications to meet elevated, high-density wireless endpoint access criteria. UDN has many diverse cells compared to telecommunication (long-term evolution). Network performance will be considerably affected if a problem and its effects are not mitigated in time. Therefore, cell outage compensation (COC) based on UDN (COC-UDN) is suggested. IIoT's core communication characteristics are similar to those of IoT in general: low cost, constrained equipment, and network extensibility.

Lai *et al.* (2020) aimed to lower the average long-term delay through evaluating the dynamic resource management issues of combined power regulation and computing the distribution of resources in IIoT. The original problem is turned into part of the tasks, and a part of the original problem is now a task. DRL for task generation (TG) is provided through considering dynamics and continuity (DRLTG). Using IIoT and clustering techniques, the problem as expressed was solved. Information is collected from sensing devices in an industrial setting, and the devices are accessible and controlled via the Internet.

From the above research strategies, the existing methodologies of DRL-EE, DRL-UWL, EE-IIoT, COC-UDN, and DRLTG learning are compared with a novel method of DRL-IIoT to improve the accuracy of acute teaching through the mobile intelligent terminal for developing physical skills for monitoring the Earth hazards process by RST. The following section discusses the proposed model briefly.

Implementation of the DRL-Based IIoT

The growth of deep learning and deep neural networks aided in speeding up the process. DRL advancement can be used to solve various problems, including natural disasters. The reinforcement learning technique, which uses continuous trial and error to find the best control strategy, has advanced quickly in recent years.

Resource Management

The deep learning and decision-making abilities of high-dimensional data in native-form DRL are, as a result, an approach to the IIoT. This is known for its computer-integrated manufacturing, with machine learning integration into edge-intelligent IIoT a major enabler for intelligent IoT. Machine learning methodologies described in this research strengthen the intellectual function of edge-enhanced IIoT to achieve unique, sophisticated applications. DRL-IIoT is more effective for a single agent than Q-learning to monitor hazards by RST methods. The design and analysis of the DRL-based approach in stationary base stations are constrained largely to solving typical resource allocation issues. K-means are used to build the primary model of the system using the DRL.

Figure 1 represents resource management as to how firms correctly manage their many capabilities. There must be careful planning to ensure that the right resources are allocated to the right job with conventional techniques. Individuals, organizations, technology, networks, and consumables have deadlines and must be managed in a timely fashion. This resource management can be a combination of radio and computational management techniques. Both management techniques are connected with more outputs, such as power control, optimization, and so on. It can produce a real-time excess network with less performance. In this resource management, efficiency increased through the DRL method in the IIoT. A good resource management system should include resource and demand management and prioritizing high-value work to maximize available resources. Ensuring proper utilization of available resources is essential to achieve the strategic objectives for monitoring Earth hazards with RST.

DRL-IIoT solves the typical significant resource management challenges, such as radio management, computational management, and management of other networks. Traditional resource management, which is difficult to model, is considerably enhanced by applying DRL to tackle current difficulties. The IIoT network must operate in real time with surplus network resources. DRL clustering techniques blend deep learning's sensing function with reinforcement learning's decision-making load. It is a type of artificial intelligence considered true artificial Intelligence since it is closer to human thinking. Deep learning is becoming more popular for targeted observation of the environment and offers information about the present state of the environment. The present state is then mapped to the desired state via reinforcement learning, corresponding action is taken, and values are assessed. A process of constant interaction creates a step-by-step method for decision making. More than 1 billion devices are connected to the

IoT to monitor hazards by RST methods in big data. Machine learning is energized by data and creates insight from those data. In machine learning, past behavior identifies patterns and creates models that help make predictions and events.

Architecture of DRL

DRL is used to maximize a satisfaction criterion. Meanwhile, interacting with a given environment through trial and error yields a long-term aggregate of rewards. To reinforce the learning system to implement
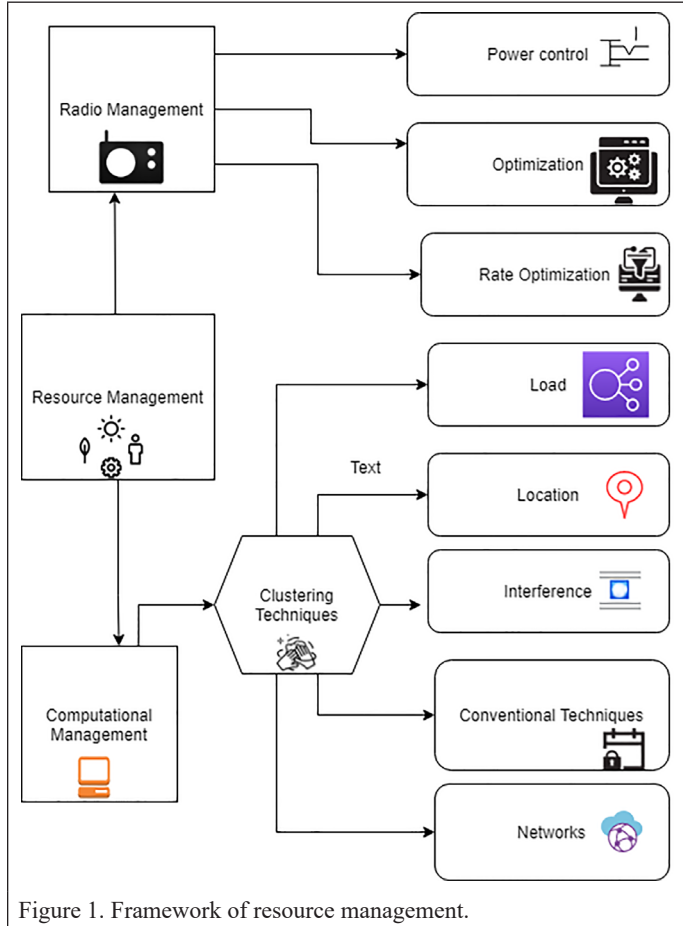
Figure 1. Framework of resource management.
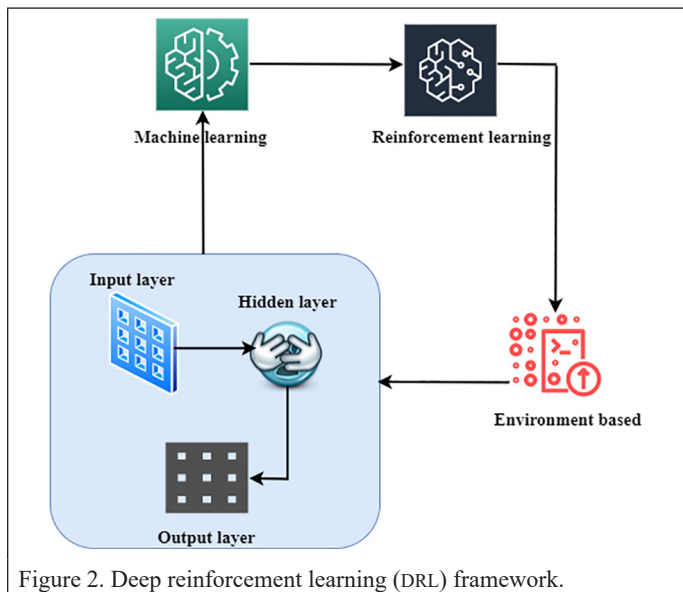
Figure 2. Deep reinforcement learning (DRL) framework.

these features, decision makers known as agents are at the heart of the framework.

Figure 2 is used to calculate the working state-of-the-art setting; the representative is a consequence of the current situation, capable of doing particular acts. Maximizing a satisfaction criterion is accomplished through the application of DRL. The rewards accrue over time due to interacting with a given environment through trial and error. The framework's most important component is the agent, a decision maker, who plays a key role in implementing these features to monitor Earth hazards by RST. The mathematical foundations and concepts of reinforcement learning are introduced as follows:

$$A*(S) = \max_\pi A^\pi \tag{1}$$

$$B*(S,\, b) = max_\pi B^\pi \tag{2}$$

$$R(S_{t+1(s0,\, a0,\, \ldots,\, st,\, at)} R(S_{t+1}/ s_{t,\, a0}) \tag{3}$$

The Markov decision process is used as the key formalism of reinforcement learning and resource allocation. It defines the state that determines the process's future; the current situation and the agent are not necessary. It can be summarized in Equations 1 to 3, where A and B represent best and action-value functions, respectively; (S) denotes a value function; t determines a time function; and a denotes optimal value functions $(s0, a0, \ldots, st, at)$. The agent obtains a reward after choosing an action at time max_π; $= st+1$ $rt + 1$ is a scalar reward and enters a new stage S_{t+1}, which depends on the current condition and the action selected, as shown in Figure 1. When it comes to reinforcement learning, to monitor Earth hazards by RST, the Markov decision process is a key formalism, as the current state solely defines the process's future and current situations. The agent is completely uninterested in the history of the process.

At each epoch, the agent performs an action that alters its environment's state and gives a reward. The procedure then continues. The optimal reward value and value functions are suggested. At each epoch, the agent performs an action that alters its environment's state and gives a reward π. Value functions and the best policy are used to further process the suggested reward value.

DRL in IIoT

The transition from reinforcement learning to DRL is a long, winding road. The state and action spaces in traditional tabular reinforcement learning, such as Q-learning, are small enough approximate values. Arrays or tables can represent functions, and the exact optimal value functions are commonly found using approaches in this situation. On the other hand, the most effective methods when it comes to design have a difficult time being implemented in the real world.

According to the proposed DRL-based optimization strategies in RST convergence results to monitor Earth hazards, transactional throughput begins the learning process with relatively low throughput. However, as the number of people grows, the bandwidth ultimately reaches its maximum capacity. A parameterized representation of approximate value functions uses DRL functional form with a weight vector instead of a table to address this issue. is used DRL functional form with a weight vector instead of a table to address this issue. Because of its ability to learn different levels of abstraction from data, DRL can execute hard tasks with less prior knowledge. The use of networks is represented in Figure 3. Further information on DRL can be discussed.

The convergence performance of the proposed DRL-based performance optimization strategy is shown in Figure 3; transactional throughput is relatively poor at the start of the learning procedure. However, as the number of people increases, throughput also grows eventually so does the throughput, which eventually reaches. Afterward, the system has reached a steady state, indicating that the system is working properly. Furthermore, it has been discovered that the proposed project can acquire more funding than the other three DRL-based baselines in terms of throughput. This demonstrates the benefit of the proposed approach.
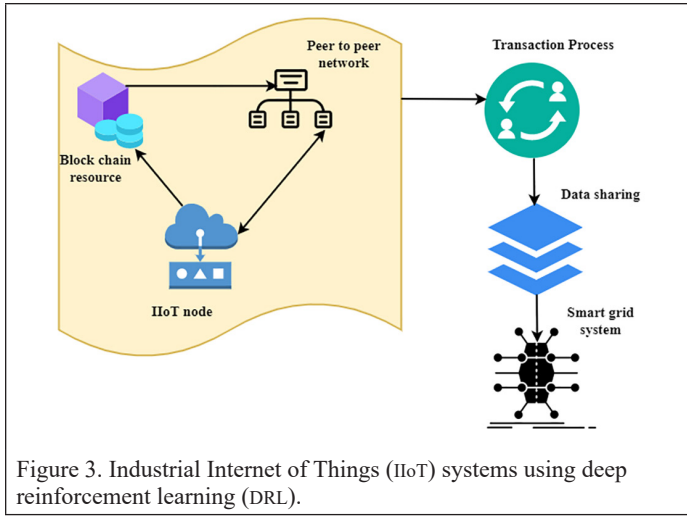
Figure 3. Industrial Internet of Things (IIoT) systems using deep reinforcement learning (DRL).

DRL methodologies were applied to IIoT networks in various fields, including smart grids, manufacturing, smart procedures, and environmental monitoring. These data can be stored, processed, and shared with the IIoT node over a peer-to-peer (P2P) network. The proposed clustering approaches (k-means clustering techniques) are implemented to address the considerable problems of the existing techniques in real-time access networks.

Spaces That Are Three-Dimensional and Continuous

Even though several real-world problems result in high-dimensional, continuous-state spaces or action spaces, it is nevertheless impossible to solve them by putting them into a table or performing a function. The phenomenon is referred to as dimensionality's curse. The challenges of Q-learning over IIoT networks to monitor Earth hazards by RST include (1) the test effectiveness problem, (2) learning stability, (3) disastrous interference, (4) discovery problems, and (5) systematic review and depiction learning for generalization.

Issue of Explorations Versus Exploitation

When an agent begins collecting knowledge about the environment, one must choose between learning more about the environment and learning less about it, pursuing the most promising exploration is the environment plan based on the knowledge gained factor(exploration) or the environment plan based on the knowledge gained (exploitation). Reinforcement learning is a field of machine learning to maximize the concept of cumulative reward. In a table reinforcement learning, transition and uncertainty about the reward function. Confidence intervals or percentages can be used to quantify probability parameters of the environment's posterior Different options are available in DRL are put into practice.

Convergence and Stability

Tables and linearly parameterized approximates can be utilized to ensure convergence in reinforcement learning. A huge number of basic functions and the choice of those functions must be defined in such a way that they encompass the entire state-action space. As a result, in high-dimensional issues, this is unworkable. To solve this issue, nonlinear approximates such as convergence and stability has been demonstrated. The k-means algorithm's applications in Q-learning in the monitoring process by RST can be given as clustering and is used in marketing and customer categorization, physiological data and diagnostic imaging, search result grouping, learning algorithms, pattern matching, network analysis, image analysis, and so on.

This can be seen and evaluated in the following equations. In this research, assuming that the block chain system has n IIoT nodes and k block producers, the stake is

$$S = \{z1, z2, \ldots zn\} \qquad (4)$$

$$Y = \{y1, y2, \ldots yn\} \qquad (5)$$

$$C = \{c1, c2, \ldots cn\} \qquad (6)$$

From Equations 4 to 6, the proposed clustering approaches (k-means) are implemented to address the considerable problems of the existing techniques in real-time access networks. Here, zn denotes computational resources cn, where the value of $n = 1, \ldots, n$; yn is defined as the stakes set, and cn represents computing complexity resources. DRL methodologies were applied to IIoT networks in various fields, including smart grids, manufacturing, smart procedures, and environmental monitoring. These data can be stored $z1, z2, \ldots zn$, processed $y1, y2, \ldots yn$, and shared $c1, c2, \ldots cn$ with the IIoT node over a P2P network. In the analysis of algorithms, computational complexity is critical. The ability to select effective methodologies becomes increasingly important, as difficulties are becoming more complex and larger in the monitoring of Earth hazards by RST. It is extremely convenient to categorize algorithms according to how difficult they are to enforce.

The convergence performance of the proposed DRL-based performance optimization strategy is shown in Figure 3; transactional throughput is relatively poor at the start of the learning procedure. However, when the number of people increases, so the throughput increases eventually does the throughput, which eventually reaches. Afterward, the system has reached a steady state, indicating that the system is working properly. Furthermore, it has been discovered that the proposed project can acquire more funding than the other three DRL-based baselines in terms of throughput. The IIoT node can access these data via a P2P network and process those data. To address the current problems in real-time access networks, the proposed clustering approaches (k-means clustering methods) have been implemented to monitor Earth hazards by RST.

Clustering Technique and k-Means Clustering Technique

Clustering algorithms are iterative algorithms that minimize an objective function. For correctly identifying image pixels, such techniques consider pixel intensity levels. Clustering techniques are used for DRL, and the literature improves segmentation. Using the k-means clustering method, many structures are distributed into disjoint and overlapping clusters.

To try to segment images of k-means clustering for typical signs, clusters with homogeneous hybrid combinations are detected. A combination of k-means techniques utilizes fuzzy k-means to segments each cluster into an action as represented in Figure 4. A combination of k-means techniques proposed utilizing fuzzy k-means to segments clustering put it into action are represented in Figure 4. As a mining analysis technique, k-means clustering expression data and even clustering methods are more efficient. Trial-and-error problem solving involves making multiple attempts at solutions. It is a fundamental instruction process that nearly all organisms use to monitor hazards by RST methods. Trying a method, seeing if it performs, and then testing a new method if it does not is called trial and error.

Figure 4. Deep reinforcement learning–based Industrial Internet of Things (DRL-IIoT) with clustering techniques.
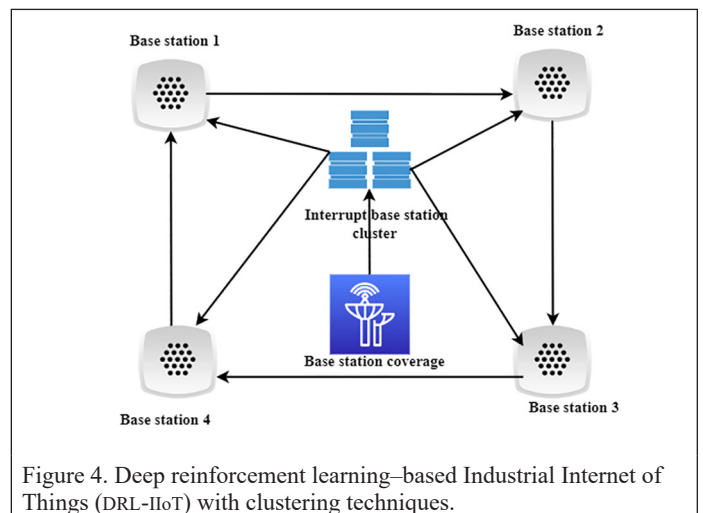
Interrupting the Base Station
Unsupervised machine learning is used in the k-means clustering algorithm. The samples are separated without prototypes instead of relying on the properties of the samples themselves. There are parallels in the data to begin. Setting up the clusters nearby base stations is used to calculate centroids. Coverage of base stations will then recalculate the center of the cluster point involving the iteration process. This process is repeated until the cluster centroids remain unchanged. In the same cluster, reimbursement users are assigned to the base closest to its station, and the connectivity among base stations and users is set:

$$Ri = a \sum \frac{bj}{\pi ij} + b \sum_{m,n\mu B} u \qquad (7)$$

$$Ri(x,y) = \frac{1}{2\pi} \int_{-\infty}^{\infty} e(-\partial |nsB|) e^{\frac{-(a+b)}{bj-m(a,b)|^3}} \qquad (8)$$

The DRL-based framework's attitudes, behaviors, and consequences are defined in Equations 7 and 8. The πij relationship between state spaces i and j for the base station allocated power of transmission πij from base stations to compensation user $n\varepsilon$. The parameters tend to be optimal B for both a and b. Equation 8 shows the $Ri(x,y)$, where Ri is the parameter of state and record on the x and y axes in any orientation, a is the external source for quantization and explicit visual instruction, ∂ is the total evaluation criteria, S is the difference of an image to identify, u is the velocity for the lower state, v is the velocity of the higher state, and

Based on Equations 7 and 8, the parameters tend to be optimal with the external source for quantization, explicit visual instructions and the total evaluation criteria of an image is to identify the velocity of lower state and the velocity of higher state based on the object to monitor Earth hazards by RST. Based on Equations 7 and 8, the parameters tend to be optimal for the parameter of state and record in any orientation the external source for quantization, explicit visual instructions, and the total evaluation criteria for the difference of an image to identify the velocity for the lower state and the velocity of the higher state the aspect enclosing with the object to monitor Earth hazards by RST.

K-means clustering is a vector quantization method originally derived from signal processing that aims to divide n observations into k clusters where each observation belongs to the cluster with the nearest mean from Equation 8, serving as a cluster prototype in monitoring the Earth hazards process by RST. The incentive must reflect that goal if the framework is to enhance base station communication and fulfill each compensation user. The work reduce the action space to a manageable size Then define the instantaneous reward as the proposed work reduce the action space to a manageable size. The computational complexity is minimal, and the size is tiny.

Resource-Based Strengthening Learning System
For illustration, a DRL representative will monitor the web-based learning process, utilize the neural networks to calculate the approximated Q value in each epoch, and then choose an action that determines an aggressive cop action with probability at random and select the action with probability $1 - e$, the maximum calculated Q value. During the immediate reward r and the engagement with the environment, the following states are observed, and the state transition within the construction phase necessitates the accumulation of a sufficient number of samples of value estimates and their corresponding (s, a) to take advantage of experience memory to make the training phase go more smoothly. Given the speed of the pathways the data take and the increase in the number of packets being sent in comparison, for direct connections, latency tends to decrease as bandwidth increases in the monitoring process by RST:

$$d = \frac{1}{e} \sum_{i=1}^{n} a(i) + b(i) + c(i) \qquad (9)$$

Each source must constantly adjust its network congestion as a feature of the feedback information it receives from the network's inability to remain near the curves in monitoring the Earth hazards process by RST. Consequently, congestion control is an inherently distributed optimization problem. The boundary of the proposed DRL-IIoT denoted as   and expressed in Equation 9; $a(i)$, $b(i)$, and $c(i)$ indicate the estimated time for particular number i indicate the estimated time is the number i, elevation e, and diameter d of the simulating objects, respectively. There are $6n$ objects in the experiment, and few considerations can be exhibited.

which is the many considerations exhibited. When the output sign of classification is confusing, the decision boundary is the area of the problem space where this is the case. The classification problem is linear if the decision surface is a horizontal angle, and the classes are differentiable for monitoring the Earth hazards process by RST. It is not always easy to tell where one decision stops and another begins. A pictorial representation of μ is shown in Figure 5; $p(i)$, $q(i)$, and $r(i)$ indicate the length, breadth, and diameter of the simulator objects, respectively. The number of items in the simulation is n. The boundary for the proposed model DRL-IIoT is established.

Using clustering algorithms, the DRL is a procedure in which the implementer can lower the response rate by reinforcing either fewer or longer intervals between response incidents in monitoring the Earth hazards process by RST. To achieve this, relatively narrow action space and low computing overhead have been proposed in Figure 6. The DRL representative uses neural networks to observe the current state to calculate the estimated Q value in each epoch and then chooses an action that implies an aggressive cop action with probability at random accessing and selects the action with probability $1 - e$; the maximum calculated Q value is updated during the retrieving reward e and engagement with the environment. Overlapping methods of k-means clustering are used to distribute many structures into overlapping and disjoint clusters. Occurring clustering methods, as previously mentioned, allow data points to be part of multiple clusters in monitoring the Earth hazards process by RST. Partitioning methods are more popular than overlapping clustering algorithms because they are simple and effective on large data sets. The following states are observed and the sample network parameters are updated for retrieving rewards in the process of random choosing from the remembrance of an experience with different incentives. The following states are observed, and the state transition in memory and sample network parameters to update network parameters for retrieving rewards in the process of random choosing from the remembrance of an experience because the incentives are different. The network changes depending on the actions chosen.

Q-Learning Technique with DRL
This reinforcement learning technique uses Q-learning, a model-free technique, to consider the importance of activity in a certain state. "Model free" means it does not require a system model and can deal with unpredictable transitioning and incentives without the need for adjustment or modification.
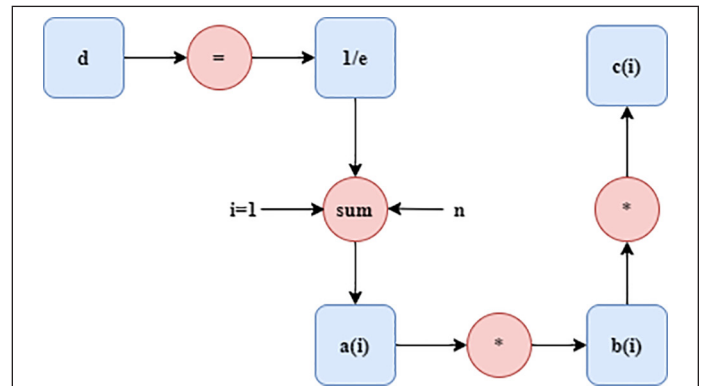
Figure 5. Pictorial representation of remote sensing techniques (RST).
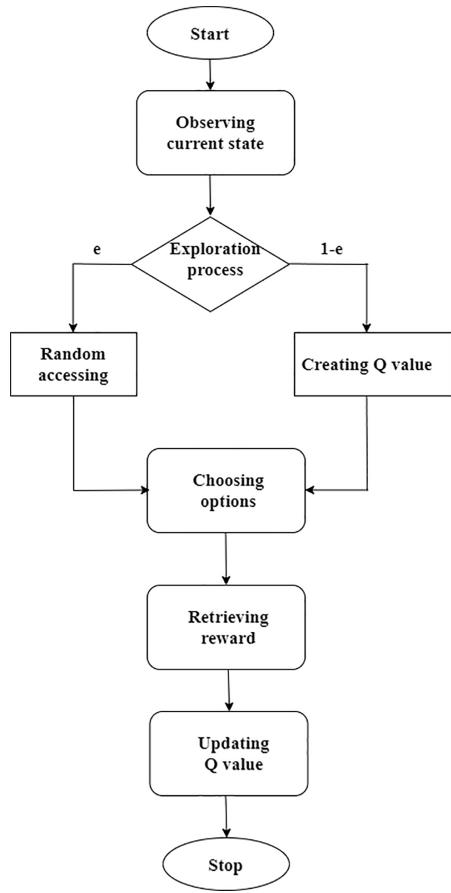
Figure 6. Process related with a resource-based strengthening learning system.
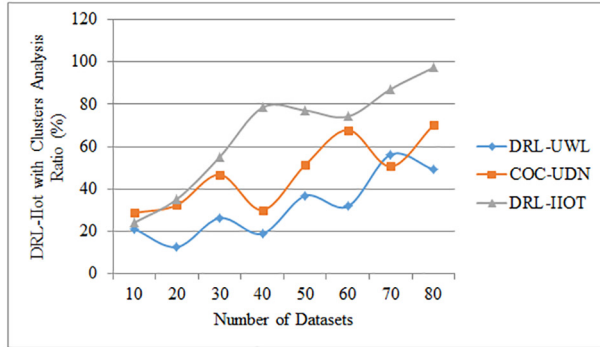
Figure 7. Framework of the deep reinforcement learning–based Industrial Internet of Things (DRL-IIoT) with clusters.

Algorithm 1
Input:
ts: Type of state [n]
bd: queue.size [..]
Output:
Given_
bd: in state condition
if *bd* == 20 []then
if *tp* == add rows then
Given_*bd* = 1000
else if *tp* == state info then add columns-1
Given_*bd* = 100
end if
return Given_*bd*

Algorithm 1 shows how documents are transferred to the server in sequential order. Even though there is no priority scheme for subsequent frames, the latency of an image frame is measured in this approach. Due to its lower level of unpredictability than Q-learning, the DRL model approach outperforms the conventional algorithm. The object/image file type has a few things to consider. The bandwidth component is based on 20 bits if a condition is true.

To consider the significance of activity in a specific state, this reinforcement learning technique uses Q-learning to assess the image frame's delay in RST, even though there is no priority mechanism for subsequent frames to monitor Earth hazards:

$$A*(S)(S_{t+1(s0, a0, ..., st, at)R(S_{t+1}/s_{t, at})}) \qquad (10)$$

$$S = a(i) + b(i) + c(i) * a \sum \frac{bj}{\pi ij} \qquad (11)$$

In each epoch, an RST representative will monitor the web-based learning process, which uses neural networks to calculate the approximated Q value and then selects an action that determines an aggressive cop action at random and selects the action with probability $1 - e$, the maximum calculated Q value using Equations 10 and 11.

The file type is specified as an image with a size of 1000 bytes for the state information, and then columns-1 are added. In other words, a state is nothing more than the pixels on top of which a definition is placed. Objects must be loaded within a bandwidth of 100, including their content, location, and proper knowledge. Objects with lower quality will have their information added to the bandwidth Bdsection of the image and object. As a result, if the condition is completed within this and the residing part executes the state information, columns-2 are added to the condition. Even if there is a lot of traffic, uploading a large object takes longer. The algorithm returns the bandwidth allocated in the system at this point.

From the above recommendations of reinforcement learning, IoT wireless management information has been researched through frequency assignment and power administration for monitoring the Earth hazards process by RST. Other approaches to enhance quality of service and communication performance are compared with DRL-IIoT, improving reinforcement learning performance.

Results and Discussion
As research continues, DRL is rapidly being used in various power systems, such as cybersecurity, economic dispatch, and system optimization, when the DRL approach is suited to solve complex events, dynamic behaviors, and uncertain constraints.

Analysis of DRL-IIoT with Cluster
The simulation scenario in this research is rather straightforward. More sophisticated network situations, such as heterogeneity with multiple nodes, are given in Figure 7 and will be studied in the future as small cells will be taken into account. The swap notes, among others, propose a DRL-based COC method: COC-UDN and DRL-EE with DRL-IIoT. In the future, channel allocation will be done. In each epoch, a DRL representative observes the current state and uses neural networks to estimate the Q value, selects an action that implies aggressive cop action with random access, and selects the action with probability for monitoring the Earth hazards process by RST; Q is updated during retrieving reward e and interaction with the environment. A huge amount of attention has been paid to the task of transferring concerns in DRL. A few researchers have analyzed how to correctly allocate the computational resources of the DRL server to improve the system's consequences that may result in and reduce job delay.

Performance Ratio
Next, an IIoT dynamic resource administration DRL algorithm based on dynamic resource mapping is proposed. Because the system is asynchronous, inputs taken during the algorithm involving training are self-executed through the representatives in Figure 8. The performance analysis is compared with DRL-UWL and DRL-IIOT, and the proposed

system's performance is higher than other conventional techniques. Q-learning's ability to evaluate the utility function of various actions without requesting a map of the environment is one of its strongest suits. Reinforcement learning teaches an agent how to solve a problem without a teacher's aid for monitoring the Earth hazards process by RST.

Comparison of DRL-IIoT with Conventional Techniques
From Table 1, the comparison of DRL-IIoT with the traditional techniques is compared, and the results achieved are higher. It is a machine learning task known as cluster analysis or clustering, and it is a method for automatically identifying patterns in data for monitoring the Earth hazards process by RST. On the other hand, unsupervised learning algorithms focus on finding groups or clusters of data based on their interpretation of input data. As a result of the three approaches described above, one can determine the average task delay based on the number of IIoTs, the computing quantity of the assignment, data volume, and the DRL server's processing capability.

From Figure 9, both industry and science are very interested in the IIoT because it can enhance production performance and resource intelligence. As a result of the rapid expansion of end devices and information flows, DRL-IIoT is experiencing a shortage of spectrum for broadband devices.

Efficiency Analysis
From Table 2, the analysis of DRL-IIoT is that synchronization between IIoT devices and peripheral networks is necessary to provide graphics rendering deep neural network inference services that require high speed and low reliability in their inference results. To reduce service delays, sample rate adaptation, which dynamically configures the sampling rates of IIoT devices based on network conditions, is essential.

A single number in a vector represents the mean of each variable for the findings in a cluster, called a centroid in data for monitoring the Earth hazards process by RST. Put another way, the centroid is the cluster's multi-dimensional average. For information technology professionals, keeping up with the increasing number of devices in use is becoming increasingly difficult, requiring a lot of time-consuming daily tasks to monitor hazards by RST methods.

DRL-IIoT and the suggested algorithm have a more modest performance gap than the computer-generated random method or the packed k-means clustering technique with optimal probability for monitoring the Earth hazards process by RST. The Q-learning algorithm in this study is based on state information, reward function, and action vector design and not on the algorithm provided in IoT.

Conclusion
The Q-learning problem is solved in this study using a DRL-based framework to maximize connection while meeting the need of each compensation user and is well suited for huge IoT environments for monitoring the Earth hazards process by RST. A well-trained network can solve the Q-learning issues in which the result is close to public. A well-trained network can Q-learning issues are rapidly resolved, and the result is closed to the public. The best price framework is capable of dealing with clustering techniques. The simulation scenario in this research is rather straightforward. More complex work will be done in

Figure 8. Deep reinforcement learning (DRL) performance analysis.
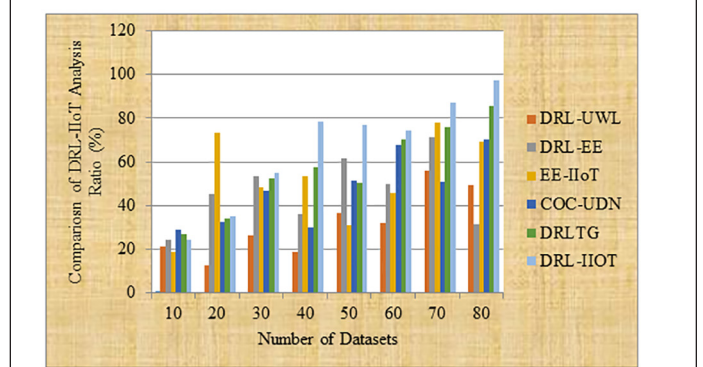
Figure 9. Comparison of the deep reinforcement learning–based Internet of Things (DRL-IIT) analysis.
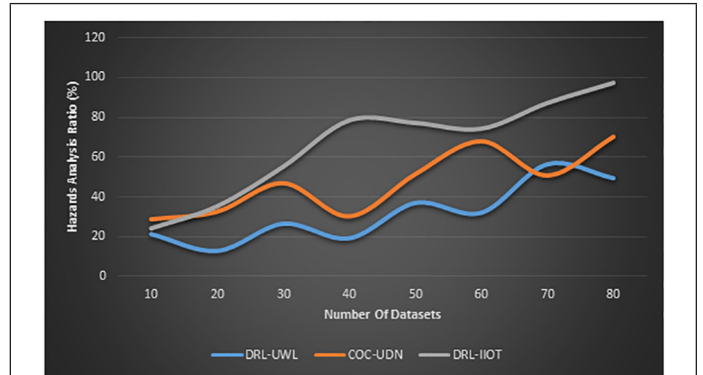
Figure 10. Comparison of remote sensing techniques (RST) analysis.

Table 1. Comparison of the deep reinforcement learning–based Industrial Internet of Things (DRL-IIoT) with conventional techniques.

Number of Data Sets	DRL-UWL	DRL-EE	EE-IIoT	COC-UDN	DRLTG	DRL-IIoT
10	21.21	24.54	18.76	28.76	27.13	24.10
20	12.65	45.36	73.56	32.45	34.25	35.23
30	26.33	53.66	48.23	46.76	52.39	55.13
40	18.98	35.97	53.26	30.12	57.54	78.43
50	36.78	61.78	31.03	51.34	50.43	77.11
60	31.87	49.74	45.69	67.87	70.17	74.20
70	56.21	71.23	77.89	50.65	75.89	87.15
80	49.21	31.43	69.31	70.12	85.74	97.24

Table 2. Analysis of the efficiency of the Q-learning method.

Number of Devices	DRL-EE	Q-Learning	IIoT	Clustering	k-Means Clustering
10	52.1	43.1	62.5	35.3	72.9
20	58.3	44.4	61.6	36.6	75.6
30	59.7	47.3	59.1	37.8	77.3
40	57.8	48.6	58.3	38.6	79.6
50	58.5	42.9	61.4	42.5	81.5
60	59.4	41.2	64.6	46.4	83.2
70	64.3	48.4	65.8	41.8	86.7
80	66.6	51.1	66.5	47.3	93.2

the future, such as heterogeneous networks and networks with several nodes. Among others, a DRL-based clustering m-means technique method will be proposed and considered. In the future, channel allocation will be done. Simulation findings demonstrated that the suggested DRL-IIoT algorithm outperformed Q-learning with the best accessibility frequency and the spontaneous allocated approach. The DRL's performance will continue to improve in Earth hazards management. Dimensions such as length, breadth, and diameter are all considered in the formulations presented here to make up the simulation by RST approaches. Using a mathematical tool the proposed method achieves the highest convergence speed, improved learning efficiency of 97.24% when compared with Convolutional Neural Network.

Using a mathematical tool as an extra benefit has a faster convergence speed, improved learning efficiency of 97.24%, and somewhat higher performance than convolutional neural networks. Future improvements to the DRL's performance will be based on power management.

References

Abd EL-Latif, A. A., B. Abd-El-Atty and S. E. Venegas-Andraca. 2020. Controlled alternate quantum walk-based pseudo-random number generator and its application to quantum color image encryption. *Physica A: Statistical Mechanics and Its Applications* 547:123869. https://doi.org/10.1016/j.physa.2019.123869.

Abdel-Basset, M., G. Manogaran, M. Mohamed and E. Rushdy. 2019. Internet of things in smart education environment: Supportive framework in the decision-making process. *Concurrency and Computation: Practice and Experience* 31(10):e4515. https://doi.org/10.1002/cpe.4515 .

Amudha, G. 2021. Dilated transaction access and retrieval: Improving the information retrieval of blockchain-assimilated Internet of Things transactions. *Wireless Personal Communications*. https://doi.org/10.1007/s11277-021-08094-y.

Awuson-David, K., T. Al-Hadhrami, M. Alazab, N. Shah and A. Shalaginov. 2021. BCFL logging: An approach to acquire and preserve admissible digital forensics evidence in the cloud ecosystem. *Future Generation Computer Systems* 122:1–13. https://doi.org/10.1016/j.future.2021.03.001.

Bachmann, D., F. Weichert and G. Rinkenauer. 2018. Review of three-dimensional human-computer interaction with a focus on the leap motion controller. *Sensors* 18(7):2194. https://doi.org/10.3390/s18072194.

Chi, X. C., Y. S. Yang, Y. H. Wang, J. C. Gao, N. Sui, H. G. Yang, L. Zou, Z.-H. Kang and H. Z. Zhang, 2015. Studying of photoluminescence characteristics of CdTe/ZnS QDs manipulated by TiO2 inverse opal photonic crystals. *Optical Materials* 46:350–354. https://doi.org/10.1016/j.optmat.2015.04.043.

Dhanachandra, N., K. Manglem and Y. J. Chanu. 2015. Image segmentation using K-means clustering and subtractive clustering algorithms. *Proceedings of Computer Science* 54:764–771. doi: 10.1007/978-981-15-9712-1_8.

Ding, Y., Y. Li and L. Cheng. 2020. Application of Internet of Things and virtual reality technology in college physical education. *IEEE Access* 8:96065–96074. doi: 10.1109/ACCESS.2020.2992283.

Elgendy, I. A., W. Z. Zhang, H. He, B. B. Gupta and A. A. Abd EL-Latif. 2021. Joint computation offloading and the task is caching for multi-user and multi-task MEC systems: Reinforcement learning-based algorithms. *Wireless Networks* 27(3):2023–2038. https://doi.org/10.1007/s11276-021-02554-w.

Gao, J., H. Wang and H. Shen. 2020a. Smartly handling renewable energy instability in supporting a cloud datacenter. Pages 769–778 in 2020 IEEE International Parallel and Distributed Processing Symposium (IPDPS), held in New Orleans, LA, USA , 18-22 May 2020. New York: IEEE. doi: 10.1109/IPDPS47924.2020.00084.

Gao, J., H. Wang and H. Shen. 2020b. Task failure prediction in cloud data centers using deep learning. *IEEE Transactions on Services Computing*. doi: 10.1109/TSC.2020.2993728.

Gunasekaran, A. and P. Narayanasamy. 2018. Analyzing the network performance of various replica detection algorithms in wireless sensor network. *Journal of Computational and Theoretical Nanoscience* 15(3):989–994. https://doi.org/10.1166/jctn.2018.7188, https://doi.org/10.1002/cpe.4515.

Jan, M. A., J. Cai, X. C. Gao, F. Khan, S. Mastorakis, M. Usman, M. Alazab and P. Watters. 2020. Security and blockchain convergence with the Internet of Multimedia Things: Current trends, research challenges, and future directions. *Journal of Network and Computer Applications*. https://doi.org/10.1016/j.jnca.2020.102918.

Lai, X., Q. Hu, W. Wang, L. Fei and Y. Huang. 2020. Adaptive resource allocation method based on deep Q network for Industrial Internet of Things. *IEEE Access* 8:27 426–27 434. doi: 10.1109/ACCESS.2020.2971228s.

Lei, L., Y. Tan, K. Zheng, S. Liu, K. Zhang and X. Shen. 2020. Deep reinforcement learning for autonomous internet of things: Model, applications and challenges. *IEEE Communications Surveys and Tutorials* 22(3):1722–1760. doi: 10.1109/COMST.2020.2988367.

Li, Y., X. Hu, Y. Zhuang, Z. Gao, P. Zhang and N. El-Sheimy. 2019. Deep reinforcement learning (DRL): Another perspective for unsupervised wireless localization. *IEEE Internet of Things Journal* 7(7):6279–6287. doi: 10.1109/JIOT.2019.2957778.

Manogaran, G., R. Varatharajan, D. Lopez, P. M. Kumar, R. Sundarasekar and C. Thota. 2018. A new IoT and big data ecosystem architecture for securing smart healthcare monitoring and alerting systems. *Future Generation Computer Systems* 82:375–387. doi: 10.1007/978-3-030-37468-6_25.

Nieto, Y., V. Gacía-Díaz, C. Montenegro, C. C. González and R. G. Crespo. 2019. Usage of machine learning for strategic decision making at higher educational institutions. *IEEE Access* 7:75007–75017. doi: 10.1109/ACCESS.2019.2919343.

Pham, D. V., G. L. Nguyen, T. N. Nguyen, C. V. Pham and A. V. Nguyen. 2020. Multi-topic misinformation blocking with a budget constraint on online social networks. *IEEE Access* 8:78879–78889. doi: 10.1109/ACCESS.2020.2989140.

Ranjan, G., T. N. Nguyen, H. Mekky and Z. L. Zhang. 2020. On virtual id assignment in networks for high resilience routing: A theoretical framework. Pages 1–6 in GLOBECOM 2020 IEEE Global Communications Conference, held in 07-11 December 2020, Taipei, Taiwan: IEEE. doi: 10.1109/GLOBECOM42002.2020.9322538.

Ren, F. and Y. Bao. 2020. A review of human-computer interaction and intelligent robots. *International Journal of Information Technology and Decision Making* 19(01):5–47. doi: 10.1007/978-3-030-70099-7_12.

Shakeel, P. M., S. Baskar, V. S. Dhulipala, S. Mishra and M. M. Jaber. 2018. Maintaining security and privacy in health care system using learning-based deep-Q-networks. *Journal of Medical Systems* 42(10):186. https://doi.org/10.1007/s10916-018-1045-z.

Shakeel, P. M., S. Baskar, H. Fouad, G. Manogaran, V. Saravanan and Q. Xin. 2020. Creating collision-free communication in IoT with 6G using multiple machine access learning collision avoidance protocol. *Mobile Networks and Applications*. https://doi.org/10.1007/s11036-020-01670-9.

Wang, J., C. Jiang, K. Zhang, X. Hou, Y. Ren and Y. Qian. 2019. Distributed Q-learning aided heterogeneous network association for energy-efficient IIoT. *IEEE Transactions on Industrial Informatics* 16(4):2756–2764. doi: 10.1109/TII.2019.2954334.

Yang, H., W.-D. Zhong, C. Chen, A. Alphones and X. Xie. 2020. Deep-reinforcement-learning-based energy-efficient resource management for social and cognitive Internet of Things. *IEEE Internet of Things Journal* 7(6):5677–5689. doi: 10.1109/JIOT.2020.2980586.

Yang, Xiao, Peng Yu, Lei Feng, Fanqin Zhou, Wenjing Li, Xuesong Qiu 2019. A deep reinforcement learning-based mechanism for cell outage compensation in 5G UDN. Pages 284–289 in 2019 IFIP/IEEE Symposium on Integrated Network and Service Management (IM), held April 8-12 2019, Washington DC. New York: IEEE. doi:10.1109/IWCMC.2019.8766654.

Yao, H., R. Qin and X. Chen. 2019. Unmanned aerial vehicle for remote sensing applications—A review. *Remote Sensing* 11(12):1443. doi: https://doi.org/10.3390/rs11121443.

Yassine, S., S. Kadry and M. A. Sicilia. 2020. Statistical profiles of users' interactions with videos in large repositories: Mining of Khan Academy Repository. *KSII Transactions on Internet and Information Systems* 14(5):2101–2121. doi: https://doi.org/10.1142/S0219265921410188.

Zhang, N., X. Fang, Y. Wang, S. Wu, H. Wu, D. Kar and H. Zhang. 2020. Physical layer authentication for the internet of things via worst-based Gaussian tag embedding. *IEEE Internet of Things Journal*. doi: 10.1109/JIOT.2020.3001597.

New Generation Hyperspectral Sensors DESIS and PRISMA Provide Improved Agricultural Crop Classifications

Itiya Aneece and Prasad S. Thenkabail

Abstract

Using new remote sensing technology to study agricultural crops will support advances in food and water security. The recently launched, new generation spaceborne hyperspectral sensors, German DLR Earth Sensing Imaging Spectrometer (DESIS) and Italian PRecursore IperSpettrale della Missione Applicativa (PRISMA), provide unprecedented data in hundreds of narrow spectral bands for the study of the Earth. Therefore, our overarching goal in this study was to use these data to explore advances that can be made in agricultural research. We selected PRISMA and DESIS images during the 2020 growing season in California's Central Valley to study seven major crops. PRISMA and DESIS images were highly correlated (R^2 of 0.9–0.95). Out of the 235 DESIS bands (400–1000 nm) and 238 PRISMA bands (400–2500 nm), 26 (11%) and 45 (19%) bands, respectively, were optimal to study agricultural crops. These optimal bands provided crop type classification accuracies of 83–90%. Hyperspectral vegetation indices to estimate plant pigment content, stress, biomass, moisture, and cellulose/lignin content were also identified.

Introduction

Twenty-first century remote sensing calls for increased use of data from hyperspectral sensors to advance the study of agricultural crop characteristics. In the past, this advance has been hindered by the lack of availability of spaceborne hyperspectral data covering the planet. The Hyperion Earth Observing-1 (EO-1) sensor was the first spaceborne hyperspectral sensor with publicly available data that provided significant insights into the possibilities of great scientific advances in the study of agricultural crops and vegetation (Bannari *et al.* 2015; Bhojaraja *et al.* 2015; Breunig *et al.* 2011; Houborg *et al.* 2016; Lamparelli *et al.* 2012; Moharana and Dutta 2016; Pan *et al.* 2013; Sonmez and Slater 2016; Thenkabail *et al.* 2013). EO-1 acquired over 70 000 images of the Earth from the year 2001 through 2015 in 242 narrow spectral bands in the 400–2500 nm spectral range (Aneece and Thenkabail 2018). This acquisition was a quantum leap in spectral data relative to multispectral broadband data acquired in a few broad bands such as from Landsat, Moderate Resolution Imaging Spectroradiometer (MODIS), *Satellite pour l'Observation de la Terre* (SPOT), and the *Indian Remote Sensing* (IRS) series of satellites (Mariotto *et al.* 2013; Marshall and Thenkabail 2015). However, the recent launch of advanced spaceborne hyperspectral sensors such as the Italian PRecursore IperSpettrale della Missione Applicativa (PRISMA) and the German Deutsches Zentrum für Luft- und Raumfahrt (DLR) Earth Sensing Imaging Spectrometer (DESIS) onboard the International Space Station (ISS) has opened up a new dimension in remote sensing by offering hundreds of hyperspectral narrowbands (HNB) along the electromagnetic spectrum (Heiden *et al.* 2019; Loizzo *et al.* 2016; Lu *et al.* 2020). PRISMA acquires data from 400 to 2500 nm and DESIS from 400 to 1000 nm (Table 1) and both acquire data

as near-continuous HNB, generating a "spectral signature" rather than a few "data points" as acquired by broadband sensors (Heiden *et al.* 2019; Loizzo *et al.* 2016). In addition, a number of spaceborne hyperspectral sensors were recently launched, such as Germany's Environmental Mapping and Analysis Program (EnMAP) (EnMAP 2022), or planned for launch in the coming years, such as the United States' National Aeronautics and Space Administration (NASA) Surface Biology and Geology (SBG) mission (SBG 2022).

Table 1. Characteristics of hyperspectral data used in this study: Deutsches Zentrum für Luft- und Raumfahrt (DLR) Earth Sensing Imaging Spectrometer (DESIS) and PRecursore IperSpettrale della Missione Applicativa (PRISMA) (Heiden *et al.* 2019; Loizzo *et al.* 2016).

	DESIS	PRISMA
Sensor Type	Spaceborne, on ISS	Spaceborne, polar-orbiting
Spectral Range	400 to 1000 nm	400 to 2500 nm
Number of Bands	235	238
Spectral Resolution	2.55 nm	≤12 nm
Spatial Resolution	30 m	30 m; 5 m for panchromatic band
Signal to Noise Ratio (@ 550 nm)	205	200
Radiometric Resolution	13-bit	12-bit
Swath Width	30 km	30 km

ISS = International Space Station.

DESIS Hyperspectral Data

The German Aerospace Center (formerly DLR) partnered with Teledyne Brown Engineering to design the DLR Earth Sensing Imaging Spectrometer (DESIS) (Heiden *et al.* 2019; Krutz *et al.* 2019; Peschel *et al.* 2018). It is mounted on the Multi-User System for Earth Sensing (MUSES) platform on the International Space Station (ISS) (Heiden *et al.* 2019). Since the sensor is mounted on the ISS, its coverage depends on the overpasses of the ISS which has a non–sun-synchronous and varied orbit, with no repeat cycle (Heiden *et al.* 2019). Despite the challenges of the variable orbit and collection environments, the cost-savings of mounting DESIS on the ISS are substantial (Krutz *et al.* 2019). Since it is unable to point at the sun, moon, or deep space for calibration, DESIS has in-orbit spectral calibration and in-orbit radiometric calibration (Krutz *et al.* 2019). Because of the push broom mechanism, DESIS data are affected by a low smile effect of 1.7 pixels and an even lower keystone effect of 0.3 pixel across the entire field of view and spectral range (Krutz *et al.* 2019). For details on smile, keystone, striping, and rolling shutter corrections, refer to Alonso *et al.* (2019).

DESIS has 235 bands along a spectral range from 400 nm to 1000 nm (Heiden *et al.* 2019; Krutz *et al.* 2019). It has a spectral resolution of

US Geological Survey, Western Geographic Science Center, 2255 N. Gemini Rd., Flagstaff, AZ 86001 (ianeece@usgs.gov).

2.55 nm with Full Width Half Maximum of approximately 3.5 nm, and a radiometric resolution of 13 bits (Alonso *et al.* 2019; Heiden *et al.* 2019). Its spatial resolution is 30 m, with a 30 km swath at 400 km altitude (Heiden *et al.* 2019). The signal to noise ratio (SNR) varies by band, but at 550 nm the SNR is 205 without binning and 406 at 4 bin (Heiden *et al.* 2019).

DESIS data are now available through Teledyne, in several levels of processing (Heiden *et al.* 2019). The Level 0 product consists of raw data (Heiden *et al.* 2019). The Level 1A product consists of tiled images, a browse image, metadata, and quality flags (Heiden *et al.* 2019). The Level 1B product consists of top of atmosphere (TOA) radiance, with systematic and radiometric corrections including those for the rolling shutter and the smile effect (Heiden *et al.* 2019). The Level 1C product has orthorectified, georeferenced TOA data (Heiden *et al.* 2019). Finally, the Level 2A (L2A) data are atmospherically corrected to ground surface reflectance, available with and without terrain correction (Heiden *et al.* 2019). Atmospheric correction is conducted using the DLR's Python Atmospheric Correction algorithm, based on the Atmospheric and Topographic Correction algorithm (Alonso *et al.* 2019). The L2A data include masks for water, land, cloud, shadow, snow, haze, aerosol optical thickness, and water vapor (Alonso *et al.* 2019). Products are available in four spectral binning configurations: *x*1, *x*2, *x*3, and *x*4, resulting in the spectral resolutions of 2.55 nm, 5.1 nm, 7.65 nm, and 10.2 nm, respectively (Alonso *et al.* 2019).

PRISMA Hyperspectral Data

The Italian Space Agency's (ASI) *PRecursore IperSpettrale della Missione Applicativa* (PRISMA) satellite was launched in 2019 and is in sun-synchronous low-Earth orbit at an altitude of 615 to 620 km (Loizzo *et al.* 2016). Details about the sensor design can be found in Labate *et al.* (2009); Loizzo *et al.* (2016); Pignatti *et al.* (2015, 2013). PRISMA's on-board radiometric calibration system includes absolute calibration using the sun, relative calibration using two tungsten lamps, dark calibration using a shutter slit, and on-demand calibration using flat-field calibration and lunar observation (Pignatti *et al.* 2013). Stripes are removed using non-local means (Pignatti *et al.* 2015). Smile and keystone effects also exist, but errors are within 10% of a pixel (Labate *et al.* 2009). Clouds are detected using a discriminant analysis algorithm trained using Hyperion data (Pignatti *et al.* 2015). Atmospheric correction is done using a method similar to Moderate Resolution Atmospheric Transmission (Berk *et al.* 2008), a simplified radiative transfer equation, and a digital elevation model; for more detail on these pre-processing steps, please refer to Pignatti *et al.* (2015).

PRISMA collects data at 66 visible to near infrared (VNIR) bands from 400 to 1010 nm and 171 short-wave infrared (SWIR) bands from 920 to 2500 nm, at 10–12 nm spectral resolution (Loizzo *et al.* 2016; Pignatti *et al.* 2013). VNIR data are collected using a silicon-based detector, while SWIR data are collected using a mercury cadmium telluride diode array (Pignatti *et al.* 2013). In addition, PRISMA collects one panchromatic (PAN) band from 400 to 750 nm (Pignatti *et al.* 2013). The VNIR-SWIR imaging spectrometer and PAN camera are optically integrated to enable hyperspectral and panchromatic data fusion (Loizzo *et al.* 2016; Pignatti *et al.* 2015). Radiometric resolution is 12 bit, the swath width is 30 km, and the ground sampling distance is 30 m for VNIR-SWIR and 5 m for PAN (Loizzo *et al.* 2016). The SNR is greater than 200:1 in the 400 to 1750 nm range, and 100:1 at the 1950 to 2350 nm range (Loizzo *et al.* 2016). The PAN SNR is greater than 240:1 (Loizzo *et al.* 2016).

PRISMA data are available in several levels of processing (Loizzo *et al.* 2016). Level 0 consists of raw data with appended metadata (Loizzo *et al.* 2016). Level 1 consists of radiometrically corrected and calibrated top-of-atmosphere radiance, with masks for clouds, sunglint, and general classification (Loizzo *et al.* 2016). Level 2b consists of geolocated surface radiance (Loizzo *et al.* 2016). Level 2c consists of surface reflectance, with aerosol and water vapor products and cloud masks (Loizzo *et al.* 2016). Lastly, Level 2d consists of geocoded surface reflectance (Loizzo *et al.* 2016). ASI also plans to add subsequent product levels with geophysical, geochemical, biophysical, and biochemical characteristics (Loizzo *et al.* 2016).

Understanding the characteristics of these sensors is of great importance to advance science applications within and between sensors, especially when integrating data from multiple hyperspectral sensors that will become available in the coming years. How do the spectral signatures of these multiple hyperspectral sensors compare with each other? What are their inter-relationships? How do they characterize different applications? What advances do they offer? These are relevant questions for which scientifically sound answers will allow full use of the new generation of hyperspectral data.

Hyperspectral Remote Sensing of Agriculture

Hyperspectral data provide several advantages over multispectral data in the study of agricultural crops because they provide information in hundreds of near-continuous bands along the electromagnetic spectrum; in contrast, multispectral data provide information in only a few broad spectral bands (Aneece and Thenkabail 2018; Kennedy *et al.* 2020; Lu *et al.* 2020; Thenkabail *et al.* 2021). HNB significantly improve classification accuracies of crop types, modeling of crop biochemical and biophysical characteristics, and assessment of other factors such as plant health and stress (Lu *et al.* 2020; Mariotto *et al.* 2013; Marshall *et al.* 2016; Thenkabail *et al.* 2018a, 2018b, 2018c, 2018d; Vali *et al.* 2020).

An extensive study of agricultural crops using hyperspectral remote sensing of old generation sensors has been documented in a four-volume book on the hyperspectral remote sensing of vegetation (Thenkabail *et al.* 2018a, 2018b, 2018c, 2018d). Many hyperspectral studies have been conducted using hand-held, truck-mounted, or airborne hyperspectral sensors. For example, several researchers have used airborne hyperspectral data to study agriculture (Feng *et al.* 2020; Nigam *et al.* 2019; Oki *et al.* 2006; Sahadevan 2021; Salas and Subburayalu 2019; Salas *et al.* 2020; Yang *et al.* 2021) However, these data may be more cost-prohibitive and/or more limited in spatial extent than satellite data. The first-of-its-kind NASA-built EO-1 Hyperion hyperspectral spaceborne sensor collected over 70 000 images across the world from 2001 to 2017 (Aneece and Thenkabail 2018). It was used for various agricultural applications like classification of crop residue, crop types and varieties, and crop conditions (Aneece and Thenkabail 2021; Bannari *et al.* 2015; Bhojaraja *et al.* 2015; Breunig *et al.* 2011; Lamparelli *et al.* 2012; Pan *et al.* 2013; Sonmez and Slater 2016) and for estimating tillage intensity and crop characteristics (Houborg *et al.* 2016; Mariotto *et al.* 2013; Marshall and Thenkabail 2015; Moharana and Dutta 2016; Sonmez and Slater 2016; Thenkabail *et al.* 2013), but has now been decommissioned.

We are now entering a new era of hyperspectral remote sensing with the launch of DESIS onboard ISS in 2018 and the polar-orbiting PRISMA in 2019. A few recent studies have used DESIS (Aneece and Thenkabail 2021) or PRISMA (Cogliati *et al.* 2021; Pepe *et al.* 2020) data to study agriculture. A few have also compared the two for geological (Tripathi and Garg 2021) and aquatic ecosystem applications (Bresciani *et al.* 2022). However, this is one of the first studies, alongside Hank *et al.* (2021), that compares the performance of DESIS and PRISMA in classifying agricultural crops. The differences in the bandwidths and spectral ranges of these sensors influence their use in various agricultural applications. In addition, these sensors are precursors to the recently launched German hyperspectral sensor Environmental Mapping and Analysis Program (EnMAP) and upcoming hyperspectral sensors like NASA's Surface Biology and Geology (SBG) mission. Thus, the study of these sensors will be invaluable once data from EnMAP, SBG, and others become available. One of the major advances of this study was building spectral libraries of major agricultural crops from these new generation sensors. Such libraries are important reference training and validation data for machine learning, deep learning, and artificial intelligence model development (Thenkabail *et al.* 2019). These models will in turn enable classification of crop types, estimation of biophysical and biochemical characteristics, and assessment of crop health and stress.

Overarching Goal and Objectives

The goal of this research was to study the characteristics of two new generation spaceborne hyperspectral sensors: DESIS and PRISMA. Two DESIS and one PRISMA images acquired during the 2020 growing season were used to classify seven major crops (almonds, corn, cotton, grapes, pistachios, rice, and tomatoes) in a study area located in the Central Valley of California, USA. Specific objectives were to:

1. Develop spectral libraries of seven major agricultural crops in California's Central Valley using DESIS (400–1000 nm) and PRISMA (400–2500 nm) new generation hyperspectral sensors;
2. Compare DESIS and PRISMA spectral characteristics of seven major crops in the 400 to 1000 nm spectral range;
3. Determine optimal hyperspectral narrowbands (OHNB) in DESIS and PRISMA data sets;
4. Establish crop type classification accuracies using OHNB from DESIS and PRISMA;
5. Develop and adapt hyperspectral narrowband vegetation indices based on literature review and OHNB.

Materials and Methods

Study Area

The study area is in the Central Valley of California, in north-central California (Figure 1). This area was selected due to the presence of several crop types in a small area that could be captured by DESIS and PRISMA image footprints, its significance in national food security, and image availability. We focused on almonds, corn, cotton, grapes, pistachios, rice, and tomatoes because these were most prevalent in the study area and/or are globally major crops. Planting and harvesting dates for these crops vary by year and farm. For example, corn is planted around May 15th and harvested around October 15th, but those dates can vary by plus or minus 1.5 months (Sacks et al. 2010). Similarly, cotton is planted around April 20th and harvested around October 25th and rice is planted around May 15th and harvested around October 10th, but these dates vary by plus or minus one month (Sacks et al. 2010). Tomatoes are planted around April 1st and harvested before the first frost around December 1st (California Grown, 2022). Almonds, pistachios, and grapevines grow throughout the year. Almonds are harvested August through November, pistachios September through November, and grapes July through November (CUESA, 2022). Below, we describe the hyperspectral data acquired for this study area (Figure 1), followed by reference and validation data.

Data

The goal of this research was to compare two new generation sensors (DESIS and PRISMA), both of which need to be tasked for acquiring

Figure 1. Study area. Location of the study area showing PRecursore IperSpettrale della Missione Applicativa (PRISMA) and Deutsches Zentrum für Luft- und Raumfahrt (DLR) Earth Sensing Imaging Spectrometer (DESIS) image footprints. The red outline indicates overlapping area across all three images. A PRISMA image from June 17, 2020, and two DESIS images from June 18, 2020, and August 8, 2020, were acquired in California's Central Valley. Within the outline is the United States Department of Agriculture Cropland Data Layer showing study crop type distributions for the 2020 growing season. [Source: USDA National Agricultural Statistics Service Cropland Data Layer (2022)].

data rather than providing wall-to-wall coverage as do satellites like Landsat. Getting images over the same area on the same or similar dates is extremely difficult. A study of this nature, however, requires acquisitions on the same or similar dates to build a valid comparison. We were able to achieve this for our study area by acquiring data from DESIS onboard the ISS and PRISMA, a polar-orbiting satellite, by tasking them. Both satellites acquired some images for the study area; we reviewed them and selected those of good quality, similar dates of acquisition within the growing season, and with overlapping footprints. Therefore, three hyperspectral images over the study area were selected with which we were able to compare DESIS and PRISMA images for similar dates, and DESIS June with DESIS August images to assess crops in different growth stages. The two DESIS images were acquired in clear conditions on June 18, 2020, and August 8, 2020, downloaded as Level 2a, surface reflectance products from DLR and Teledyne Brown (German Aerospace Center (formerly DLR) and Teledyne Brown 2022). The PRISMA image with less than 11.5% cloud cover was acquired on June 17, 2020 and downloaded as a Level 2D surface reflectance product from the PRISMA data portal made available by the ASI (Italian Space Agency (ASI) 2022).

The United States Department of Agriculture's National Agricultural Statistics Service Cropland Data Layer (USDA NASS CDL) (USDA National Agricultural Statistics Service Cropland Data Layer 2022) was used as reference data because it consists of yearly wall-to-wall crop type data for the USA. The USDA NASS CDL has relatively high classification accuracies for the selected study crops in the study site (Table 2; USDA NASS 2022) and has been used frequently in research for reference (Boryan and Yang 2021; Hao et al. 2016; Lark et al. 2021; Zhang et al. 2021a; Zhong et al. 2014). As seen in Table 2, all study crops except for corn and grapes have high producer's (87.9%–97.7%), user's (82.7%–99.1%) accuracies, and Kappa values (0.876–0.975) (USDA NASS 2022). While lower than the others, corn and grapes also have relatively high producer's accuracies (74.8% and 77.7%, respectively), user's accuracies (80.5% and 71.2%, respectively) accuracies, and Kappa values (0.744 and 0.774, respectively) (USDA NASS 2022) These two crop types also covered less area than the other study crop types. Thus, we used the high-quality USDA NASS CDL data for reference.

Because the three images had a slight spatial misalignment, we georeferenced them to the USDA NASS CDL in ArcGIS (Version 10.8.1; ESRI 2022) to ensure sampling at the same location across images. The image footprints had enough overlap to select samples across all three images. Sampling was done by generating random points within the overlapping area with a minimum distance of 100 m to avoid autocorrelation and extracting data from all three images. This sampling was also done in ArcGIS (Version 10.8.1; ESRI 2022).

In addition to extracting crop type data (illustrated in Figure 2), confidence information was also extracted from the USDA NASS CDL (USDA National Agricultural Statistics Service Cropland Data Layer 2022). The random samples were then filtered based on confidence, crop type (only retaining study crops), and spectral quality (Table 3). We retained only samples with confidence levels of at least 70%. A lower threshold allowed the introduction of noise and a higher threshold impeded adequate sample size. Fields with double-cropping were excluded to ensure spectral

Table 2. Classification accuracies and Kappa statistics from the United States Department of Agriculture National Agricultural Statistics Service Cropland Data Layer (USDA National Agricultural Statistics Service Cropland Data Layer, 2022) for 2020 in California for the study crops. [Source: (USDA NASS 2022)]

Crop Type	Producer's Accuracy (%)	User's Accuracy (%)	Kappa
Almonds	89.2	87.9	0.884
Corn	74.8	80.5	0.744
Cotton	87.9	86.6	0.876
Grapes	77.7	71.2	0.774
Pistachios	88.6	89.7	0.883
Rice	97.7	99.1	0.975
Tomatoes	88.2	82.7	0.879
Average	86.3	85.4	0.859

signatures were as pure as possible. Data used in this study are available through the ScienceBase Catalog (Aneece and Thenkabail 2022).

Sensor Comparisons

Spectral libraries were used to generate correlation plots in R (Version 4.0.4; R Core Team 2018) using the ggplot2 package (Version 3.3.5; Wickham 2016) comparing DESIS and PRISMA June spectral reflectances at various wavelength ranges: 400 to 1000 nm, 400 to 699 nm, 700 to 759 nm, 760 to 899 nm, and 900 to 1000 nm. Correlation analysis was done within and across crop types. Since only June PRISMA data were available, only June DESIS data were included in this analysis. To establish a fair comparison, broader DESIS bands were simulated by averaging across five bands to approximate PRISMA bandwidths. Linear models were determined in R (Version 4.0.4; R Core Team 2018) using the ggpmisc package (Aphalo 2020). Band averaging was only done for these correlation analyses, not for the optimal band selection or classification analyses described below.

Optimal Bands

Many methods for band selection exist, including principal component analyses, lambda-by-lambda plots, and stepwise-regression (Aneece and Thenkabail 2021; Mariotto et al. 2013; Marshall et al. 2016). In this study, we selected optimal HNB for DESIS and PRISMA data using peak and trough detection, which has successfully been used for finding features in other remote sensing applications (Ali and Clausi 2001; Kutser et al. 2016; Zarco-Tejada et al. 2003). First, peaks and troughs were determined by comparing the reflectance of a band with the reflectances of bands immediately before and immediately after it. This comparison was done separately for each hyperspectral image and each crop type. We counted the number of times each peak or trough wavelength was detected by month and crop type. The most frequently detected wavelengths across images and crop types, which represented consistent patterns at specific locations of the spectrum, were selected for future analysis. Frequencies varied by month and crop type; thus, a single threshold value could not be used. To determine the most important bands for DESIS analysis, we pooled June and August data. Since PRISMA data were only available for June, these were used to determine the most important bands.

Classification Algorithms

The support vector machine supervised classification algorithm was selected to classify crop types and compare classification accuracies across sensors. This algorithm has been used successfully for hyperspectral (including DESIS) analysis (Aneece and Thenkabail 2021; Gopinath et al. 2020; Lin and Yan 2016; Praveen et al. 2016; Puletti et al. 2016; Rodriguez-Galiano et al. 2015), and has outperformed random forest for hyperspectral crop classification (Aneece and Thenkabail 2018, 2021) The linear kernel produced higher accuracies than the more commonly used radial basis function kernel and was thus selected for this analysis.

To compare the abilities of DESIS and PRISMA data to classify agricultural crop types, we conducted classification analyses using the following:
1. 26 DESIS bands at 2.55 nm from 400 to 1000 nm
2. 25 PRISMA bands at ≤12 nm from 400 to 1000 nm
3. 45 PRISMA bands at ≤12 nm from 400 to 2500 nm

Classification comparisons using the first and second data sets would help detect any benefits the narrower DESIS bands may provide over the relatively broader PRISMA bands. A comparison between results using the second and third data sets would help detect the advantages of including SWIR data in classification of these crop types.

Vegetation Indices

PRISMA OHNB were used to adapt vegetation indices found in literature based on narrowbands available in PRISMA data, the optimal band analysis in this study, and extensive literature review (Carter 1994; Clevers 2014; Daughtry 2001; Giovos et al. 2021; Gitelson et al. 2006, 2001, 2002; Hatfield et al. 2019; Hunt et al. 2013; Kandylakis and Karantzalos 2016; Kior et al. 2021; Lichtenthaler et al. 1996; Poley and McDermid 2020; Roberts et al. 2018; Segarra et al. 2020; Serrano et al. 2002; Vogelmann et al. 1993; Wang and Qu 2007; Zarco-Tejada et al. 2005; Zhang et al. 2021b). OHNB were also used to build hyperspectral two-band vegetation indices (HTBVI), which may be used to estimate crop characteristics such as plant pigment content, biomass, stress,
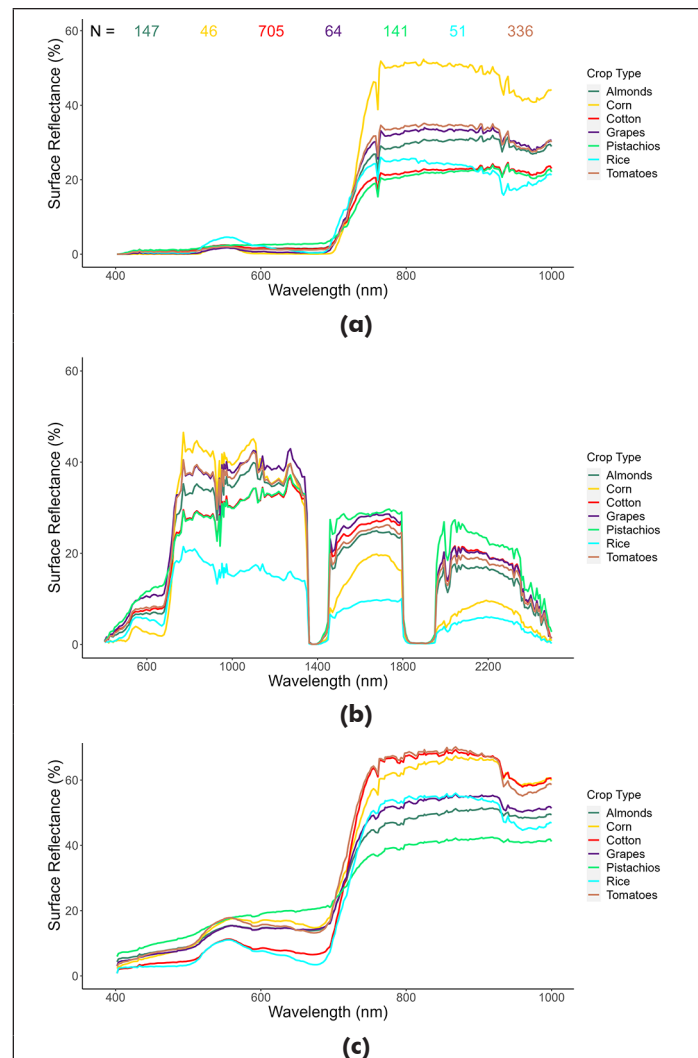
Figure 2. Spectral libraries of study crops. (a) Deutsches Zentrum für Luft- und Raumfahrt (DLR) Earth Sensing Imaging Spectrometer (DESIS) June, (b) PRecursore IperSpettrale della Missione Applicativa (PRISMA) June, and (c) DESIS August spectra, averaged by crop type. The number of spectra (N) used to calculate the average is the same for all three plots.

Table 3. Number of samples used in this study. Reference crop type data were extracted from the United States Department of Agriculture National Agricultural Statistics Service Cropland Data Layer (USDA National Agricultural Statistics Service Cropland Data Layer, 2022).

Number of Samples				
Crop Type	**Training**	**Testing**	**Validation**	**Total**
Almonds	74	36	37	147
Corn	23	12	11	46
Cotton*	50	25	25	705
Grapes	32	16	16	64
Pistachios	70	36	35	141
Rice	26	12	13	51
Tomatoes*	50	25	25	336
Total	325	162	162	1490

*For classification, 100 spectra were randomly selected to balance sample sizes across crop types.

and moisture. The HTBVI can be calculated using Equation 1, where $R_{\lambda 1}$ and $R_{\lambda 2}$ are percent surface reflectances at wavelengths $\lambda 1$ and $\lambda 2$, respectively.

$$HTBVI = \frac{R_{\lambda 1} - R_{\lambda 2}}{R_{\lambda 1} + R_{\lambda 2}} \qquad (1)$$

Results

Sensor Comparisons

As shown in Figure 3, PRISMA and DESIS data in the early growing season (June) had similarly shaped spectral profiles of crops in early vegetative growth. However, PRISMA average reflectances were higher than DESIS for all crops in the visible range, and for most crops in the near-infrared (NIR) range. In contrast, the NIR reflectances for corn and rice were higher in DESIS data than PRISMA. Additionally, the shapes of the spectral profiles in the water absorption trough from 900 to 1000 nm differed between sensors. Average PRISMA spectral profiles were also smoother than DESIS profiles due to wider bands.

When comparing the two DESIS images, one in June and one in August, the August reflectances were higher than June reflectances as would be expected later in the growing season (Figure 4). Also as expected, the green peaks, red troughs, and water absorption features (from plant moisture) were more prominent later in the growing season. Subtle spectral features in the red (600 to 670 nm) and NIR (800 to 900 nm) ranges were also more prominent in August spectra.
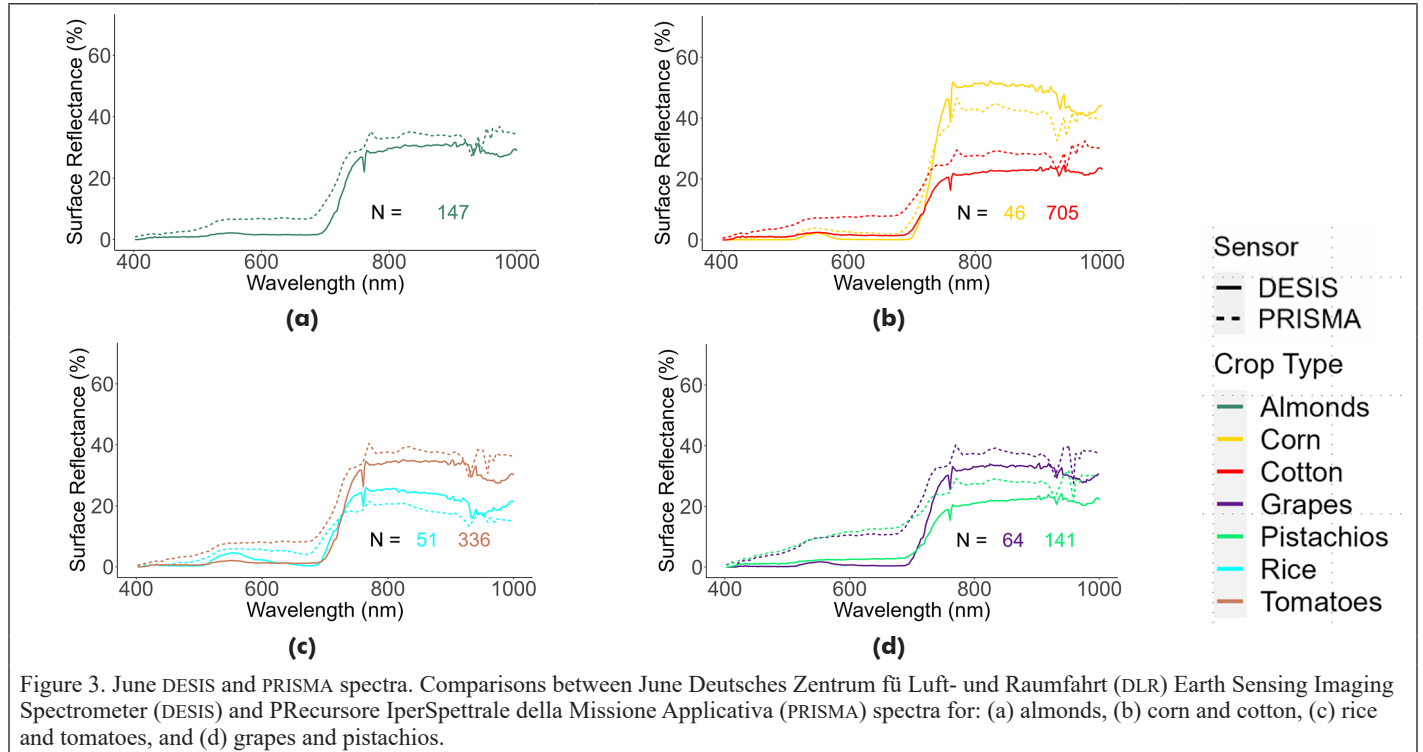
Figure 3. June DESIS and PRISMA spectra. Comparisons between June Deutsches Zentrum fü Luft- und Raumfahrt (DLR) Earth Sensing Imaging Spectrometer (DESIS) and PRecursore IperSpettrale della Missione Applicativa (PRISMA) spectra for: (a) almonds, (b) corn and cotton, (c) rice and tomatoes, and (d) grapes and pistachios.
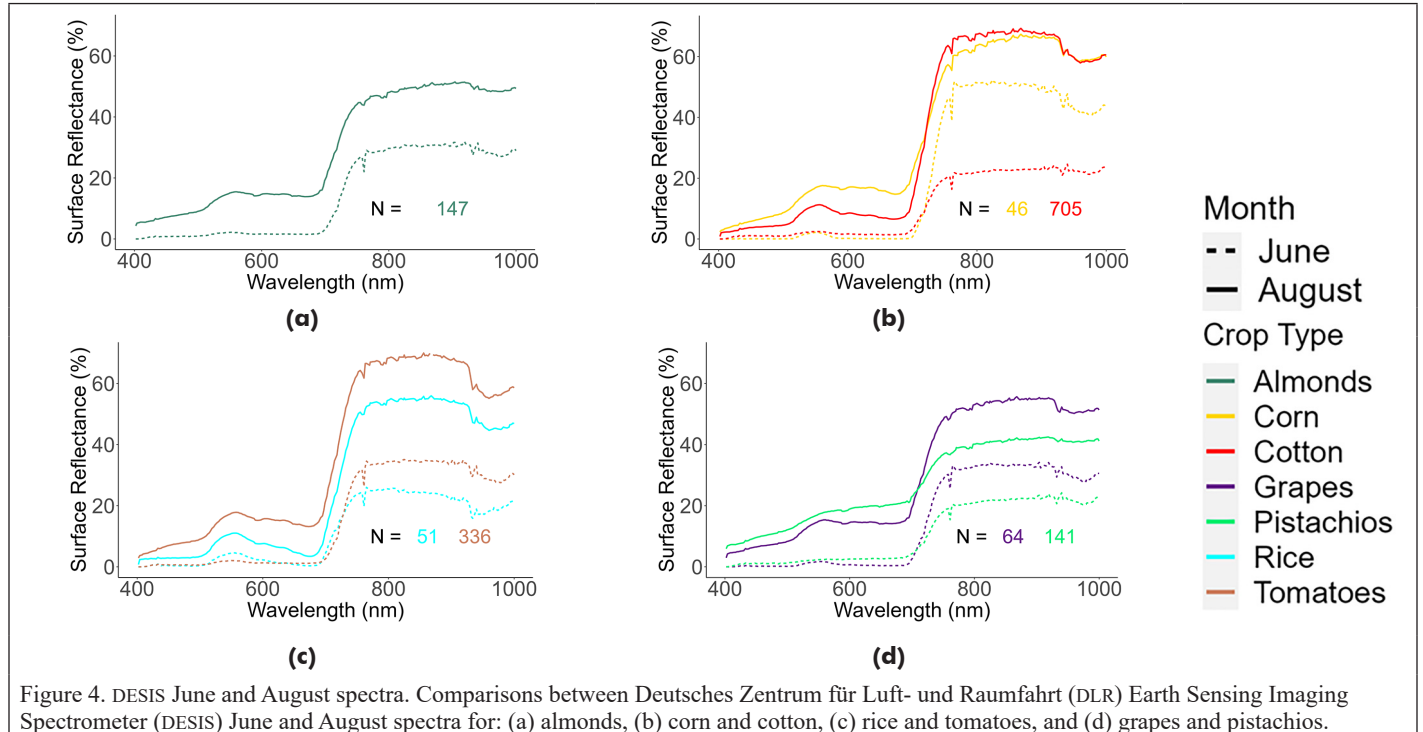
Figure 4. DESIS June and August spectra. Comparisons between Deutsches Zentrum für Luft- und Raumfahrt (DLR) Earth Sensing Imaging Spectrometer (DESIS) June and August spectra for: (a) almonds, (b) corn and cotton, (c) rice and tomatoes, and (d) grapes and pistachios.
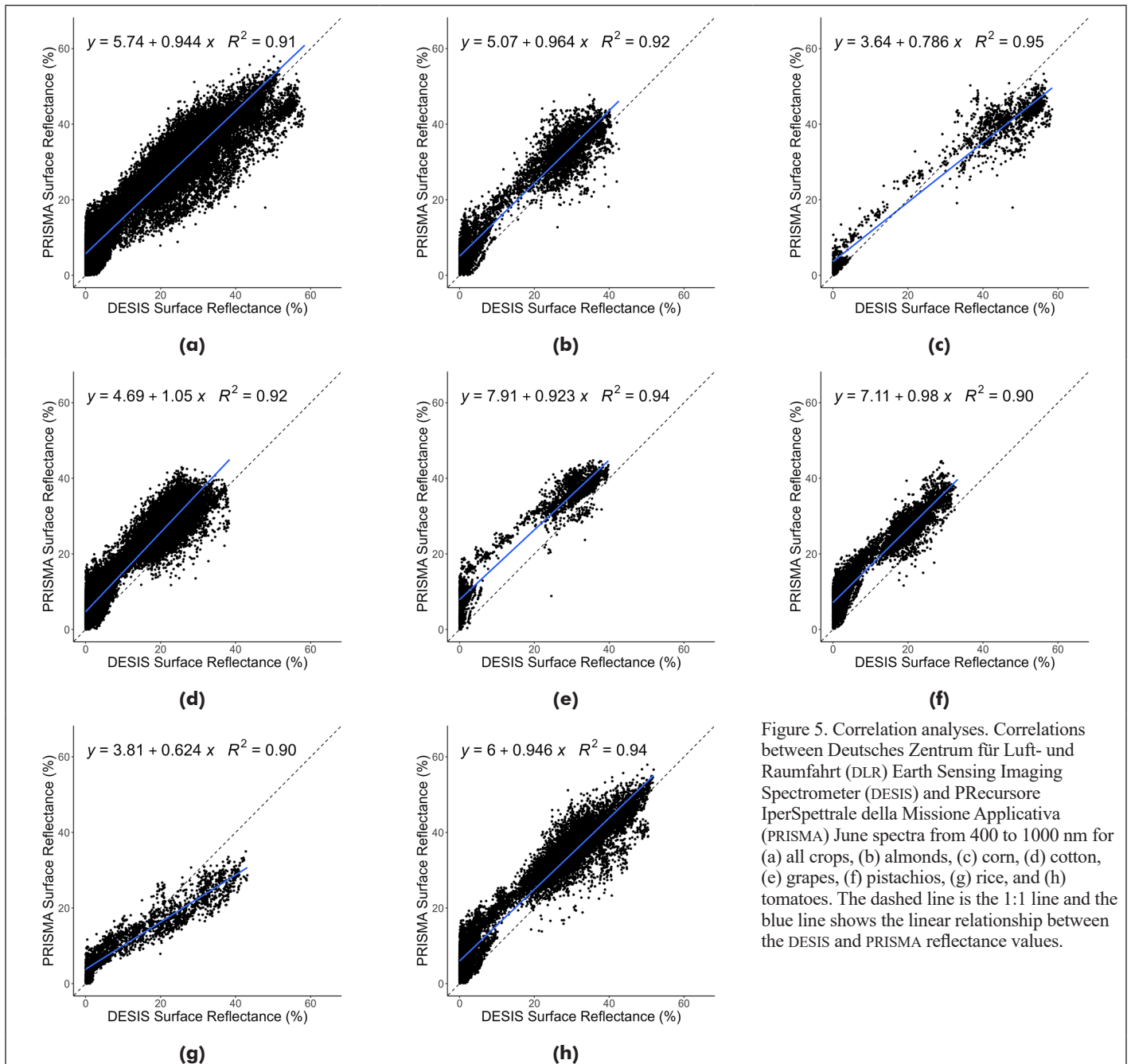
Figure 5. Correlation analyses. Correlations between Deutsches Zentrum für Luft- und Raumfahrt (DLR) Earth Sensing Imaging Spectrometer (DESIS) and PRecursore IperSpettrale della Missione Applicativa (PRISMA) June spectra from 400 to 1000 nm for (a) all crops, (b) almonds, (c) corn, (d) cotton, (e) grapes, (f) pistachios, (g) rice, and (h) tomatoes. The dashed line is the 1:1 line and the blue line shows the linear relationship between the DESIS and PRISMA reflectance values.

In addition to the visual comparisons described below, linear correlation analyses were run between PRISMA and DESIS June spectra (Figure 5 and Table 4). When considering the entire 400 to 1000 nm spectral range, R^2 values ranged from 0.90 to 0.95 across crop types. Correlations were also strong in the 700 to 759 nm range, with R^2 values of 0.77 to 0.94. In contrast, correlations were relatively weak in the 400 to 699 nm range, with R^2 values of 0.11 to 0.44 across crop types, as well as in the 900 to 1000 nm range, with R^2 values of 0.12 to 0.49 for all crops except rice (R^2 0.81). Finally, R^2 values varied from 0.40 to 0.83 in the 760 to 899 nm range.

Optimal Bands

Out of the 235 DESIS bands in the 400 to 1000 nm range, 26 bands (11%) were selected for further analysis, as illustrated in Figure 6 and Table 5. These band center wavelengths have been found useful for various agricultural applications (Aneece and Thenkabail 2021; Mariotto *et al.* 2013; Thenkabail 2015; Thenkabail *et al.* 2021, 2014) including crop type and growth stage classification, disease and stress detection, estimation of biochemical properties such as nitrogen,

Table 4. Coefficients of determination (R^2) for Deutsches Zentrum für Luft- und Raumfahrt (DLR) Earth Sensing Imaging Spectrometer (DESIS) and *PRecursore IperSpettrale della Missione Applicativa* (PRISMA) spectral comparisons.

| Crop(s) | Spectral Range | | | | |
	400–1000 nm	400–699 nm	700–759 nm	760–899 nm	900–1000 nm
All	0.91	0.25	0.78	0.75	0.53
Almonds	0.92	0.28	0.81	0.47	0.17
Corn	0.95	0.11	0.94	0.40	0.16
Cotton	0.92	0.24	0.77	0.61	0.36
Grapes	0.94	0.13	0.93	0.75	0.12
Pistachios	0.90	0.43	0.78	0.79	0.45
Rice	0.90	0.44	0.82	0.83	0.81
Tomatoes	0.94	0.27	0.89	0.78	0.49

Figure 6. DESIS OHNB. Deutsches Zentrum für Luft- und Raumfahrt (DLR) Earth Sensing Imaging Spectrometer (DESIS) optimal hyperspectral narrowbands (OHNB), represented by vertical lines along corn (yellow) and cotton (red) spectra. Brown vertical lines represent peaks while black vertical lines represent troughs.

pigment, protein, and moisture content, and biophysical properties such as biomass/yield (sometimes estimated using Leaf Area Index (LAI)), and vegetation vigor.

Out of the 238 PRISMA bands from 400 to 2500 nm, 45 bands (19%) were selected as optimal for agricultural studies, as illustrated in Figures 7 and 8 and listed in Table 6 (see page 723). As with the selected DESIS bands, these bands have been used for differentiating crop and vegetation types, their growth stages, weeds, and diseased and stressed plants, for estimating crop biomass/yield (and LAI), nitrogen, protein, pigment, water, starch, sugar, cellulose, and lignin content, and for assessing Light Use Efficiency (LUE) (Aneece and Thenkabail 2018, 2021; Delalieux *et al.* 2007; Mariotto *et al.* 2013; Thenkabail *et al.* 2021). Of the selected 45 bands, 25 are within the 400 to 1000 nm range, almost the same number of bands selected from DESIS data along the same spectral range.

Classification Accuracies

The selected OHNB of DESIS and PRISMA in the 400 to 1000 nm range achieved the best results in classifying the seven agricultural crops, with the higher PRISMA overall accuracy of 90% compared to the DESIS

Table 5. Characteristics and relevance of Deutsches Zentrum für Luft- und Raumfahrt (DLR) Earth Sensing Imaging Spectrometer (DESIS) optimal hyperspectral narrowbands.

λ (nm)	Frequency	Feature	Relevance	References
408	99	Peak	Nitrogen, senescence	Thenkabail (2015); Thenkabail *et al.* (2014)
430	263	Trough	Crop classification, biomass/yield, chlorophyll	Mariotto *et al.* (2013); Mobasheri and Rahimzadegan (2012)
433	245	Peak	Crop classification, chlorophyll	Mariotto *et al.* (2013); Mobasheri and Rahimzadegan (2012)
519	8	Peak	Pigment, biomass change	Thenkabail *et al.* (2021)
556	4	Peak	Nitrogen, growth stage, weeds, pigments	Aneece and Thenkabail (2021); Hennessy *et al.* (2020); Ma *et al.* (2019); Mudereri *et al.* (2020); Ren *et al.* (2020); Salem *et al.* (2017); Thenkabail *et al.* (2021)
581	42	Peak	Vegetation vigor, pigments, nitrogen	Thenkabail *et al.* (2021)
588	25	Trough	Biomass/yield	Aneece and Thenkabail (2021); Mariotto *et al.* (2013); Ren *et al.* (2020)
648	124	Trough	Biomass/yield, chlorophyll	Aneece and Thenkabail (2021); Clevers (2014); Mobasheri and Rahimzadegan (2012); Ren *et al.* (2020); Thenkabail *et al.* (2013)
676	11	Trough	Biomass/yield, disease, pigments, weeds, LAI	Aneece and Thenkabail (2018, 2021); Chen *et al.* (2020); Deng *et al.* (2020); Mudereri *et al.* (2020); Roberts *et al.* (2018); Salem *et al.* (2017)
695	180	Trough	Stress, chlorophyll, biomass, LAI	Thenkabail *et al.* (2021, 2004)
718	148	Trough	Stress, pigments, growth stage	Aneece and Thenkabail (2018, 2021); Ma *et al.* (2019); Thenkabail *et al.* (2014, 2013)
735	292	Trough	Nitrogen, LULC classification, growth stage, LAI	Aneece and Thenkabail (2021); Chen *et al.* (2020); Ma *et al.* (2019); Ren *et al.* (2020); Thenkabail *et al.* (2021)
755	10	Peak	Biomass/yield, pigments	Aneece and Thenkabail (2018, 2021); Mariotto *et al.* (2013); Ren *et al.* (2020); Salem *et al.* (2017); Thenkabail *et al.* (2013)
761	865	Trough	Biomass/yield, pigments	Aneece and Thenkabail (2018, 2021); Ren *et al.* (2020); Salem *et al.* (2017); Thenkabail *et al.* (2013)
765	379	Peak	Biomass/yield, pigments	Aneece and Thenkabail (2018, 2021); Ren *et al.* (2020); Salem *et al.* (2017); Thenkabail *et al.* (2013)
783	36	Peak	Biomass/yield, crop classification	Aneece and Thenkabail (2021); Mariotto *et al.* (2013); Ren *et al.* (2020)
796	87	Trough	Biomass/yield, crop classification	Aneece and Thenkabail (2021); Mariotto *et al.* (2013); Ren *et al.* (2020)
813	17	Trough*	Crop classification	Mariotto *et al.* (2013)
850	359	Trough*	Biophysical characteristics, pigments	Thenkabail *et al.* (2021, 2004)
856	273	Peak**	Biomass/yield, pigments, disease, LAI	Aneece and Thenkabail (2018, 2021); Chen *et al.* (2020); Deng *et al.* (2020); Thenkabail *et al.* (2014, 2013)
863	361	Trough	Crop classification	Aneece and Thenkabail (2021); Mariotto *et al.* (2013); Zhang *et al.* (2018)
904	156	Peak	Biomass/yield, pigments, LAI, proteins	Aneece and Thenkabail (2021); Mariotto *et al.* (2013); Mobasheri and Rahimzadegan (2012); Thenkabail *et al.* (2004, 2013); Zhang *et al.* (2018)
919	377	Peak	Moisture, biomass, proteins	Thenkabail *et al.* (2021)
934	885	Trough	Biomass/yield, LAI, oils	Aneece and Thenkabail (2021); Chen *et al.* (2020); Mariotto *et al.* (2013); Mobasheri and Rahimzadegan (2012)
940	684	Peak	Biomass/ yield, LAI, moisture	Aneece and Thenkabail (2021); Chen *et al.* (2020); Clevers (2014); Mariotto *et al.* (2013); Thenkabail *et al.* (2004)
958	370	Trough	Moisture, biomass/yield, protein, growth stage	Aneece and Thenkabail (2021); Chen *et al.* (2020); Ma *et al.* (2019); Thenkabail *et al.* (2014, 2013)

LAI = Leaf Area Index; LULC = Land Use/Land Cover.
*Local peak within larger trough; **Local trough within larger peak.
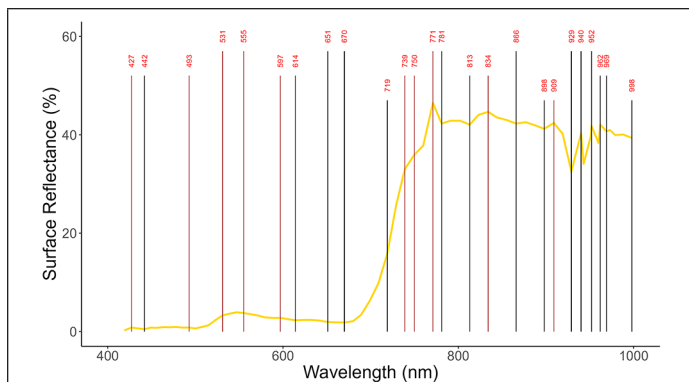
Figure 7. PRISMA OHNB 400–1000 nm. PRecursore IperSpettrale della Missione Applicativa (PRISMA) optimal hyperspectral narrowbands (OHNB) from 400 to 1000 nm, represented by vertical lines along corn spectra. Brown vertical lines represent peaks while black vertical lines represent troughs.
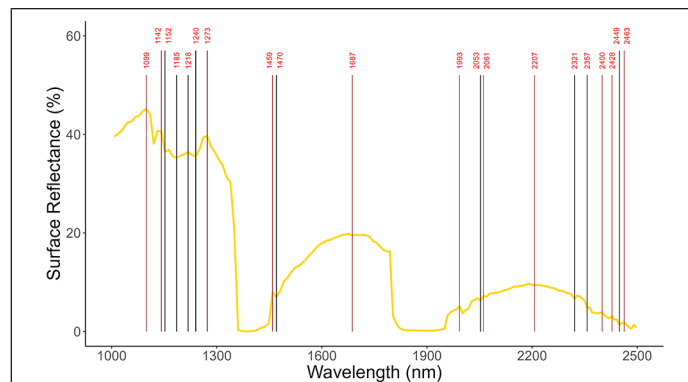
Figure 8. PRISMA OHNB 1000–2500 nm. PRecursore IperSpettrale della Missione Applicativa (PRISMA) optimal hyperspectral narrowbands (OHNB) from 1000 to 2500 nm, represented by vertical lines along corn spectra. Brown vertical lines represent peaks while black vertical lines represent troughs.

overall accuracy of 83% (Table 7). Producer's accuracies for PRISMA ranged from 72–100%, while user's accuracies ranged from 80–100%. Those for DESIS ranged from 63–100% and 67–100%, respectively. Especially of note are the much lower user's accuracy for almonds and producer's accuracy for grapes using DESIS data, caused by grape spectra being misclassified as almonds. This may be due to the spectral similarities of the two for DESIS data, and due to the small area of grapes and large area of almonds in the study area.

However, including PRISMA bands beyond 1000 nm did not result in increased classification accuracies, with an overall accuracy of 89% compared to 90% using only bands from 400 to 1000 nm (Table 7). Using all bands resulted in producer's accuracies of 72–100% and user's accuracies of 73–100%. However, the bands beyond 1000 nm are useful for estimating specific crop biophysical and biochemical properties (Giovos *et al.* 2021; Hatfield *et al.* 2019; Kior *et al.* 2021; Roberts *et al.* 2018).

Vegetation Indices

Since classification accuracies were higher using PRISMA OHNB than when using DESIS OHNB, we focused on using PRISMA bands to build vegetation indices. Out of numerous existing vegetation indices, we selected some of the commonly used indices to estimate plant biomass/density/yield; nitrogen, pigment, moisture, and structural content; and stress (Table 8, see page 724). These were adapted to PRISMA data considering bands used in literature review and spectral features seen in PRISMA data. In addition to adapting existing vegetation indices, we

have suggested HTBVI that may be useful for estimating such biophysical and biochemical characteristics as plant pigment, stress, biomass, moisture, and cellulose/lignin (Table 9).

Discussion

In this paper, we compared data from the new generation hyperspectral sensors PRISMA and DESIS using two DESIS images and one PRISMA image in the growing season of 2020 in the Central Valley of California, USA. We developed spectral libraries for each sensor for seven major

Table 9. Potential PRecursore IperSpettrale della Missione Applicativa (PRISMA) hyperspectral optimal two-band pairs for the hyperspectral two-band vegetation indices (HTBVI) determined in this study.

λ1 (nm)	λ2 (nm)	HTBVI* (Unitless)	Potential Characteristics
555	670	HTBVI-1	
555	493	HTBVI-2	Pigment content
555	614	HTBVI-3	(Anthocyanin, Chlorophyll, Carotenoids)
427	670	HTBVI-4	
719	670	HTBVI-5	Plant stress in visible region
771	719	HTBVI-6	
771	670	HTBVI-7	
771	781	HTBVI-8	Wet and dry biomass, Leaf Area Index, plant height, plant density
834	813	HTBVI-9	
771	969	HTBVI-10	
771	929	HTBVI-11	
834	969	HTBVI-12	
834	929	HTBVI-13	
834	998	HTBVI-14	
1099	1185	HTBVI-15	Plant moisture, water content
1099	998	HTBVI-16	
1099	1240	HTBVI-17	
1273	1185	HTBVI-18	
1142	1152	HTBVI-19	
1273	1240	HTBVI-20	
1459	1470	HTBVI-21	
1687	1470	HTBVI-22	
2061	2053	HTBVI-23	Plant cellulose and/or lignin content
2207	2053	HTBVI-24	
2207	2357	HTBVI-25	Plant stress in shortwave infrared region
2400	2449	HTBVI-26	

*HTBVI = $(R_{\lambda 1} - R_{\lambda 2})/(R_{\lambda 1} + R_{\lambda 2})$.

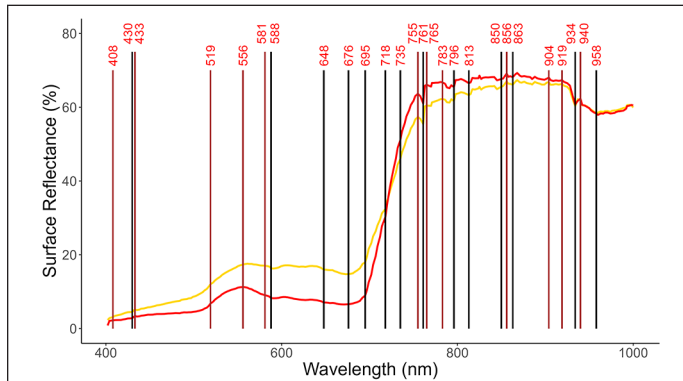Table 7. Classification accuracies for Deutsches Zentrum für Luft- und Raumfahrt (DLR) Earth Sensing Imaging Spectrometer (DESIS) optimal hyperspectral narrowbands (OHNB), PRecursore IperSpettrale della Missione Applicativa (PRISMA) OHNB from 400 to 1000 nm, and PRISMA OHNB from 400 to 2500 nm using support vector machine (Aneece and Thenkabail 2021) classification.

	Producer's (User's) Accuracy (%)		
Crop Type	DESIS	PRISMA_400 to 1000	PRISMA_400 to 2500
Almonds	92 (67)	92 (87)	84 (97)
Corn	100 (100)	100 (100)	100 (100)
Cotton	80 (91)	72 (90)	72 (95)
Grapes	63 (77)	75 (92)	81 (87)
Pistachios	86 (94)	94 (97)	97 (89)
Rice	100 (100)	100 (87)	100 (93)
Tomatoes	68 (85)	96 (80)	96 (73)
Overall Accuracy (%)	83	90	89

Table 6. Characteristics and relevance of *PRecursore IperSpettrale della Missione Applicativa* (PRISMA) optimal hyperspectral narrowbands.

λ (nm)	Frequency	Feature	Relevance	Reference
427	287	Peak	Crop classification, biomass/yield, chlorophyll	Mariotto *et al.* (2013); Mobasheri and Rahimzadegan (2012)
442	351	Trough	Nitrogen, senescing, chlorophyll	Aneece and Thenkabail (2018); Clevers (2014); Thenkabail *et al.* (2013)
493	4	Peak*	Carotenoids, LUE, stress	Aneece and Thenkabail (2018); Hennessy *et al.* (2020); Thenkabail *et al.* (2014, 2013)
531	18	Peak	LUE, stress, disease, growth stage	Aneece and Thenkabail (2021); Deng *et al.* (2020); Hennessy *et al.* (2020); Ma *et al.* (2019); Ren *et al.* (2020); Roberts *et al.* (2018); Thenkabail *et al.* (2014, 2013)
555	11	Peak*	Nitrogen, growth stage, weeds, pigments	Aneece and Thenkabail (2021); Hennessy *et al.* (2020); Ma *et al.* (2019); Mudereri *et al.* (2020); Ren *et al.* (2020); Salem *et al.* (2017); Thenkabail *et al.* (2021)
597	17	Peak	LULC classification	Aneece and Thenkabail (2021); Mariotto *et al.* (2013); Ren *et al.* (2020)
614	50	Trough	LULC classification, biomass, LAI	Aneece and Thenkabail (2021); Chen *et al.* (2020); Ren *et al.* (2020); Thenkabail *et al.* (2004); Zhang *et al.* (2018)
651	61	Trough	Biomass/yield, chlorophyll	Aneece and Thenkabail (2021); Clevers (2014); Ren *et al.* (2020); Thenkabail *et al.* (2013)
670	45	Trough	Biomass/yield, disease, pigments, weeds, LAI	Aneece and Thenkabail (2018, 2021); Chen *et al.* (2020); Deng *et al.* (2020); Mudereri *et al.* (2020); Roberts *et al.* (2018); Salem *et al.* (2017)
719**	0	Trough	Stress, pigments, growth stage	Aneece and Thenkabail (2018, 2021); Ma *et al.* (2019); Thenkabail *et al.* (2014, 2013)
739	119	Peak	Nitrogen, LULC classification, growth stage, LAI	Aneece and Thenkabail (2021); Chen *et al.* (2020); Ma *et al.* (2019); Ren *et al.* (2020); Thenkabail *et al.* (2021)
750	300	Peak*	Biomass/yield, pigments	Aneece and Thenkabail (2018, 2021); Mariotto *et al.* (2013); Ren *et al.* (2020); Salem *et al.* (2017); Thenkabail *et al.* (2013)
771	1484	Peak	Biomass/yield, LAI	Aneece and Thenkabail (2018)
781	792	Trough	Biomass/yield, crop classification	Aneece and Thenkabail (2021); Mariotto *et al.* (2013); Ren *et al.* (2020)
813	614	Trough	Crop classification	Mariotto *et al.* (2013)
834	625	Peak*	Biomass/yield	Aneece and Thenkabail (2021); Mariotto *et al.* (2013)
866	827	Trough	Crop classification	Aneece and Thenkabail (2021); Mariotto *et al.* (2013); Zhang *et al.* (2018)
898	1047	Trough	Biomass/yield, pigments, LAI, proteins	Aneece and Thenkabail (2021); Mariotto *et al.* (2013); Thenkabail *et al.* (2004, 2013); Zhang *et al.* (2018)
909	1136	Peak	Biomass/yield, pigments, protein	Aneece and Thenkabail (2021); Mobasheri and Rahimzadegan (2012); Thenkabail *et al.* (2013); Zhang *et al.* (2018)
929	1488	Trough	Biomass/yield, LAI, oils	Aneece and Thenkabail (2018); Mobasheri and Rahimzadegan (2012)
940	1467	Trough***	Biomass/yield, LAI, water content	Aneece and Thenkabail (2021); Chen *et al.* (2020); Clevers (2014); Mariotto *et al.* (2013); Thenkabail *et al.* (2004)
952	1400	Trough***	Biomass/yield	Mariotto *et al.* (2013)
962	1084	Trough***	Moisture, biomass/yield, protein, growth stage, LAI	Aneece and Thenkabail (2021); Chen *et al.* (2020); Ma *et al.* (2019); Roberts *et al.* (2018); Thenkabail *et al.* (2014, 2013)
969	1026	Trough	Moisture, biomass/yield, starch	Hatfield *et al.* (2019); Mobasheri and Rahimzadegan (2012); Roberts *et al.* (2018); Serrano *et al.* (2002); Thenkabail *et al.* (2021)
998	190	Trough	Moisture, biomass/yield, protein, starch	Aneece and Thenkabail (2018); Mobasheri and Rahimzadegan (2012)
1099	87	Peak	Biomass/yield, LAI	Mariotto *et al.* (2013); Thenkabail *et al.* (2004)
1142	1273	Peak	Biomass/yield, water content, lignin	Clevers (2014); Mariotto *et al.* (2013); Mobasheri and Rahimzadegan (2012); Thenkabail *et al.* (2004)
1152	893	Trough	Biomass/yield	Mariotto *et al.* (2013)
1185	339	Trough	Biomass/yield, moisture	Mariotto *et al.* (2013); Roberts *et al.* (2018)
1218	234	Trough***	Moisture	Aneece and Thenkabail (2018); Hatfield *et al.* (2019); Roberts *et al.* (2018); Thenkabail *et al.* (2004)
1240	1142	Trough	Water sensitivity	Thenkabail *et al.* (2021)
1273	1103	Peak	Biomass/yield	Mariotto *et al.* (2013)
1459	1460	Peak	Moisture, lignin, nitrogen, classification, starch, sugar	Mobasheri and Rahimzadegan (2012); Roberts *et al.* (2018); Serrano *et al.* (2002); Singh *et al.* (2022); Thenkabail *et al.* (2021)
1470	865	Trough	Biomass/yield, moisture	Mariotto *et al.* (2013); Thenkabail *et al.* (2004)
1687	38	Peak*	Biomass/yield, lignin, starch, protein	Mariotto *et al.* (2013); Mobasheri and Rahimzadegan (2012); Serrano *et al.* (2002)
1993	1421	Peak	Biomass/yield, nitrogen	Mariotto *et al.* (2013); Singh *et al.* (2022)
2053	1440	Trough	Biomass/yield, proteins, lignin, cellulose, nitrogen	Mariotto *et al.* (2013); Mobasheri and Rahimzadegan (2012); Roberts *et al.* (2018); Thenkabail *et al.* (2004)
2061	1139	Peak	Moisture, nitrogen, protein	Aneece and Thenkabail (2018); Mobasheri and Rahimzadegan (2012); Serrano *et al.* (2002)
2207	432	Peak*	Lignin, cellulose, sugar, starch, protein	Aneece and Thenkabail (2018); Roberts *et al.* (2018); Thenkabail *et al.* (2014, 2013)
2321	1443	Trough	Biomass/yield, stress moisture, lignin, starch	Mariotto *et al.* (2013); Mobasheri and Rahimzadegan (2012); Thenkabail *et al.* (2004)
2357	1201	Trough	Cellulose, protein, nitrogen	Mobasheri and Rahimzadegan (2012); Thenkabail *et al.* (2021)
2400	1058	Peak	Cellulose, lignin, protein	Roberts *et al.* (2018)
2428	1368	Peak	Undetermined	This study
2449	1319	Trough	Undetermined	This study
2463	1106	Peak	Undetermined	This study

LAI = Leaf Area Index; LULC = Land Use/Land Cover; LUE = Light Use Efficiency.
*Local trough within a peak; **Frequency of 0 but included because important for subsequent analyses; ***Local peak within water absorption.

Table 8. Hyperspectral vegetation indices (HVI) sourced from literature, for which specific narrowband centers were selected from optimal hyperspectral narrowbands (OHNB) of PRecursore IperSpettrale della Missione Applicativa (PRISMA) from this study.

Index	References
Biomass, Vegetation Density, Vegetation Fraction, Leaf Area Index	
Normalized Difference Vegetation Index (NDVI), $NDVI = \dfrac{R_{834} - R_{670}}{R_{834} + R_{670}}$	Giovos et al. (2021); Kior et al. (2021); Segarra et al. (2020); Zhang et al. (2021b)
Green Normalized Difference Vegetation Index (GNDVI), $GNDVI = \dfrac{R_{781} - R_{555}}{R_{781} + R_{555}}$	Giovos et al. (2021); Kior et al. (2021); Poley and McDermid (2020); Zhang et al. (2021b)
Enhanced Vegetation Index (EVI), $EVI = 2.5 * \left(\dfrac{R_{781} - R_{670}}{R_{781} + (C1 * R_{670}) - (C2 * R_{442}) + L} \right)$	Kior et al. (2021); Poley and McDermid (2020); Roberts et al. (2018); Zhang et al. (2021b)
Soil-Adjusted Vegetation Index (SAVI), $SAVI = \dfrac{(R_{791} - R_{670}) * (1 + L)}{R_{791} + R_{670} + L}$	Hatfield et al. (2019); Kior et al. (2021); Roberts et al. (2018)
Atmospherically-Resistant Vegetation Index (ARVI), $ARVI = \dfrac{R_{781} - (R_{670} * R_{442})}{R_{781} + (R_{670} * R_{442})}$	Kior et al. (2021); Roberts et al. (2018)
Nitrogen Content	
Normalized Difference Nitrogen Index (NDNI), $NDNI = \dfrac{log(1/R_{1512}) - log(1/R_{1687})}{log(1/R_{1512}) + log(1/R_{1687})}$	Roberts et al. (2018); Serrano et al. (2002)
Chlorophyll Content	
Modified Chlorophyll Absorption in Reflectance Index (MCARI), $MCARI = [R_{719} - R_{670} - 0.2(R_{719} - R_{555})] * \left(\dfrac{R_{719}}{R_{670}} \right)$	Clevers (2014); Giovos et al. (2021); Kior et al. (2021); Poley and McDermid (2020); Roberts et al. (2018); Zhang et al. (2021b)
Triangular Greenness Index (TGI), $TGI = -0.5 * [228(R_{670} - R_{555}) - 115(R_{670} - R_{442})]$	Hunt et al. (2013); Segarra et al. (2020)
Triangular Vegetation Index (TVI), $TVI = 0.5 * [115(R_{750} - R_{555}) - 195(R_{670} - R_{555})]$	Hatfield et al. (2019); Hunt et al. (2013); Kior et al. (2021); Poley and McDermid (2020)
Gitelson's Chlorophyll Index 1, $Gitelson - chl1 = \left(\dfrac{1}{R_{555}} - \dfrac{1}{R_{781}} \right) * R_{781}$	Giovos et al. (2021); Gitelson et al. (2006); Kandylakis and Karantzalos (2016)
Normalized Pigment Chlorophyll Index (NPCI), $NPCI = \dfrac{R_{670} - R_{427}}{R_{670} + R_{427}}$	Hatfield et al. (2019); Kandylakis and Karantzalos (2016); Kior et al. (2021); Poley and McDermid (2020)
Carotenoid Content	
Gitelson's Carotenoid Index 1, $Gitelson - car1 = \left(\dfrac{1}{R_{515}} - \dfrac{1}{R_{555}} \right) * R_{781}$	Giovos et al. (2021); Gitelson et al. (2006); Kandylakis and Karantzalos (2016)
Blackburn's Carotenoid Index 2, $Blackburn - car2 = \dfrac{R_{802} - R_{471}}{R_{802} + R_{471}}$	Giovos et al. (2021); Gitelson et al. (2002); Kandylakis and Karantzalos (2016)
Anthocyanin Content	
Anthocyanin Reflectance Index 2 (ARI2), $ARI2 = R_{802} * \left(\dfrac{1}{R_{555}} - \dfrac{1}{R_{719}} \right)$	Gitelson et al. (2001); Kior et al. (2021); Roberts et al. (2018)
Anthocyanin Content Index (ACI), $ACI = \dfrac{R_{555}}{R_{781}}$	Giovos et al. (2021); Roberts et al. (2018)
Water Content	
Normalized Difference Water Index (NDWI), $NDWI = \dfrac{R_{866} - R_{1240}}{R_{866} + R_{1240}}$	Clevers (2014); Giovos et al. (2021); Kior et al. (2021)
Water Index (WI), $WI = \dfrac{R_{898}}{R_{969}}$	Clevers (2014); Giovos et al. (2021); Kior et al. (2021); Roberts et al. (2018)
Structural Content	
Cellulose Absorption Index (CAI), $CAI = 0.5(R_{2019} + R_{2207}) - R_{2111}$	Daughtry (2001); Roberts et al. (2018)
Normalized Difference Lignin Index (NDLI), $NDLI = \dfrac{log(1/R_{1756}) - log(1/R_{1687})}{log(1/R_{1756}) + log(1/R_{1687})}$	Roberts et al. (2018); Serrano et al. (2002)
Stress	
Moisture Stress Index (MSI), $MSI = \dfrac{R_{1687}}{R_{929}}$	Giovos et al. (2021); Kior et al. (2021); Roberts et al. (2018)
Carter Index 1, $Ctr1 = \dfrac{R_{695}}{R_{427}}$	Carter (1994); Giovos et al. (2021); Kandylakis and Karantzalos (2016); Kior et al. (2021)
Lichtenthaler Index 2, $Lic2 = \dfrac{R_{442}}{R_{695}}$	Kior et al. (2021); Lichtenthaler et al. (1996); Zarco-Tejada et al. (2005)
Photochemical Reflectance Index (PRI), $PRI = \dfrac{R_{531} - R_{571}}{R_{531} + R_{571}}$	Giovos et al. (2021); Hatfield et al. (2019); Kior et al. (2021); Roberts et al. (2018)
Shortwave Infrared Water Stress Index (SIWSI), $SIWSI = \dfrac{R_{866} - R_{1687}}{R_{866} + R_{1687}}$	Giovos et al. (2021); Hatfield et al. (2019)
Vogelmann Index 2, $Vog2 = \dfrac{R_{739} - R_{750}}{R_{719} + R_{729}}$	Giovos et al. (2021); Vogelmann et al. (1993); Zarco-Tejada et al. (2005)
Normalized Multi-Band Drought Index (NMDI), $NMDI = \dfrac{R_{866} - (R_{1687} - R_{2207})}{R_{866} + (R_{1687} - R_{2207})}$	Kior et al. (2021); Wang and Qu (2007)

agricultural crops (almonds, corn, cotton, grapes, pistachios, rice, and tomatoes). These spectral libraries were used to compare DESIS and PRISMA data characteristics. DESIS data, with narrower bands, had more spectral features (peaks and troughs) than did PRISMA data. However, given the lower classification accuracies using DESIS data, these spectral features may be more noise than information. This performance can be attributed to the issues of sensor SNR related to the very narrow spectral bandwidth of 2.55 nm in DESIS. It has been observed that the signal in the visible portion of the spectrum (400–700 nm) in DESIS is low and the noise in the 760–1000 nm range is high. There is also an issue of overcorrection in DESIS or a sensor-related issue where we have noticed a number of bands with zero reflectivity in the 400–700 nm range. Very narrow bands have high SNR when data are collected from the ground using a spectroradiometer. However, when collected from spaceborne sensors, SNR can be low for very narrow bands such as the 2.55 nm of DESIS relative to the slightly broader ≤12 nm of PRISMA. Field data are needed to determine optimal bandwidths. Thus, when conducting inter-sensor comparisons, differences in sensor characteristics (e.g., bandwidth) and in data preprocessing (e.g., atmospheric correction) need to be kept in mind.

DESIS and PRISMA spectral libraries were used to determine OHNB for each sensor, retaining 11–19% non-redundant hyperspectral data. This percentage of unique information retained is consistent with other hyperspectral literature (Aneece and Thenkabail 2021; Mariotto *et al.* 2013; Marshall *et al.* 2016; Thenkabail *et al.* 2021). Some spectral features seen in DESIS and PRISMA data may be sensor or detector artifacts, or products of the atmospheric correction methods used. For example, the peak at 771 nm in PRISMA data may be influenced by correction of the oxygen absorption feature. The peaks observed in the NIR region, especially in the water absorption feature from 910 to 1000 nm, may be influenced by the low SNR in that spectral range. Determining the level of signal versus noise and artifacts will allow us to evaluate the extrapolability of these results in other areas and using other sensors.

Further, the selected features and corresponding OHNB fall in regions of the spectral profile correlated with plant characteristics as determined in agricultural remote sensing literature (Aneece and Thenkabail 2018, 2021; Chen *et al.* 2020; Clevers 2014; Delalieux *et al.* 2007; Deng *et al.* 2020; Hatfield *et al.* 2019; Hennessy *et al.* 2020; Ma *et al.* 2019; Mariotto *et al.* 2013; Mobasheri and Rahimzadegan 2012; Mudereri *et al.* 2020; Ren *et al.* 2020; Roberts *et al.* 2018; Salem *et al.* 2017; Serrano *et al.* 2002; Singh *et al.* 2022; Thenkabail 2015; Thenkabail *et al.* 2021, 2014; Zhang *et al.* 2018). These OHNB were able to differentiate the seven crop types. The overall accuracies were higher for PRISMA (90%) than for DESIS (83%) in the 400 to 1000 nm range. Using the PRISMA OHNB from 400 to 1000 nm, we obtained producer's accuracies of 72 to 100% and user's accuracies of 80 to 100%. These accuracies were obtained using the support vector machine classification algorithm. Higher accuracies may be obtained using deep learning algorithms (Raczko and Zagajewski 2017). Bands beyond 1000 nm in PRISMA did not result in increased accuracies. However, these bands will likely improve results in studies pertaining to crop biophysical/biochemical properties.

Lastly, PRISMA narrowbands were used to adapt vegetation indices for estimation of various plant characteristics including pigment content, stress, biomass, and cellulose/lignin content (Table 8). For example, the Normalized Difference Vegetation Index (NDVI) has been used in many studies to estimate vegetation growth and health. However, it has issues of saturation in areas with high amounts of vegetation and can be influenced by soil and atmosphere (Roberts *et al.* 2018). The Green Normalized Difference Vegetation Index (GNDVI) is similar to NDVI, but more sensitive to chlorophyll content (Kior *et al.* 2021). The Soil-Adjusted Vegetation Index (SAVI) and the Atmospherically-Resistant Vegetation Index (ARVI) minimize influence from soil properties and atmospheric conditions respectively (Roberts *et al.* 2018). The Enhanced Vegetation Index (EVI) also includes corrections for differences in soil properties and atmospheric conditions and is less susceptible to problems of saturation (Roberts *et al.* 2018).

Many indices also exist for estimating nitrogen and pigment content. Nitrogen is used by plants for building pigments and proteins, influencing the spectral profile throughout the spectral range. The Normalized Difference Nitrogen Index (NDNI) compares the nitrogen absorbance around 1510 nm with the non-absorbing region around 1680 nm (Roberts *et al.* 2018). However, nitrogen estimation can be challenging because absorption features around 1500 and 2180 nm are masked by water absorption features in healthy plants (Clevers 2014).

Several chlorophyll indices use the chlorophyll absorption band around 670 nm and the green peak around 550 nm. For example, the Chlorophyll Absorption in Reflectance Index (CARI) compares the reflectance around 670 nm with reflectance in the red (R) region, around 700 nm. The modified CARI (MCARI) includes a ratio between the NIR and R regions to compensate for soil (Roberts *et al.* 2018). The Triangular Greenness Index (TGI) allows for estimation of chlorophyll without the need for a red-edge band; it instead uses reflectances around 670, 550, and 480 nm (Hunt *et al.* 2013). Similarly, the Triangular Vegetation Index (TVI) uses reflectances around 670, 550, and 750 nm to form a triangle to estimate chlorophyll and LAI (Hunt *et al.* 2013; Kior *et al.* 2021). The Normalized Pigment Chlorophyll Index (NPCI) estimates the ratio of total pigments to chlorophyll and can be used to assess plant stress (Penuelas *et al.* 1994). Carotenoids play a role in photosynthesis and the protection of chlorophyll from photooxidation (Gitelson *et al.* 2006; Roberts *et al.* 2018). Both chlorophylls and carotenoids influence spectral reflectances in the green region. Thus, bands to estimate concentrations of individual pigment types need to use bands that are influenced only by one pigment type, as done by Gitelson *et al.* (2006) and Blackburn (1998) to estimate carotenoid content. Carotenoids are most easily detected during plant senescence, when chlorophyll breaks down while carotenoids are still intact (Roberts *et al.* 2018). Similarly, anthocyanins also play a role during periods of stress, and are thought to reduce photoinhibition (Roberts *et al.* 2018). Leaves have a reddish color when high in anthocyanin content. The Anthocyanin Reflectance Index (ARI) takes the difference between the reciprocals of the green and red-edge reflectances. ARI-2 refines the estimation by adding a weighting through NIR reflectance (Roberts *et al.* 2018). The Anthocyanin Content Index uses the ratio between green and NIR reflectances to measure the drop in green leaf reflectance with increasing anthocyanin content (Roberts *et al.* 2018).

For estimating plant moisture/water content, the Normalized Difference Water Index (NDWI) compares reflectance values around 860 and 1240 nm to estimate plant moisture while minimizing atmospheric influences (Kior *et al.* 2021). The Water Index, also called the Water Band Index, compares reflectances at 900 and 970 nm to detect the amount of water absorption and estimate plant moisture (Roberts *et al.* 2018). To estimate cellulose content, the Cellulose Absorption Index (CAI) uses the cellulose absorption band around 2101 nm and surrounding bands outside of the absorption feature (Roberts *et al.* 2018). Similarly, the Normalized Difference Lignin Index (NDLI) compares reflectance at the lignin absorption band around 1754 nm with the non-absorbing region around 1680 nm (Roberts *et al.* 2018).

As plants face several stressors, there are many indices used to estimate plant stress. The Moisture Stress Index (MSI) compares reflectance at the water absorption band around 1650 nm with NIR reflectance (either around 830 nm or 927 nm) (Roberts *et al.* 2018). The Carter Index 1 (Ctr1) uses reflectances around 695 and 420 nm to estimate stress regardless of the stressor (Carter 1994). Similarly, the Lichtenthaler Index 2 (Lic2) uses reflectances around 695 and 440 nm to detect inhibition of photosynthesis and stress (Lichtenthaler *et al.* 1996). The Photochemical Reflectance Index measures the decrease in reflectance at 531 nm by comparing it with reflectance at 570 nm (Roberts *et al.* 2018). This decrease can be used to estimate plant stress or carotenoid content (Roberts *et al.* 2018). The Shortwave Infrared Water Stress Index (SIWSI) uses reflectances around 860 and 1650 nm to detect water stress (Hatfield *et al.* 2019). The Vogelmann Index 2 uses red edge bands to detect low chlorophyll levels and estimate stress (Giovos *et al.* 2021; Vogelmann *et al.* 1993). Finally, the Normalized

Multi-Band Drought Index (NMDI) uses the water absorption bands around 860, 1640, and 2130 nm (MODIS bands 2, 6, and 7, respectively) to estimate plant and soil moisture to assess drought stress (Wang and Qu 2007).

These existing vegetation indices were adapted to PRISMA data considering available bands, spectral features seen in the spectral libraries, and PRISMA OHNB. The bands included in these indices sometimes differ from those in literature because of differences in bandwidths across sensors. For example, the NMDI was built using available MODIS bands, but may benefit from using narrower PRISMA bands like those recommended here. The recommended bands are also sometimes adjusted to take into account PRISMA spectral features. For example, 550 nm is often used to represent the green band. Here, we found the green peak most often occurred at 555 nm, and thus recommended this to be used (Table 8). Index parameters also needed to be adjusted when adjusting bands in certain indices. For example, the values of 228 and 115 in the TGI represent differences between band values (i.e., 670 – 442 = 228 and 670 – 555 = 115). A similar adjustment was made to the TVI. In cases where very broad spectral regions were indicated in the equations (e.g., NIR/R), we used literature review and PRISMA features/OHNB to recommend narrowbands. Further exploration, especially in conjunction with field measurements, will help further refine these recommendations.

In addition to adapting existing vegetation indices, we suggested HTBVI that may be used to estimate various plant biophysical and biochemical characteristics using PRISMA narrowbands (Table 9). Using the existing knowledge-base (for example Thenkabail *et al.* (2018a, 2018b, 2018c, 2018d)), we have attempted to define spectral bands of importance considering various peaks and troughs throughout the electromagnetic spectrum. These important peaks and troughs were determined based on their consistent occurrence and patterns observed across crop types and dates using large sample sizes and literature review. Regardless, further research, alongside field-observed data, will allow each of these HTBVI to be specifically linked to a particular biochemical or biophysical characteristic. These suggested indices are meant to serve as a pathway for further research.

The DESIS and PRISMA spectral libraries developed here alongside others in the Global Hyperspectral Imaging Spectral-libraries of Agricultural crops (GHISA) project (Thenkabail *et al.* 2019), will facilitate development and automated deployment of crop type machine/deep learning classification algorithms. In addition, such inter-sensor comparisons at overlapping study areas and time-periods are crucial for future workflows taking advantage of these and upcoming hyperspectral sensors for crop type mapping and crop productivity estimations.

Of course, there is much work to be done. Our goal for this study was to assess any advantages that would be provided by the narrower DESIS bands; however, future work could include comparing classification accuracies using the various binned DESIS products. It also includes testing of the adapted VI and suggested HTBVI with ground measurements of plant characteristics. Additionally, small spectral features from DESIS data need to be examined alongside field data to determine whether they encompass noise or information. These sensor comparisons could be furthered by adding future sensors such as the recently launched German EnMAP and upcoming US NASA SBG sensors. The data from these future sensors will also increase image availability for time-series classification analyses.

Conclusions

DESIS and PRISMA new generation spaceborne hyperspectral sensors were used to develop spectral libraries of seven agricultural crops (almonds, corn, cotton, grapes, pistachios, rice, and tomatoes) in the Central Valley of California, USA for the growing season of 2020. Inter-sensor comparisons of these two hyperspectral sensors indicated high correlations with R^2 values of 0.90–0.95. The study established 26 DESIS optimal hyperspectral narrow bands (OHNB) (11% of the 235 DESIS HNB from 400 to 1000 nm) and 45 PRISMA OHNB (19% of the 238 PRISMA HNB from 400 to 2500 nm) for the study of agricultural crops. The rest (89% of DESIS and 81% of PRISMA) of the bands were found to be redundant. The seven agricultural crops were classified with overall accuracies of 83–90% using these OHNB. Producer's accuracies of individual crop types for PRISMA ranged from 72 to 100% whereas those for DESIS ranged from 63 to 100%. User's accuracies of individual crop types for PRISMA ranged from 80 to 100% while those from DESIS ranged from 67 to 100%. Overall, PRISMA yielded substantially higher classification accuracies as a result of higher signal to noise ratio. HNB have shown great advances in the study of agricultural crops and vegetation. However, this study indicates there is an optimal bandwidth for spaceborne sensors below which SNR ratio decreases. Here, the ≤12 nm bandwidth of PRISMA provided more signal and less noise than the 2.55 nm bandwidth of DESIS. Finally, based on literature review and these OHNB, we developed hyperspectral two-band vegetation indices and adapted existing vegetation indices for PRISMA bands to estimate plant pigment content, plant stress, wet and dry biomass, plant water/moisture content, and cellulose/lignin content.

References
Ali, M. and D. Clausi. (2001). Using the canny edge detector for feature extraction and enhancement of remote sensing images. Pages 2298–2300 in *Proceedings IEEE 2001 International Geoscience and Remote Sensing Symposium*, vol. 5, held in Sydney, Australia, 9–13 July 2001.

Alonso, K., M. Bachmann, K. Burch, E. Carmona, D. Cerra, R. de los Reyes, D. Dietrich, U. Heiden, A. Holderlin, J. Ickes, U. Knodt, D. Krutz, H. Lester, R. Muller, M. Pagnutti, P. Reinartz, R. Richter, R. Ryan, I. Sebastian and M. Tegler. 2019. Data products, quality and validation of the DLR Earth Sensing Imaging Spectrometer (DESIS). *Sensors* 19(4471):1–44.

Aneece, I. and P. Thenkabail. 2018. Accuracies achieved in classifying five leading world crop types and their growth stages using optimal Earth Observing-1 Hyperion hyperspectral narrow-bands on Google Earth Engine. *Remote Sensing* 10:29.

Aneece, I. and P. Thenkabail. 2021. Classifying crop types using two generations of hyper-spectral sensors (Hyperion and DESIS) with machine learning on the cloud. *Remote Sensing* 13(4704):1–24.

Aneece, I. and P. S. Thenkabail. 2022. *DESIS and PRISMA Spectral Library of Agricultural Crops in California's Central Valley in the 2020 Growing Season*. U.S. Geological Survey Data Release. https://doi.org/10.5066/P98LO5D4.

Aphalo, P. 2020. *Learn R: As a Language. The R Series.* Boca Raton and London: Chapman and Hall/CRC Press.

Bannari, A., K. Staenz, C. Champagne and K. Khurshid. 2015. Spatial variability mapping of crop residue using Hyperion (EO-1) hyperspectral data. *Remote Sensing* 7:8107–8127.

Berk, A., G. Anderson, P. Acharya and E. Shettle. 2008. *MODTRAN 5.2.0.0 User's Manual*. Technical report.

Bhojaraja, B., A. Shetty, M. K. Nagaraj and P. Manju. 2015. Age-based classification of areca nut crops: A case study of Channagiri, Karnataka, India. *Geocarto International* 1–11.

Blackburn, G. 1998. Quantifying chlorophylls and carotenoids at leaf and canopy scales: An evaluation of some hyperspectral approaches. *Remote Sensing of Environment* 66(3):273–285.

Boryan, C. and Z. Yang. 2021. Integration of the cropland data layer based automatic stratification method into the traditional area frame construction process. *Survey Research Methods* 11(3):289–306.

Bresciani, M., C. Giardino, A. Fabbretto, A. Pellegrino, S. Mangano, G. Free and M. Pinardi. 2022. Application of new hyperspectral sensors in the remote sensing of aquatic ecosystem health: Exploiting PRISMA and DESIS for four Italian lakes. *Resources* 11(8):1–17.

Breunig, F., L. Galvao, A. Formaggio and J. Epiphanio. 2011. Classification of soybean varieties using different techniques: Case study with Hyperion and sensor spectral resolution simulations. *Journal of Applied Remote Sensing* 5:053533-1-053533-15.

California Grown. 2022. *California Grown: What's in Season in California?* <https://californiagrown.org/blog/whats-in-season-in-california> Accessed 9 June 2022.

Carter, G. 1994. Ratios of leaf reflectances in narrow wavebands as indicators of plant stress. *International Journal of Remote Sensing* 15:697–703.

Chen, Z., K. Jia, C. Xiao, D. Wei, X. Zhao, J. Lan, X. Wei, Y. Yao, B. Wang, Y. Sun and L. Wang. 2020. Leaf area index estimation algorithm for GF-5 hyperspectral data based on different feature selection and machine learning methods. *Remote Sensing* 12(2110):1–23.

Clevers, J. 2014. Chapter 22: Beyond NDVI: Extraction of biophysical variables from remote sensing imagery. In *Remote Sensing and Digital Image Processing,* volume Land Use and Land Cover Mapping in Europe: Practices and Trends. New York: Springer, pp. 363–381.

Cogliati, S., F. Sarti, L. Chiarantini, M. Cosi, R. Lorusso, E. Lopinto, F. Miglietta, L. Genesio, L. Guanter, A. Damm, S. Pérez-López, D. Scheffler, G. Tagliabue, C. Panigada, U. Rascher, T. Dowling, C. Giardino and R. Colombo. 2021. The PRISMA imaging spectroscopy mission: Overview and first performance analysis. *Remote Sensing of Environment* 262:112499.

CUESA (Center for Urban Education about Sustainable Agriculture). 2022. Center for Urban Education about Sustainable Agriculture—Seasonality Chart: Fruit and Nuts. <https://cuesa.org/eat-seasonally/charts/fruit> Accessed 09 June 2022.

Daughtry, C. 2001. Discriminating crop residues from soil by shortwave infrared reflectance. *Agronomy Journal* 93:125–131.

Delalieux, S., J. Aardt, W. Keulemans, E. Schrevens and P. Coppin. 2007. Detection of biotic stress (Venturia inaequalis) in apple trees using hyperspectral data: Non-parametric statistical approaches and physiological implications. *European Journal of Agronomy* 27:130–143.

Deng, X., Z. Zhu, J. Yang, Z. Zheng, Z. Huang, X. Yin, S. Wei and Y. Lan. 2020. Detection of citrus huanglongbing based on multi-input neural network model of UAV hyperspectral remote sensing. *Remote Sensing* 12(2678):1–20.

EnMAP. 2022. Welcome to EnMAP: The German Spaceborne Imaging Spectrometer Mission. <https://www.enmap.org/> Accessed 17 June 2022.

ESRI (Environmental Systems Research Institute). 2022. *ArcGIS Desktop: Release 10.8.1*. Redlands, CA: Environmental Systems Research Institute.

Feng, L., Z. Zhang, Y. Ma, Q. Du, P. Williams, J. Drewry and B. Luck. 2020. Alfalfa yield prediction using UAV-based hyperspectral imagery and ensemble learning. *Remote Sensing* 12(2028):1–24.

German Aerospace Center (formerly DLR) and Teledyne Brown. 2022. TCloud: Teledyne Technologies. <http://tcloudhost.com/> Last accessed [01/15/2022]. Last accessed [06/09/2022].

Giovos, R., D. Tassopoulos, D. Kalivas, N. Lougkos and A. Priovolou. 2021. Remote sensing vegetation indices in viticulture: A critical review. *Agriculture* 11(457):1–20.

Gitelson, A., G. Keydan and M. Merzlyak. 2006. Three-band model for noninvasive estimation of chlorophyll, carotenoids, and anthocyanin content in higher plant leaves. *Geophysical Research Letters* 33:38–45.

Gitelson, A., M. Merzlyak and O. Chivkunova. 2001. Optical properties and nondestructive estimation of anthocyanin content in plant leaves. *Photochemistry and Photobiology* 71:38–45.

Gitelson, A., Y. Zur, O. Chivkunova and M. Merzlyak. 2002. Assessing carotenoid content in plant leaves with reflectance spectroscopy. *Photochemistry and Photobiology* 75(3):272–281.

Gopinath, G., N. Sasidharan and U. Surendran. 2020. Land use classification of hyperspectral data by spectral angle mapper and support vector machine in humid tropical region of India. *Earth Science Information* 13:633–640.

Hank, T., K. Berger, M. Wocher, M. Danner and W. Mauser. 2021. Introducing the potential of the EnMAP-box for agricultural applications using DESIS and PRISMA data. Pages 467–470 in *Proceedings 2021 IEEE International Geoscience and Remote Sensing Symposium*, held in Brussels, Belgium, 11–16 July 2021.

Hao, P., L. Wang, Y. Zhan, C. Wang, Z. Niu and M. Wu. 2016. Crop classification using crop knowledge of the previous-year: Case study in Southwest Kansas, USA. *European Journal of Remote Sensing* 49(1):1061–1077.

Hatfield, J., J. Prueger, T. Sauer, C. Dold, P. O'Brien and K. Wacha. 2019. Applications of vegetative indices from remote sensing to agriculture: Past and future. *Inventions* 4(71):1–17.

Heiden, U., M. Bachmann, K. Alonso, E. Carmona, D. Cerra, D. Dietrich, M. Langheinrich, R. de los Reyes, R. Mueller, N. Pinnel and V. Ziel. 2019. DESIS imaging spectrometer data access and synergistic use with other ISS earth observing instruments. In *Proceedings Workshop on International Cooperation in Spaceborne Imaging Spectroscopy*, held in Frascati, Italy, 9–11 July 2019, https://elib.dlr.de/129175/.

Hennessy, A., K. Clarke and M. Lewis. 2020. Hyperspectral classification of plants: A review of waveband selection generalisability. *Remote Sensing* 12(113):1–27.

Houborg, R., M. McCabe, Y. Angel and E. Middleton. 2016. Detection of chlorophyll and leaf area index dynamics from sub-weekly hyperspectral imagery. In *Remote Sensing for Agriculture, Ecosystems, and Hydrology XVIII*, volume 9998, pp. 999812–1-999812–11. https://doi.org/10.1117/12.2241345.

Hunt, E., P. Doraiswamy, J. McMurtrey, C. Daughtry, E. Perry and A. Bakhyt. 2013. A visible band index for remote sensing leaf chlorophyll content at the canopy scale. *Publications from USDA-ARS / UNL Faculty,* pp. 1–13.

Italian Space Agency (ASI). 2022. ASI data portal, PRISMA Catalogue Client. <http://asi.it> Accessed 09 June 2022.

Kandylakis, Z. and K. Karantzalos. 2016. Precision viticulture from multitemporal, multispectral very high resolution satellite data. Pages 919–925 in *Proceedings of the XXII ISPRS Congress,* volume XLI-B8, held in Prague, Czech Republic.

Kennedy, B., D. King and J. Duffe. 2020. Comparison of empirical and physical modelling for estimation of biochemical and biophysical vegetation properties: Field scale analysis across an Arctic bioclimatic gradient. *Remote Sensing* 12:1–41.

Kior, A., V. Sukhov and E. Sukhova. 2021. Application of reflectance indices for remote sensing of plants and revealing actions of stressors. *Photonics* 8(582):1–27.

Krutz, D., R. Muller, U. Knodt, B. Gunther, I. Walter, I. Sebastian, T. Sauberlich, R. Reulke, E. Carmona, A. Eckardt, H. Venus, C. Fischer, B. Zender, S. Arloth, M. Lieder, M. Neidhardt, U. Grote, F. Schrandt, S. Gelmi and A. Wojtkowiak. 2019. The instrument design of the DLR Earth Sensing Imaging Spectrometer (DESIS). *Sensors* 19(1622):1–16.

Kutser, T., B. Paavel, C. Verpoorter, M. Ligi, T. Soomets, K. Toming and G. Casal. 2016. Remote sensing of black lakes and using 810 nm reflectance peak for retrieving water quality parameters of optically complex waters. *Remote Sensing* 8(6). https://doi.org/10.3390/rs8060497.

Labate, D., M. Ceccherini, A. Cisbani, V. De Cosmo, C. Galeazzi, L. Giunti, M. Melozzi, S. Pieraccini and M. Stagl. 2009. The PRISMA payload optomechanical design, a high performance instrument for a new hyperspectral mission. *Acta Astronautica* 65:1429–1436.

Lamparelli, R., J. Johann, E. Dos Santos, J. Esquerdo and J. Rocha. 2012. Use of data mining and spectral profiles to differentiate condition after harvest of coffee plants. *Engenharia Agricultura Jaboticabal* 32(1):184–196.

Lark, T., I. Schelly and H. Gibbs. 2021. Accuracy, bias, and improvements in mapping crops and cropland across the United States using the USDA Cropland Data Layer. *Remote Sensing* 13(968):1–29.

Lichtenthaler, H., M. Lang, M. Sowinska, F. Heisel and J. Miehe. 1996. Detection of vegetation stress via a new high resolution fluorescence imaging system. *Journal of Plant Physiology* 148:599–612.

Lin, Z. and L. Yan. 2016. A support vector machine classifier based on a new kernel function model for hyperspectral data. *GIScience and Remote Sensing* 53(1):85–101.

Loizzo, R., C. Ananasso, R. Guarini, E. Lopinto, L. Candela and A. Pisani. 2016. The PRISMA hyperspectral mission. In *Proceedings Workshop on Living Planet Symposium*, held in Prague, Czech Republic, 9–13 May 2019. <https://lps16.esa.int/>.

Lu, B., P. Dao, J. Liu, Y. He and J. Shang. 2020. Recent advances of hyperspectral imaging technology and applications in agriculture. *Remote Sensing* 12:1–44.

Ma, H., K. Zhao, X. Jin, J. Ji, Z. Qiu and S. Gao. 2019. Spectral difference analysis and identification of different maturity blueberry fruit based on hyperspectral imaging using spectral index. *International Journal of Agriculture and Biological Engineering* 134(3):134–140.

Mariotto, I., P. Thenkabail, A. Huete, T. Slonecker and A. Platonov. 2013. Hyperspectral versus multispectral crop-productivity modeling and type discrimination for the HyspIRI mission. *Remote Sensing of Environment* 139:291–305.

Marshall, M. and P. Thenkabail. 2015. Advantage of hyperspectral EO-1 Hyperion over multi-spectral IKONOS, GeoEye-1, WorldView-2, Landsat ETM+, and MODIS vegetation indices in crop biomass estimation. *ISPRS Journal of Photogrammetry and Remote Sensing* 108:205–218.

Marshall, M., P. Thenkabail, T. Biggs and K. Post. 2016. Hyperspectral narrowband and multispectral broadband indices for remote sensing of crop evapotranspiration and its components (transpiration and soil evaporation). *Agricultural and Forest Meteorology* 218–219:122–134.

Mobasheri, M. and M. Rahimzadegan. 2012. Introduction to protein absorption lines index for relative assessment of green leaves protein content using EO-1 Hyperion datasets. *Journal of Agricultural Science and Technology* 14:135–147.

Moharana, S. and S. Dutta. 2016. Spatial variability of chlorophyll and nitrogen content of rice from hyperspectral imagery. *ISPRS Journal of Photogrammetry and Remote Sensing* 122:17–29.

Mudereri, B., T. Dube, S. Niassy, E. Kimathi, T. Landmann, Z. Khan and E. Abdel-Rahman. 2020. Is it possible to discern Striga weed (Striga hermonthica) infestation levels in maize agro-ecological systems using in-situ spectroscopy? *International Journal of Applied Earth Observation and Geoinformation* 85(102008):1–14.

Nigam, R., R. Tripathy, S. Dutta, N. Bhagia, R. Nagori, K. Chandrasekar, R. Kot, B. Bhattacharya and S. Ustin. 2019. Crop type discrimination and health assessment using hyperspectral imaging. *Current Science* 116(7):1108–1123.

Oki, K., L. Shan, T. Saruwatari, T. Suhama and K. Omasa. 2006. Evaluation of supervised classification algorithms for identifying crops using airborne hyperspectral data. *International Journal of Remote Sensing* 27(10):1993–2002.

Pan, Z., J. Huang and F. Wang. 2013. Multi range spectral feature fitting for hyperspectral imagery in extracting oilseed rape planting area. *International Journal of Applied Earth Observation and Geoinformation* 25:21–29.

Penuelas, J., J. Gamon, A. Freeden, J. Merino and C. Field. 1994. Reflectance indices associated with physiological changes in nitrogen- and water-limited sunflower leaves. *Remote Sensing of Environment* 48(2):135–146.

Pepe, M., L. Pompilio, B. Gioli, L. Busetto and M. Boschetti. 2020. Detection and Classification of Non-Photosynthetic Vegetation from PRISMA Hyperspectral Data in Croplands. *Remote Sensing* 12(23).

Peschel, T., M. Beier, C. Damm, J. Hartung, R. Jende, S. Muller, M. Rohde, A. Gebhardt, S. Risse, I. Walter, I. Sebastia, and D. Krutz. 2018. Integration and testing of an imaging spectrometer for earth observation. Page 7 in *Proceedings International Conference on Space Optics,* held in Chania, Greece, 12 July 2019.

Pignatti, S., N. Acito, U. Amato, R. Casa, F. Castaldi, R. Coluzzi, R. De Bonis, M. Diani, V. Imbrenda, G. Laneve, S. Matteoli, A. Palombo, S. Pascucci, F. Santini, T. Simoniello, C. Ananasso, G. Corsini and V. Cuomo. 2015. Environmental products overview of the Italian hyperspectral PRISMA mission: The SAP4PRISMA project. Page 5 in *Proceedings IEEE International Geoscience and Remote Sensing Symposium,* held in Milan, Italy. https://doi.org/10.1109/IGARSS.2015.7326701.

Pignatti, S., A. Palombo, S. Pascucci, F. Romano, F. Santini, T. Simoniello, U. Amato, V. Cuomo, N. Acito, M. Diani, S. Matteoli, G. Corsini, R. Casa, R. De Bonis, G. Laneve and C. Ananasso. 2013. The PRISMA hyperspectral mission: Science, activities and opportunities for agriculture and land monitoring. Page 5 in *Proceedings IEEE International Geoscience and Remote Sensing Symposium,* held in Melbourne, Australia. https://doi.10.1109/IGARSS.2013.6723850.

Poley, L. and G. McDermid. 2020. A systematic review of the factors influencing the estimation of vegetation aboveground biomass using unmanned aerial systems. *Remote Sensing* 12(1052):1–46.

Praveen, Y., A. Kiranmai, K. Nikitha and V. Devi. 2016. Hyperspectral sensor data fusion at decision level using support vector machine. *International Journal of Research in Engineering and Technology* 5(12):14–18.

Puletti, N., N. Camarretta and P. Corona. 2016. Evaluating EO-1 Hyperion capability for mapping conifer and broadleaved forests. *European Journal of Remote Sensing* 49(1):157–169.

R Core Team. 2018. *R: A Language and Environment for Statistical Computing.* Vienna, Austria: R Foundation for Statistical Computing.

Raczko, E. and B. Zagajewski. 2017. Comparison of support vector machine, random forest and neural network classifiers for tree species classification on airborne hyperspectral apex images. *European Journal of Remote Sensing* 50(1):144–154.

Ren, J., Wang, R., Liu, G., Feng, R., Wang, Y., and Wu, W. (2020). Partitioned relief-F method for dimensionality reduction of hyperspectral images. *Remote Sensing,* 12(1104):1–21.

Roberts, D., K. Roth, E. Wetherley, S. Meerdink and R. Perroy. 2018. Hyperspectral vegetation indices. In *Hyperspectral Remote Sensing of Vegetation,* Vol. II: Hyperspectral Indices and Image Classifications for Agriculture and Vegetation, 1–24. Boca Raton: Taylor and Francis Inc. CRC Press.

Rodriguez-Galiano, V., M. Sanchez-Castillo, M. Chica-Olma and M. Chica-Rivas. 2015. Machine learning predictive models for mineral prospectivity: An evaluation of neural networks, random forest, regression trees and support vector machines. *Ore Geology Reviews* 71:804–818.

Sacks, W., D. Deryng, J. Foley and N. Ramankutty. 2010. Crop planting dates: An analysis of global patterns. *Global Ecology and Biogeography* 19:607 - 620.

Sahadevan, A. 2021. Extraction of spatial-spectral homogeneous patches and fractional abundances for field-scale agriculture monitoring using airborne hyperspectral images. *Computers and Electronics in Agriculture* 188(106325):1–11.

Salas, E. and S. Subburayalu. 2019. Modified shape index for object-based random forest image classification of agricultural systems using airborne hyperspectral datasets. *PLoS ONE* 14(3):1–22.

Salas, E., S. Subburayalu, B. Slater, K. Zhao, B. Bhattacharya, R. Tripathy, A. Das, R. Nigam, R. Dave and P. Parekh. 2020. Mapping crop types in fragmented arable landscapes using AVIRIS-NG imagery and limited field data. *International Journal of Image and Data Fusion* 11(1):33–56.

Salem, S., H. Higa, H. Kim, H. Kobayashi, K. Oki and T. Oki. 2017. Assessment of chlorophyll-a algorithms considering different trophic statuses and optimal bands. *Sensors* 17(1746):1–24.

Surface Biology and Geology (SBG). 2022. Jet Propulsion Laboratory California Institute of Technology: Surface Biology and Geology. <https://sbg.jpl.nasa.gov/>. Accessed 17 June 2022.

Segarra, J., M. Buchaillot, J. Araus and S. Kefauver. 2020. Remote sensing for precision agriculture: Sentinel-2 improved features and applications. *Agronomy* 10(641):1–18.

Serrano, L., J. Penuelas and S. Ustin. 2002. Remote sensing of nitrogen and lignin in Mediterranean vegetation from AVIRIS data: Decomposing biochemical from structural signals. *Remote Sensing of Environment* 81:355–364.

Singh, L., O. Mutanga, P. Mafongoya, K. Peerbhay and J. Crous. 2022. Hyperspectral remote sensing for foliar nutrient detection in forestry: A near-infrared perspective. *Remote Sensing Applications: Society and Environment* 25:1–13.

Sonmez, N. and B. Slater. 2016. Measuring intensity of tillage and plant residue cover using remote sensing. *European Journal of Remote Sensing* 49(1):121–135.

Thenkabail, P. 2015. Hyperspectral remote sensing for terrestrial applications. In *Remote Sensing Handbook,* Vol. II: Land Resources: Monitoring, Modeling, and Mapping: Advances over Last 50 Years and a Vision for the Future. New York: Taylor and Francis Inc., CRC Press.

Thenkabail, P., I. Aneece, P. Teluguntla and A. Oliphant. 2021. Hyperspectral narrowband data propel gigantic leap in the earth remote sensing, highlight article. *Photogrammetric Engineering and Remote Sensing* 87(7):461–467.

Thenkabail, P., I. Aneece, P. Teluguntla, A. Oliphant, D. Foley and D. Williamson. 2019. Global Hyperspectral Imaging Spectroscopy of Agricultural-Crops & Vegetation (GHISA). <usgs.gov>

Thenkabail, P., E. Enclona, M. Ashton, C. Legg and M. De Dieu. 2004. Hyperion, IKONOS, ALI, and ETM+ sensors in the study of African rainforests. *Remote Sensing of Environment* 90:23–43.

Thenkabail, P., M. Gumma, P. Teluguntla and I. Mohammed. 2014. Hyperspectral remote sensing of vegetation and agricultural crops. *Photogrammetric Engineering and Remote Sensing* 80(4):697–709.

Thenkabail, P., G. Lyon and A. Huete. 2018a. Hyperspectral remote sensing of vegetation. In *Volume I: Fundamentals, Sensor Systems, Spectral Libraries, and Data Mining for Vegetation,* 449. New York: Taylor and Francis Inc., CRC Press.

Thenkabail, P., G. Lyon and A. Huete. 2018b. Hyperspectral remote sensing of vegetation. In *Volume II: Hyperspectral Indices and Image Classifications for Agriculture and Vegetation,* 296. New York: Taylor and Francis Inc., CRC Press,.

Thenkabail, P., G. Lyon and A. Huete. 2018c. Hyperspectral remote sensing of vegetation. In *Volume III: Biophysical and Biochemical Characterization and Plant Species Studies,* 348. New York: Taylor and Francis Inc., CRC Press,.

Thenkabail, P., G. Lyon and A. Huete. 2018d. Hyperspectral remote sensing of vegetation. In *Volume IV: Advanced Applications in Remote Sensing of Agricultural Crops and Natural Vegetation,* 386. New York: Taylor and Francis Inc., CRC Press,.

Thenkabail, P., I. Mariotto, M. Gumma, E. Middleton, D. Landis and K. Huemmrich. 2013. Selection of hyperspectral narrowbands (HNBs) and composition of hyperspectral two band vegetation indices (HVIs) for biophysical characterization and discrimination of crop types using field reflectance and Hyperion/EO-1 data. *IEEE Journal of Selected Topics in Applied Earth Observations and Remote Sensing* 6(2):427–439.

Tripathi, P. and R. Garg. 2021. Feature extraction of DESIS and PRISMA hyperspectral remote sensing datasets for geological applications. Pages 169–173 in *Proceedings ASPRS 2021 Annual Conference.* https://doi.org/10.5194/isprs-archives-XLIV-M-3-2021-169-2021.

United States Department of Agriculture National Agricultural Statistics Service (USDA NASS). 2022. 2020 California Cropland Data Layer: NASS/USDA Metadata. <https://www.nass.usda.gov/>. Accessed 09 June 2022.

United States Department of Agriculture (USDA) National Agricultural Statistics Service Cropland Data Layer. 2022. Published crop-specific data layer. <https://nassgeodata.gmu.edu/CropScape/>. Accessed 09 June 2022.

Vali, A., S. Comai and M. Matteucci. 2020. Deep learning for land use and land cover classification based on hyperspectral and multispectral Earth observation data: A review. *Remote Sensing* 12:1–31.

Vogelmann, J., B. Rock and D. Moss. 1993. Red edge spectral measurements from sugar maple leaves. *International Journal of Remote Sensing* 14(8):1563–1575.

Wang, L. and J. Qu. 2007. NMDI: A normalized multi-band drought index for monitoring soil and vegetation moisture with satellite remote sensing. *Geophysical Research Letters* 34:1–6.

Wickham, H. 2016. *Ggplot2: Elegant Graphics for Data Analysis* 2d ed. New York: Springer International Publishing.

Yang, S., L. Hu, H. Wu, H. Ren, H. Qiao, P. Li and W. Fan. 2021. Integration of crop growth model and random forest for winter wheat yield estimation from UAV hyperspectral imagery. *IEEE Journal of Selected Topics in Applied Earth Observations and Remote Sensing* 14:6253–6269.

Zarco-Tejada, P., A. Berjon, R. Lopez-Lozano, J. Miller, P. Martin, V. Cachorro, M. Gonzalez and A. de Frutos. 2005. Assessing vineyard condition with hyperspectral indices: Leaf and canopy reflectance simulation in a row-structured discontinuous canopy. *Remote Sensing of Environment* 99:271–287.

Zarco-Tejada, P., J. Pushnik, S. Dobrowski and S. Ustin. 2003. Steady-state chlorophyll a fluorescence detection from canopy derivative reflectance and double-peak red-edge effects. *Remote Sensing of Environment* 84(2):283–294.

Zhang, C., L. Di, P. Hao, Z. Yang, L. Lin, H. Zhao and L. Guo. 2021a. Rapid in-season mapping of corn and soybeans using machine-learned trusted pixels from Cropland Data Layer. *International Journal of Applied Earth Observation and Geoinformation* 102:1–14.

Zhang, W., X. Li and L. Zhao. 2018. Band priority index: A feature selection framework for hyperspectral imagery. *Remote Sensing* 10(1095):1–19.

Zhang, Y., C. Xia, X. Zhang, X. Cheng, G. Feng, Y. Wang and Q. Gao. 2021b. Estimating the maize biomass by crop height and narrowband vegetation indices derived from UAV-based hyperspectral images. *Ecological Indicators* 129:1–12.

Zhong, L., P. Gong and G. Biging. 2014. Efficient corn and soybean mapping with temporal extendability: A multi-year experiment using Landsat imagery. *Remote Sensing of Environment* 140:1–13.

SUSTAININGMEMBERS

ACI USA Inc.
Weston, Florida
https://acicorporation.com/
Member Since: 2/2018

Aerial Services, Inc.
Cedar Falls, Iowa
www.AerialServicesInc.com
Member Since: 5/2001

Airworks Solutions Inc.
Boston, Massachusetts
Member Since: 3/2022

Applanix
Richmond Hill, Ontario, Canada
http://www.applanix.com
Member Since: 7/1997

Ayres Associates
Madison, Wisconsin
www.AyresAssociates.com
Member Since: 1/1953

CT Consultants
Mentor, Ohio
Member Since: 3/2022

Dewberry
Fairfax, Virginia
www.dewberry.com
Member Since: 1/1985

Esri
Redlands, California
www.esri.com
Member Since: 1/1987

GeoCue Group
Madison, Alabama
http://www.geocue.com
Member Since: 10/2003

Geographic Imperatives LLC
Centennial, Colorado
Member Since: 12/2020

GeoWing Mapping, Inc.
Richmond, California
www.geowingmapping.com
Member Since: 12/2016

Halff Associates, Inc.
Richardson, Texas
www.halff.com
Member Since: 8/2021

Keystone Aerial Surveys, Inc.
Philadelphia, Pennsylvania
www.kasurveys.com
Member Since: 1/1985

Kucera International
Willoughby, Ohio
www.kucerainternational.com
Member Since: 1/1992

L3Harris Technologies
Broomfield, Colorado
www.l3harris.com
Member Since: 6/2008

Merrick & Company
Greenwood Village, Colorado
www.merrick.com/gis
Member Since: 4/1995

Nearmap
South Jordan, Utah
www.nearmap.com
Member Since: 6/2023

NV5 Geospatial
Sheboygan Falls, Wisconsin
www.quantumspatial.com
Member Since: 1/1974

Pickett and Associates, Inc.
Bartow, Florida
www.pickettusa.com
Member Since: 4/2007

Riegl USA, Inc.
Orlando, Florida
www.rieglusa.com
Member Since: 11/2004

Robinson Aerial Surveys, Inc.(RAS)
Hackettstown, New Jersey
www.robinsonaerial.com
Member Since: 1/1954

Sanborn Map Company
Colorado Springs, Colorado
www.sanborn.com
Member Since: 10/1984

Surdex Corporation
Chesterfield, Missouri
www.surdex.com
Member Since: 12/2011

Surveying And Mapping, LLC (SAM)
Austin, Texas
www.sam.biz
Member Since: 12/2005

T3 Global Strategies, Inc.
Bridgeville, Pennsylvania
https://t3gs.com/
Member Since: 6/2020

Terra Remote Sensing (USA) Inc.
Bellevue, Washington
www.terraremote.com
Member Since: 11/2016

Towill, Inc.
San Francisco, California
www.towill.com
Member Since: 1/1952

Woolpert LLP
Dayton, Ohio
www.woolpert.com
Member Since: 1/1985

SUSTAININGMEMBERBENEFITS

Membership

✓ Provides a means for dissemination of new information

✓ Encourages an exchange of ideas and communication

✓ Offers prime exposure for companies

Benefits of an ASPRS Membership

- Complimentary and discounted Employee Membership*

- E-mail blast to full ASPRS membership*

- Professional Certification Application fee discount for any employee

- Member price for ASPRS publications

- Discount on group registration to ASPRS virtual conferences

- Sustaining Member company listing in ASPRS directory/website

- Hot link to company website from Sustaining Member company listing page on ASPRS website

- Press Release Priority Listing in *PE&RS* Industry News

- Priority publishing of Highlight Articles in *PE&RS* plus, 20% discount off cover fee

- Discount on *PE&RS* advertising

- Exhibit discounts at ASPRS sponsored conferences (exception ASPRS/ILMF)

- Free training webinar registrations per year*

- Discount on additional training webinar registrations for employees

- Discount for each new SMC member brought on board (Discount for first year only)

Foreground-Aware Refinement Network for Building Extraction from Remote Sensing Images

Zhang Yan, Wang Xiangyu, Zhang Zhongwei, Sun Yemei, and Liu Shudong

Abstract

To extract buildings accurately, we propose a foreground-aware refinement network for building extraction. In particular, in order to reduce the false positive of buildings, we design the foreground-aware module using the attention gate block, which effectively suppresses the features of nonbuilding and enhances the sensitivity of the model to buildings. In addition, we introduce the reverse attention mechanism in the detail refinement module. Specifically, this module guides the network to learn to supplement the missing details of the buildings by erasing the currently predicted regions of buildings and achieves more accurate and complete building extraction. To further optimize the network, we design hybrid loss, which combines BCE loss and SSIM loss, to supervise network learning from both pixel and structure layers. Experimental results demonstrate the superiority of our network over state-of-the-art methods in terms of both quantitative metrics and visual quality.

Introduction

Building extraction aims to localize and segment the buildings in the remote sensing image. Specifically, it divides the image pixels into the foreground and background, that is, buildings and nonbuildings. Building extraction from remote sensing images plays an important role in the fields of urban planning, population estimation, land utilization analysis, building change detection, and so on. Recently, with the rapid development of deep learning methods and remote sensing technologies, significant progress has been made in building extraction.

The existing building extraction methods are divided mainly into two groups: traditional and deep learning–based methods. Traditional methods mainly rely on the handcrafted low-level features and heuristic priors, such as color (Sirmacek and Unsalan 2008), shadow (Ngo *et al.* 2016), shape (Zhang *et al.* 2017), edge (Ferraioli 2009), texture (Awrangjeb *et al.* 2011), and spectrum (Zhong *et al.* 2008). However, these features not only require prior professional knowledge but also are easily affected by sensors, imaging conditions, and position changes, which may limit their generalizability in different scenarios.

In recent years, the convolutional neural network (CNN) has boosted the development of computer vision tasks, such as object detection (Tian *et al.* 2019; Yang *et al.* 2019), saliency detection (Qin *et al.* 2019; Chen, Tan, *et al.* 2020; Chen, Xu, *et al.* 2020), semantic segmentation (Oktay *et al.* 2018; Huang *et al.* 2020; Zheng *et al.* 2020), building extraction, and building change detection. Compared to the traditional method, CNN has successfully broken the limits of traditional handcrafted features and has made remarkable achievements with its powerful feature extraction and presentation ability. Especially, the fully convolutional neural network (FCN) (Long *et al.* 2015) has attracted increasing interest in pixel-level dense estimation tasks, such as semantic segmentation, saliency detection, and building extraction. Compared with the original CNN, FCN not only supports dense estimates but also enables end-to-end training. Although existing networks have improved the accuracy, the complexity of remote sensing images still leads to some problems in building extraction.

On the one hand, the background of remote sensing image is complex, and the scale of buildings is different, which makes it difficult to extract buildings accurately. To resolve this problem, most of the algorithms use multi-cascade methods to extract targets. However, these approaches may introduce noise from the background remaining in the shallower layer, resulting in the over-segmentation of buildings. This leads to the first question: how to suppress noisy information while improving the sensitivity of the model to the foreground buildings so as to reduce the false positives of buildings.

On the other hand, the response values of different regions of remote sensing images are different. Most existing networks tend to learn regions that have high response values and ignore regions with low response values, which makes it difficult to capture complete information about building boundaries and building regions. Hence, the second question is how to enhance detailed information in order to make the building extraction results more complete.

To address the above problems, we propose a novel foreground-aware refinement network for building extraction called FAR-Net, which achieves accurate building extraction with high-quality boundaries.

The main contributions of this work are the following:
- We propose a foreground-aware refinement network for more accurate building extraction. Extensive experiments demonstrate that the proposed method achieves state-of-the-art results on both WHU and Inria data sets.
- We propose the foreground-aware module to improve the sensitivity of the network to the foreground pixel. It is composed of attention gate blocks, which allow our network to select the spatial features by the gating signal and further suppress background information in nonbuilding regions. Through this module, the network enhances the sensitivity of the building and reduces the false positive of buildings.
- We design the detail refinement module to guide network learning based on the reverse attention mechanism. This module focuses on the undetected regions and aggregates more detailed features, which leads to higher completeness and accuracy of the details of building boundaries and regions.

Related Work

Traditional methods rely on handcrafted features, which require experienced professionals and a large number of material resources. The emergence of deep learning achieves automatic extraction and learning

Zhang Yan is with the School of Computer and Information Engineering, Tianjin Chengjian University, Tianjin, China, and the Tianjin Intelligent Elderly Care and Health Service Engineering Research Center, Tianjin, China.

Wang Xiangyu, Zhang Zhongwei, and Sun Yemei are with the School of Computer and Information Engineering, Tianjin Chengjian University, Tianjin, China.

Liu Shudong is with the School of Computer and Information Engineering, Tianjin Chengjian University, Tianjin, China, and the Tianjin Intelligent Elderly Care and Health Service Engineering Research Center, Tianjin, China.

Corresponding author: Zhang Zhongwei (gucaszzw@163.com)

features, which is the deficiency of traditional methods and promotes the research progress of building extraction.

Recently, many building extraction methods based on FCN have been proposed. Maggiori *et al.* (2016) proposed a solid framework for remote sensing image classification. Liu, Liu, *et al.* (2019) proposed a novel spatial residual inception network (SRI-Net) to extract and fuse multi-scale contexts for building extraction by integrating multi-level features progressively. Consequently, the network can detect large buildings accurately and retain global morphological characteristics and local details. Liu, Luo, *et al.* (2019) proposed a deep encoding network (DE-Net) to mitigate information loss and enhance building distinction. Although important advances have been achieved by the above building extraction methods, they generally have incomplete or inaccurate boundary shortcomings. To mitigate this problem, Jin *et al.* (2021) proposed the boundary-aware refined network (BARNet) based on U-Net and DeepLab-v3+ for better global extraction results. He and Jiang (2021) proposed a boundary-assisted learning method that fully utilizes the boundary information of buildings and ameliorates the boundary maintenance of buildings. Deng *et al.* (2021) proposed an encoder-decoder architecture to extract buildings automatically by introducing the attention gate mechanism. We can see that these networks enhance the feature extraction by adding boundary learning and the attention mechanism. In addition, in the field of saliency object detection, Chen, Tan, *et al.* (2020) designed a novel reverse attention block for guiding the whole network to sequentially discover complement object regions and details by erasing the current predicted regions from a side-output feature. Thus, we introduce attention gate blocks to increase the sensitivity of the model to buildings and utilize the reverse attention mechanism to enhance the extraction of detailed feature.

The above methods based on FCN focus on existing backbone networks, such as Alexnet (Krizhevsky *et al.* 2017), VGG (Simonyan and Zisserman 2014), ResNet (He *et al.* 2016), ResNeXt (Xie *et al.* 2017), and DenseNet (Huang *et al.* 2017). Nevertheless, these networks are unable to extract the features of local details and global contrast information effectively. To address this problem, these methods aggregate the multi-scale features by introducing additional feature aggregation modules. However, it will increase the complexity of the network.

U-Net (Ronneberger *et al.* 2015), as a classical variant of FCN, did not use any existing backbone network and achieved multi-scale features extraction and fusion. Therefore, U-Net is extended to similar fields, such as saliency detection and building extraction. Wu *et al.* (2018) proposed a multi-constraint fully convolutional network (MC-FCN) for end-to-end building segmentation. Ji *et al.* (2019) proposed a Siamese U-Net with shared weights in two branches that improves the segmentation accuracy, especially for large buildings. Because of the complexity and scale variability of remote sensing images, the single U-Net is not enough to extract enough feature information. Therefore, the stacking of multiple U-Net–like structures has been applied in complex natural image segmentation (Shah *et al.* 2018), pose estimation (Newell *et al.* 2016; Ma *et al.* 2018; Tang *et al.* 2018), remote sensing image segmentation (Ghosh *et al.* 2018), and so on.

In the above methods, cascaded models are built by stacking multiple structures similar to U-Net sequentially. Although they extract more enriched features, they increase computation and memory cost. To address this issue, Qin *et al.* (2020) designed a nested network, called U2-Net, for salient object detection.

Compared to the usual cascade model, U2-Net is simpler and more efficient. Furthermore, it allows the network to go deeper to capture multi-scale local and global features while maintaining high resolution. Meanwhile, high resolution is the characteristic of remote sensing images, and it also plays a crucial part in building extraction. Inspired by U2-Net, aiming at the characteristics of high-resolution remote sensing images and the problems of building extraction, we propose the network FAR-Net, which is explained next.

Network Architecture

The proposed FAR-Net consists of the feature extraction module (FEM), the foreground-aware module (FAM), and the detail refinement module (DRM), as illustrated in Figure 1. First, the input image is fed to the FEM to extract multi-scale features. Next, the FAM is designed to suppress the background noise of shallow-layer features and strengthen the building recognition. Finally, we develop the DRM to further refine the detail and generate the final result.

FEM

The FEM is used to extract rich multi-scale features from the input image. As shown in Figure 1, we use nested U-shaped structure, which is composed mainly of the encoder and decoder. In the encoder stages, the input of current stage is down-sampled from the output of the previous stage. Similarly, in the decoder stages, the input of current stage is up-sampled from the output of the previous stage. Hence, the structure allows the network to go deeper and attain high resolution without significantly increasing the memory and computation cost. Through this module, our network locates buildings accurately, especially in building boundaries and small buildings.

To implement the encoder $E_i(i = 1 \sim 6)$ and decoder $D_i(i = 1 \sim 5)$, we designed residual U-blocks RSU_L and RSU_{4F}, as shown in Figure 2. The encoder consists of 6 stages, in the encoder $E_i(i = 1 \sim 4)$ stages, we use the residual U-blocks RSU_L ($L = 8 - i$), respectively. RSU_L consists of the convolution layer, the encoder-decoder structure (where the number of encoder layers is L), and a residual connection, as shown in Figure
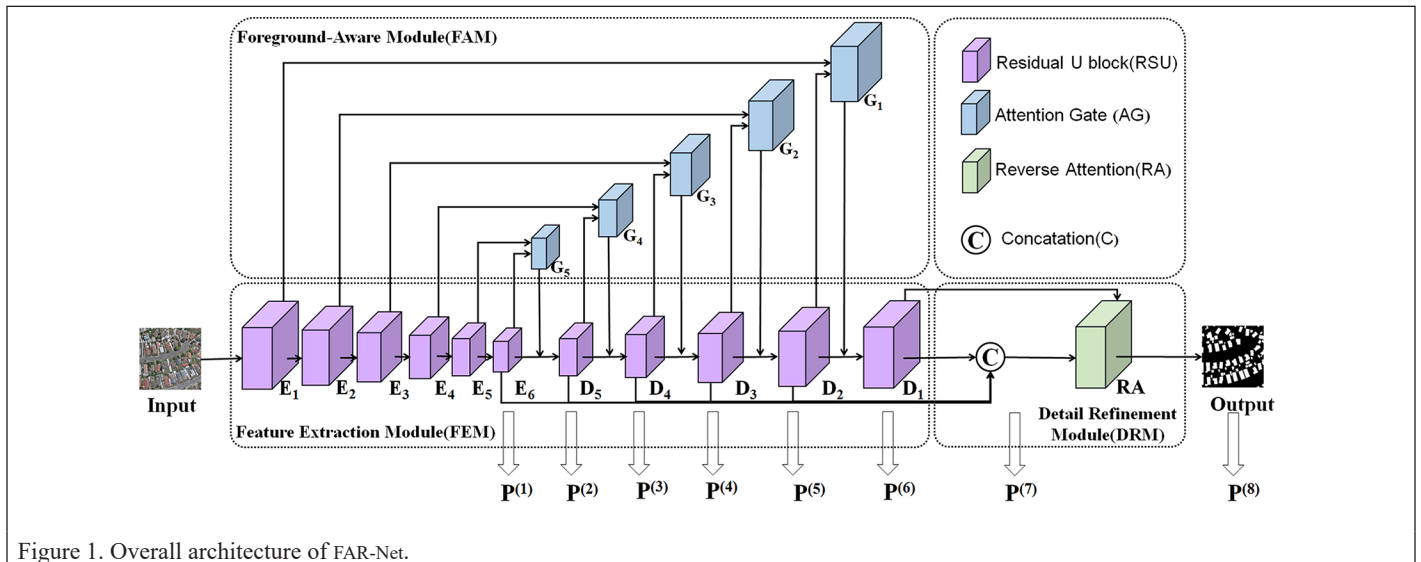

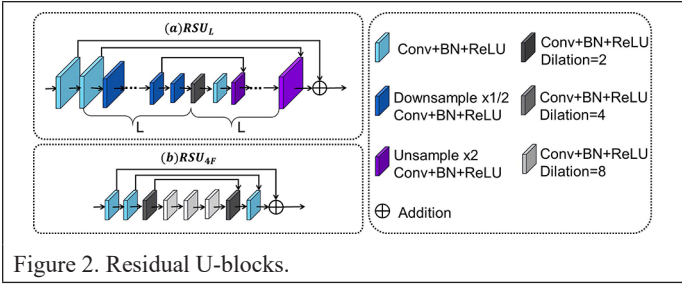Figure 1. Overall architecture of FAR-Net.

Figure 2. Residual U-blocks.

2a. However, in the encoder $E_i (i = 5, 6)$ stages, the resolution of feature maps is relatively low, and useful context will be lost by further downsampling of these feature maps. In view of the above, for E_5 and E_6 stages, we design RSU_{4F} with dilated convolutions and replace the downsampling and up-sampling operations in RSU_{4F}, as seen in Figure 2b. Among them, the dilated rates of the dilated convolutions are 2, 4, and 8, respectively. Each of these convolution layers is followed by a batch normalization and a ReLU activation function. Thus, the resolution of each intermediate feature map of RSU_{4F} is consistent with their input feature map. The combined use of RSU_L and RSU_{4F} balances memory consumption and resolution. The decoder consists of five stages and has a similar structure with respect to the E_6 symmetry of the encoder. We also use the RSU_{4F} in D_5, similar to the encoder stages E_5 and E_6.

FAM

In general, fine feature maps contain abundant local spatial information, which is helpful to refine and enrich the structure of buildings, but have more background noise. Coarse feature maps contain context information and have less noise, which is helpful to locate buildings. Fusing the coarse feature map and fine feature map would simply introduce background noise from the fine map, resulting in false positives of buildings. Therefore, in order to reduce false positives, we propose the FAM. The module consists of five attention gate blocks, as seen in Figure 3.
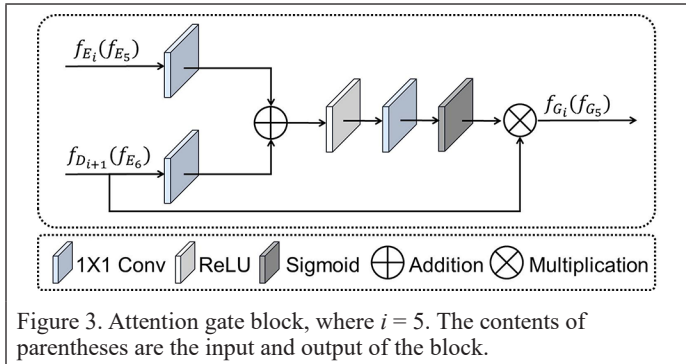

Figure 3. Attention gate block, where $i = 5$. The contents of parentheses are the input and output of the block.

In the attention gate blocks, the context information in the coarse feature map is used as the gating to select the features of the fine feature map. Through the selective fusion of features, this module can suppress the background noise and obtain more discriminative building-related features. It also allows the model to focus on the buildings automatically without additional supervision. The output f_{G_i} of FAM is defined as

$$f_{G_i} = \begin{cases} f_{D_{i+1}} \times \left(\delta \left(conv \left(ReLU \left(conv \left(f_{E_i} \right) + conv \left(f_{D_{i+1}} \right) \right) \right) \right) \right), i = 1 \sim 4 \\ f_{E_6} \times \left(\delta \left(conv \left(ReLU \left(conv \left(f_{E_5} \right) + conv \left(f_{E_6} \right) \right) \right) \right) \right), i = 5 \end{cases} \quad (1)$$

$$f_{E_i} = \begin{cases} RSU_{8-i}(RGB), i = 1 \\ RSU_{8-i}\left(f_{E_{i-1}} \right), i = 2 \sim 4 \\ RSU_{4F}\left(f_{E_{i-1}} \right), i = 5, 6 \end{cases} \quad (2)$$

$$f_{D_i} = \begin{cases} RSU_{8-i}\left(cat\left(f_{D_{i+1}}, f_{G_i} \right) \right), i = 1 \sim 4 \\ RSU_{4F}\left(cat\left(f_{E_6}, f_{G_i} \right) \right), i = 5 \end{cases} \quad (3)$$

where f_{D_i} denotes the output of the ith decoder; f_{E_i} denotes the output of the ith encoder; $conv$, $ReLU$, and δ denote convolution, rectified linear unit, and sigmoid function, respectively; $cat(*)$ denotes concatenation operation; and RGB denotes the input.

DRM

To obtain more complete features of building regions and boundaries, we design a novel DRM to further guide the network to learn the details. Specifically, the DRM employs a reverse attention mechanism, as shown in Figure 4. First, we obtain reverse attention weight from the currently predicted building regions. Then the features of the side output are selected by utilizing the weight. Thus, the missing regions and details of buildings can be learned from the remaining regions efficiently.
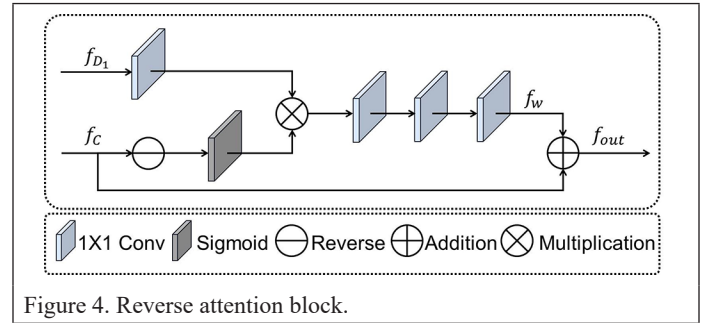
Figure 4. Reverse attention block.

Given the currently predicted building regions, reverse attention weight A can be expressed as

$$A = \delta(Rev(f_C)) \quad (4)$$

where $f_C = conv(cat(f_{E_6}, f_{D_5}, f_{D_4}, f_{D_3}, f_{D_2}, f_{D_1}))$ and $Rev(*)$ denotes a reverse operation. Each feature map is up-sampled to the same size as the input feature map for concatenation operation $cat(*)$, and then a 1×1 convolution operation is performed.

According to the reverse attention weight A and the side-output feature f_{D_1}, the weighted convolutional output f_W can be expressed as

$$f_W = conv(conv(conv(A \times conv(f_{D_1})))) \quad (5)$$

The final output f_{Out} can be expressed as

$$f_{Out} = f_W + f_C \quad (6)$$

Loss Function

We design the hybrid loss L for optimizing segmentation of regions and boundaries. Combining the binary cross entropy (BCE) loss function and the structure similarity (SSIM) loss function, the training of the model is supervised from the two levels of pixel and image structure. On the one hand, the model pays attention to the accuracy of single-pixel prediction; on the other hand, it combines the structure information to get more comprehensive and accurate extraction results. The loss function is used for training the whole network model iteratively to guide the convergence of the whole process. The loss function L can be expressed as

$$L = \sum_{k=1}^{K} \left(l_{bce}^{(k)} + l_{ssim}^{(k)} \right) \tag{7}$$

where $l_{bce}^{(k)}$ and $l_{ssim}^{(k)}$ denote BCE loss and SSIM loss, respectively, and K denotes the total number of the outputs, that is, $K = 8$. Our building extraction model is deeply supervised with eight outputs $P^{(k)}$, as shown in Figure 1.

In building extraction, BCE loss is the most widely used to measure the relation between the predicted building extraction map and the ground truth (De Boer *et al.* 2005). It is defined as

$$l_{bce} = -\sum_{(r,c)} \Big[G(r,c) \log \big(P(r,c) \big) + \big(1 - G(r,c) \big) \log \big(1 - P(r,c) \big) \Big] \tag{8}$$

where $G(r,c) \in \{0,1\}$ is the ground-truth label of the pixel (r,c) and $P(r,c)$ is the predicted probability of being building.

BCE loss is helpful to accelerate the convergence of the model, but it does not consider neighborhood information. SSIM loss considers neighborhood information and gives a higher weight to the boundary (Wang *et al.* 2003). Let $x = \{x_j: j = 1,\ldots, N^2\}$ and $y = \{y_j: j = 1,\ldots, N^2\}$, where x and y are the pixel values of two corresponding patches ($N \times N$) cropped from the predicted map P and the ground truth G, respectively. The SSIM of x and y is defined as

$$l_{ssim} = 1 - \frac{\left(2\mu_x\mu_y + C_1 \right)\left(2\sigma_{xy} + C_2 \right)}{\left(\mu_x^2 + \mu_y^2 + C_1 \right)\left(\sigma_x^2 + \sigma_y^2 + C_2 \right)} \tag{9}$$

where μ_x, μ_y and σ_x, σ_y are the mean and standard deviations of x and y, respectively; σ_{xy} is their covariance; and $C_1 = 0.0001$ and $C_2 = 0.0009$ are used to keep the denominator from being zero.

Experiments and Results

In this section, we state the implementation details, data sets, and evaluation metrics used in our experiments. To verify the validity of key modules, we do a set of ablation experiments to analyze the learning behavior of FAR-Net in step. To illustrate the overall performance of FAR-Net, we conduct performance comparisons with state-of-the-art methods. In addition, visual analysis of experimental results is shown to further prove the robustness of FAR-Net.

Implementation Details

The original images of 512×512 pixels are first rescaled to 320×320 pixels and random cropped to 228×228 pixels during training. The size of the results is restored to the original size (512×512) by using bilinear interpolation. Finally, we train 300 epochs, among which the batch size is set to 12, and the whole training process takes about 75 hours. Any existing backbones are not used in our network. Hence, we train the network from scratch without pretraining and use Xavier to initialize all the convolutional layers. Adam is used to train networks, and its hyperparameters are set to default, where $lr = 1e-3$, *betas* = (0.9, 0.999), *eps* = $1e-3$, and *weightdecay* = 0.

We implement our network based on the publicly available framework Pytorch 0.4.0. We train and test our models on Ubuntu20.04 with an Intel Xeon Gold 6154 CPU (128 GB RAM) and an NVIDIA Tesla V100 (32 GB memory).

Data Sets

We evaluate our methods on the following two open-source building data sets:
- The WHU Aerial Building Dataset was created by Ji *et al.* (2019). It contains more than 22 000 independent buildings. It is seamlessly cropped into 8189 tiles with 512×512 pixels. It is divided into the training set, the validation set, and the testing set with 4736, 1036, and 2416 tiles, respectively.
- The Inria Aerial Image Labeling Dataset was created by Maggiori *et al.* (2017). It involves aerial images of 10 cities around the world. Since only the ground-truth images of the training set are public, we selected the first five images from 36 images in each city as the test

set and the rest as the training set. Aerial image tiles (5000×5000) are seamlessly cropped to 512×512.

Evaluation Metrics

To assess the accuracy of the results comprehensively, four metrics—intersection over union (*IoU*), precision (*P*), recall (*R*), and F_1—are used during the whole experiment. They are expressed, respectively, as

$$IoU = TP/(TP + FN + FP) \tag{10}$$

$$P = TP/(TP + FP) \tag{11}$$

$$R = TP/(TP + FN) \tag{12}$$

$$F_1 = (2 \times P \times R)/(P + R) \tag{13}$$

where *TP*, *FP*, and *FN* denote the true positive, false positive, and false negative, respectively.

Ablation Study

As discussed in the section "Network Architecture," our FAR-Net contains two main components: the FAM and the DRM. To verify the effectiveness of these modules, we conduct the ablation experiments on the WHU and the Inria data sets and provide the quantitative results of different models in Table 1 (the best entries are in bold), where baseline preserves the FEM solely.

Table 1. Ablation study.[a]

	Architecture			Evaluation Metrics				Parameter
	Baseline	FAM	DRM	IoU	Precision	Recall	F_1	(M)
WHU	√			0.965	0.982	0.958	0.970	44.01
	√	√		0.971	0.985	**0.963**	**0.974**	44.63
	√	√	√	**0.974**	**0.986**	0.962	**0.974**	44.63
Inria	√			0.835	0.906	0.813	0.824	
	√	√		0.864	0.923	**0.893**	**0.907**	
	√	√	√	**0.871**	**0.927**	0.822	0.871	

[a]FAM = foreground-aware module; DRM = detail refinement module; IoU = intersection over union.

As shown in Table 1, on the WHU data sets, FAM brings performance improvement; that is, IoU is improved by 0.6%; precision is boosted by 0.3%; recall and F1 are improved by 0.5% and 0.4%, respectively; and parameter is increased 0.62M. Then the DRM is introduced, which contributes 0.3% in terms of IoU and 0.1% in terms of precision based on FAM. Although recall decreased by 0.1%, it improves the accuracy of building extraction and adds only a few parameters. On the Inria data sets, similar results are obtained. Hence, compared with other models, FAR-Net achieves the better performance, that is improves by 0.9% in terms of IoU against the baseline model and 0.4% in terms of precision. In addition, the both recall and F1 are improved by 0.4%. This demonstrates that our proposed FAR-Net achieves good performance.

The visualization of the ablation experiments on the WHU data set is shown in Figure 5. As seen the ellipse area of column c, there are building false positives due to the interference of nonbuilding targets, such as cars. After adding the FAM, as shown in column d, the false positive is significantly reduced in the corresponding regions. However, rectangle areas of column d still have incomplete building regions and blurred boundaries. On this basis, comparing columns e and d, although the recall is down by 0.1%, the problems existing in column d are significantly improved by adding a DRM, as seen in column e.

In order to better show the training process, we plotted the line graph shown in Figure 6 based on the loss values obtained from the first 300 epochs, where the abscissa is the number of epochs and the ordinate is the value of the overall loss function. The solid line is the model convergence curve on the WHU data set, and the dotted line is the model convergence curve on the Inria data set. It can be seen from Figure 6 that as the epoch approaches 300, both curves tend to
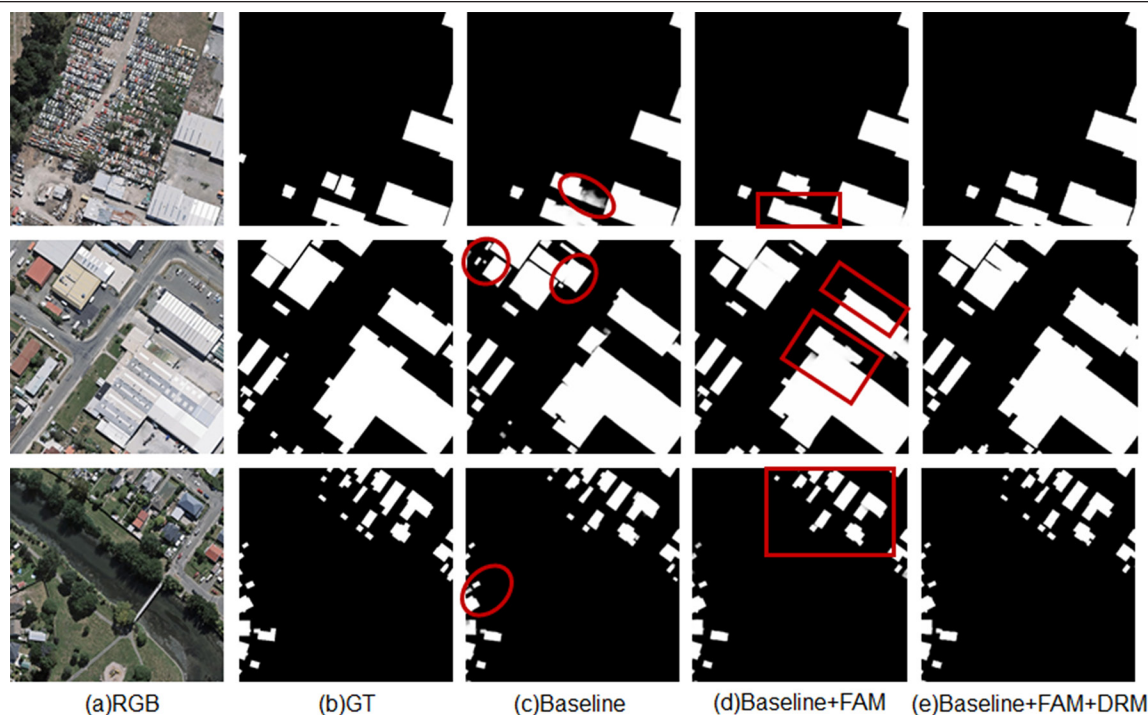
Figure 5. Visualization of the ablation experiments on the WHU data set, where the ellipse indicates the false positive of buildings and the rectangle indicates that the detail information is inaccurate.
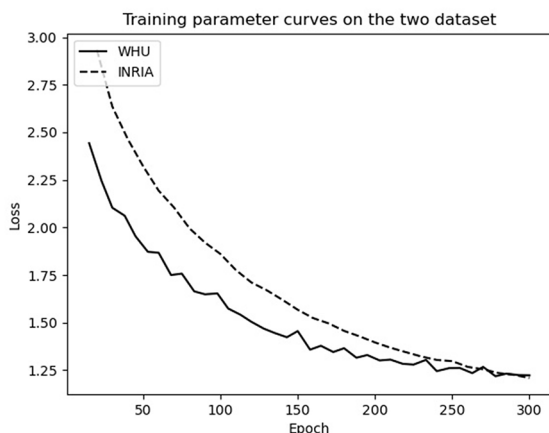
Figure 6. Training parameter curves on two data sets.

converge. In addition, the confusion matrix of the classification results is shown in Figure 7.

Performance Comparison with State-of-the-Art Methods

Quantitative Comparison
To further investigate the performance, FAR-Net is compared with 10 state-of-the-art methods on the WHU data set, including U-Net (Ronneberger *et al.* 2015), SegNet (Badrinarayanan *et al.* 2017), RefineNet (Lin *et al.* 2017), DeeplabV3+ (Chen *et al.* 2018), SRI-Net (Liu, Liu, *et al.* 2019), MC-FCN (Wu *et al.* 2018), SiU-Net (Ji *et al.* 2019), DE-Net (Liu, Luo, *et al.* 2019), BARNet (Jin *et al.* 2021), and BAL (He and Jiang 2021). The U-Net and SegNet are two typical architectures with elegant encoder-decoder structures for image segmentation. RefineNet is a multipath refinement network. DeepLabv3+ introduces the idea of encoder-decoder based on DilatedFCN. In addition, SRI-Net, MC-FCN, SiU-Net, DE-Net, BARNet, and BAL are all based on FCN for building extraction. For fair comparison, the performance data of
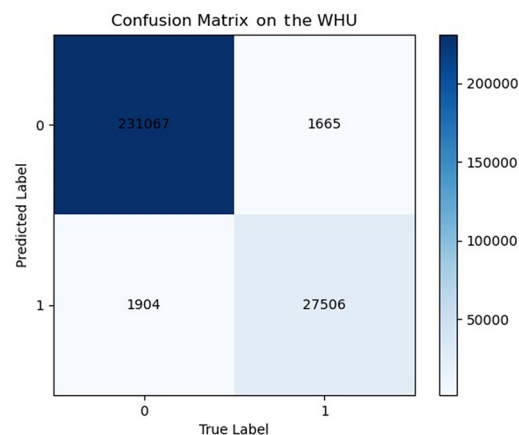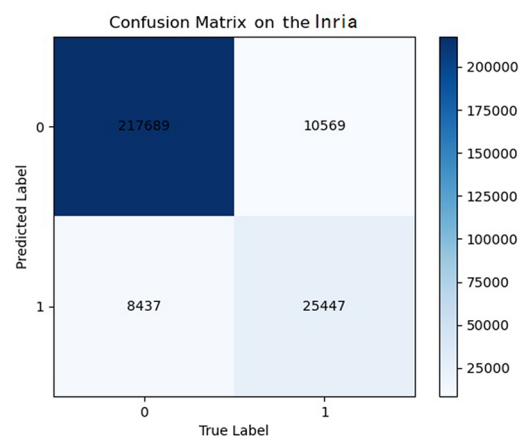
Figure 7. Confusion matrix on the two data sets.

different methods are provided directly by the author or obtained by running the provided program.

The results of different methods are shown in Table 2, where the best entries are in bold. As can be seen from the Table 2, among the comparison algorithms, BARNet has the best performance. Compared with BARNet, our method improves 5.9%, 1.4%, and 0.9% in terms of IoU, precision, and recall, respectively. It is obvious that our method has the best performance.

Furthermore, FAR-Net is compared with six state-of-the-art methods on the Inria data sets. The results of different methods are listed in Table 3, where the best entries are in bold. As shown in Table 3, BAL has the highest recall. Compared with BAL, the recall of our method decreased by 8.9%, but the IoU and precision improved by 9.9% and 9.2%, respectively. IoU and precision of FAR-Net are the highest, while precision and recall are better balanced.

Quantitative Comparison

For subjective visual evaluation, we show details of the visual examples, as shown in Figure 8. As seen in the rectangle marker region in Figure 8a–c, for large buildings, SegNet, U-Net, and RefineNet have obvious drawbacks with region incompleteness and boundary error. Although DeeplabV3+ and SRI-Net can roughly detect regions and outlines of the buildings, the two models still have boundary distortion. By contrast, the regions and boundaries of the building are detected accurately and completely by our FAR-Net. As shown in the ellipse regions in Figure 8d–e, for small buildings, SegNet, U-Net, RefineNet, and DeepLabv3 + have false positive. SRI-Net and our method have fewer false positives of buildings and more accurate boundaries. The results show that FAR-Net can deal with different scenarios that have complex backgrounds and multi-scale buildings and so on. Compared with these methods, FAR-Net is more robust for building extraction, and the building maps generated by our approach are more accurate.

Visual Analysis of Experimental Results

Moreover, our FAR-Net successfully copes with simple noninterference scenarios and complex scenarios, as shown in Figure 9. For simple noninterference scenarios, the method can accurately extract buildings of different sizes and shapes, as shown in Figure 9a. And for complex scenarios where there are cars and other interfering targets, our method still gets more accurate results, as shown in Figure 9b. This indicates that FAR-Net extracts more accurate features of buildings, thus obtaining a finer result.

Table 2. Performance comparison on the WHU data set.[a]

Method	IoU	Precision	Recall	F_1
U-Net	0.868	0.914	0.945	0.929
SegNet	0.856	0.921	0.899	0.910
RefineNet	0.869	0.937	0.923	0.930
DeeplabV3+	0.873	0.943	0.922	0.932
MC-FCN	0.871	0.946	0.917	0.931
SiU-Net	0.884	0.938	0.939	0.938
SRI-Net	0.891	0.952	0.933	0.942
DE-Net	0.904	0.952	0.948	0.950
BARNet	0.915	0.972	0.953	0.962
BAL	0.905	0.951	0.949	0.950
FAR-Net	**0.974**	**0.986**	**0.962**	**0.974**

[a]IoU = intersection over union; MC-FCN = multi-constraint fully convolutional network; SRI-Net = spatial residual inception network; DE-Net = deep encoding network; BARNet = boundary-aware refined network.

Table 3. Performance comparison on the Inria data set.[a]

Method	IoU	Precision	Recall	F_1
U-Net	0.697	0.831	0.811	0.821
SegNet	0.632	0.796	0.754	0.774
RefineNet	0.701	0.864	0.803	0.827
DeeplabV3+	0.711	0.849	0.813	0.831
SRI-Net	0.697	0.858	0.815	0.836
BAL	0.772	0.835	**0.911**	**0.871**
FAR-Net	**0.871**	**0.927**	0.822	**0.871**

[a]IoU = intersection over union; SRI-Net = spatial residual inception network.

Figure 8. Visual results by different methods on the WHU data set, where the ellipse indicates the false positive of buildings and the rectangle indicates that the detail information is inaccurate.
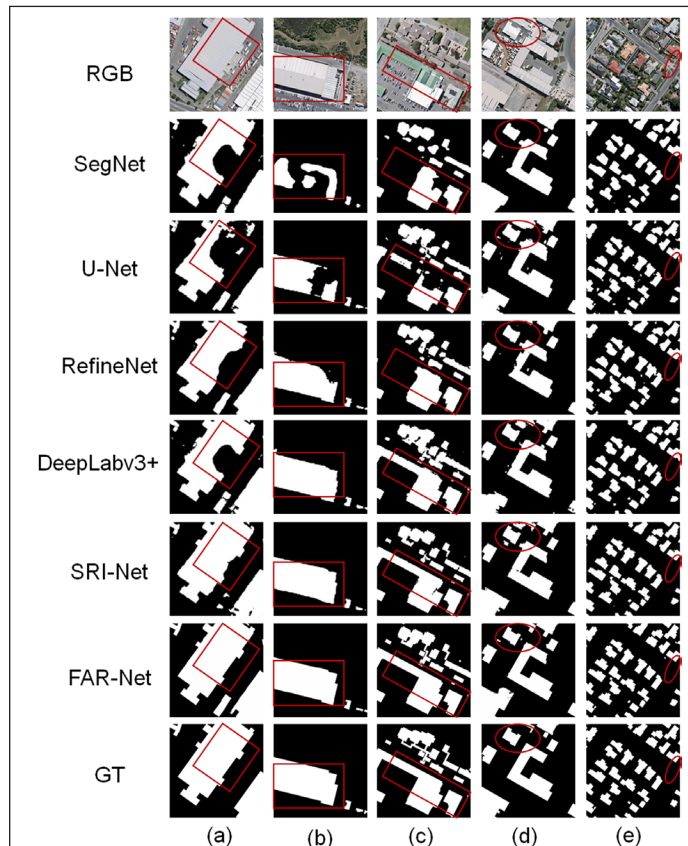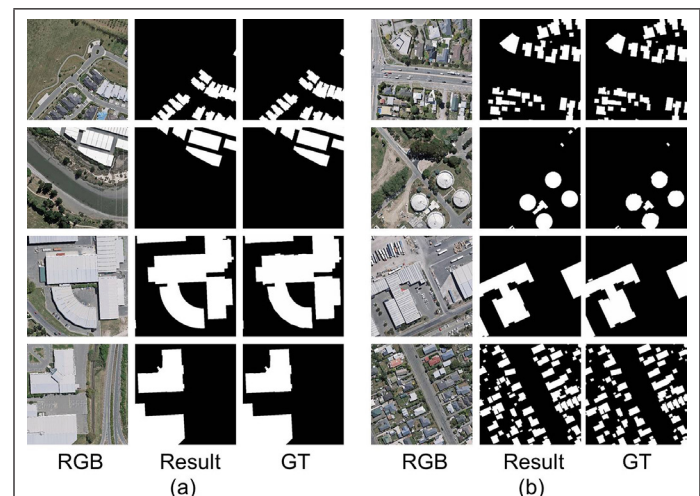

Figure 9. Visual analysis of experimental results on the WHU data set.

Conclusions

This article concentrates on building extraction in remote sensing images and proposes an end-to-end model FAR-Net. Benefiting from the attention gate of the FAM, our FAR-Net learns to focus on buildings by suppressing the noise of the background. It can reduce the false positive of buildings, and improve the accuracy of building extraction effectively. Moreover, we design the DRM to make the network learn missing building regions and details. Extensive experiments on the WHU and Inria data sets show the effectiveness of the proposed method in terms of quantitative and visual results.

Acknowledgments

References

Awrangjeb, M., C. Zhang and C. S. Fraser. 2011. Improved building detection using texture information. *International Archives of Photogrammetry, Remote Sensing and Spatial Information Sciences* 38:143–148.

Badrinarayanan, V., A. Kendall and R. Cipolla. 2017. Segnet: A deep convolutional encoder-decoder architecture for image segmentation. *IEEE Transactions on Pattern Analysis and Machine Intelligence* 39(12):2481–2495.

Chen, L. C., Y. Zhu, G. Papandreou, F. Schroff and H. Adam. 2018. Encoder-decoder with atrous separable convolution for semantic image segmentation. Pages 801–818 in *Proceedings of the European Conference on Computer Vision*, held in Munich, Germany, 8-14 September 2018. Berlin, Germany: Springer.

Chen, S., X. Tan, B. Wang, H. Lu, X. Hu and Y. Fu. 2020. Reverse attention-based residual network for salient object detection. *IEEE Transactions on Image Processing* 29:3763–3776.

Chen, Z., Q. Xu, R. Cong and Q. Huang. 2020. Global context-aware progressive aggregation network for salient object detection. *Proceedings of the AAAI Conference on Artificial Intelligence* 34(07):10599–10606.

De Boer, P. T., D. P. Kroese, S. Mannor and R. Y. Rubinstein. 2005. A tutorial on the cross-entropy method. *Annals of Operations Research* 134(1):19–67.

Deng, W., Q. Shi and J. Li. 2021. Attention-gate-based encoder–decoder network for automatic building extraction. *IEEE Journal of Selected Topics in Applied Earth Observations and Remote Sensing* 14:2611–2620.

Ferraioli, G. 2009. Multichannel InSAR building edge detection. *IEEE Transactions on Geoscience and Remote Sensing* 48(3):1224–1231.

Ghosh A, M. Ehrlich, S. Shah, L. Davis and R. Chellappa. 2018. Stacked u-nets for ground material segmentation in remote sensing imagery. Pages 257-261 in *Proceedings of the IEEE Conference on Computer Vision and Pattern Recognition Workshops*, held in Salt Lake City , United States, 18-22 June 2018. New York, United States: IEEE.

He, K., X. Zhang, S. Ren and J. Sun. 2016. Deep residual learning for image recognition. Pages 770–778 in *Proceedings of the IEEE Conference on Computer Vision and Pattern Recognition*, held in Las Vegas, United States, 26 June - 1 July 2016. New York, United States: IEEE.

He, S. and W. Jiang. 2021. Boundary-assisted learning for building extraction from optical remote sensing imagery. *Remote Sensing* 13(4):760.

Huang, G., Z. Liu, L. Van Der Maaten and K. Q. Weinberger. 2017. Densely connected convolutional networks. Pages 4700–4708 in *Proceedings of the IEEE Conference on Computer Vision and Pattern Recognition*, held in Hawaii, United States, 21-26 July 2017. New York, United States: IEEE.

Huang, H., L. Lin, R. Tong, H. Hu, Q. Zhang, Y. Iwamoto, X. Han, Y. Chen and J. Wu. 2020. UNet 3+: A full-scale connected UNet for medical image segmentation. Pages 1055–1059 in *ICASSP 2020-2020 IEEE International Conference on Acoustics, Speech and Signal Processing*, held in Barcelona, Spain, 4-9 May 2020. New York, United States: IEEE.

Ji, S., S. Wei and M. Lu. 2019. Fully convolutional networks for multisource building extraction from an open aerial and satellite imagery data set. *IEEE Transactions on Geoscience and Remote Sensing* 57(1):574–586.

Jin, Y., W. Xu, C. Zhang, X. Luo and H. Jia. 2021. Boundary-aware refined network for automatic building extraction in very high-resolution urban aerial images. *Remote Sensing* 13(4):692.

Krizhevsky, A., I. Sutskever and G. E. Hinton. 2017. ImageNet classification with deep convolutional neural networks. *Communications of the ACM 60(6):84-90.*

Lin, G., A. Milan, C. Shen and I. Reid. 2017. RefineNet: Multi-path refinement networks for high-resolution semantic segmentation. Pages 1925–1934 in *Proceedings of the IEEE Conference on Computer Vision and Pattern Recognition*, held in Hawaii, United States , 21-26 July 2017. New York, United States: IEEE.

Liu, H., J. Luo, B. Huang, X. Hu, Y. Sun, Y. Yang, N. Xu and N. Zhou. 2019. DE-Net: Deep encoding network for building extraction from high-resolution remote sensing imagery. *Remote Sensing* 11(20):2380.

Liu, P., X. Liu, M. Liu, Q. Shi, J. Yang, X. Xu and Y. Zhang. 2019. Building footprint extraction from high-resolution images via spatial residual inception convolutional neural network. *Remote Sensing* 11(7): 830.

Long, J., E. Shelhamer and T. Darrell. 2015. Fully convolutional networks for semantic segmentation. Pages 3431–3440 in *Proceedings of the IEEE Conference on Computer Vision and Pattern Recognition*, held in Boston, United States, 8-10 June 2015. New York, United States: IEEE.

Ma, K., Z. Shu, X. Bai, J. Wang and D. Samaras. 2018. DocUNet: Document image unwarping via a stacked U-Net. Pages 4700–4709 in *Proceedings of the IEEE Conference on Computer Vision and Pattern Recognition*, held in Salt Lake City, United States, 18-22 June 2018. New York, United States: IEEE.

Maggiori, E., Y. Tarabalka, G. Charpiat and P. Alliez. 2016. Fully convolutional neural networks for remote sensing image classification. Pages 5071–5074 in *IEEE International Geoscience and Remote Sensing Symposium* , held in Beijing, China, 10-15 July 2016. New York, United States:IEEE.

Maggiori, E., Y. Tarabalka, G. Charpiat and P. Alliez. 2017. Can semantic labeling methods generalize to any city? The Inria aerial image labeling benchmark. Pages 3226–3229 in *IEEE International Geoscience and Remote Sensing Symposium*, held in Fort Worth, United States, 23-28 July 2017. New York, United States : IEEE.

Newell, A., K. Yang and J. Deng. 2016. Stacked hourglass networks for human pose estimation. *European Conference on Computer Vision* pp. 483–499.

Ngo, T. T., V. Mazet, C. Collet and P. de Fraipont. 2016. Shape-based building detection in visible band images using shadow information. *IEEE Journal of Selected Topics in Applied Earth Observations and Remote Sensing* 10(3):920–932.

Oktay, O., J. Schlemper, L. L. Folgoc, M. Lee, M. Heinrich, K. Misawa, S. McDonagh, N. Y Hammerla, B. Kainz, B. Glocker and D. Rueckert. 2018. Attention U-Net: Learning where to look for the pancreas. Preprint, arXiv:1804.03999.

Qin, X., Z. Zhang, C. Huang, C. Gao, M. Dehghan and M. Jagersand. 2019. Basnet: Boundary-aware salient object detection. Pages 7479–7489 in *Proceedings of the IEEE/CVF Conference on Computer Vision and Pattern Recognition*, held in Long Beach, United States, 15-20 June 2019. New York, United States: IEEE.

Qin, X., Z. Zhang, C. Huang, M. Dehghan O. R. Zaiane and M. Jagersand. 2020. U2-Net: Going deeper with nested U-structure for salient object detection. *Pattern Recognition* 106:107404.

Ronneberger, O., P. Fischer and T. Brox. 2015. U-Net: Convolutional networks for biomedical image segmentation. Pages 234–241 in *International Conference on Medical Image Computing and Computer-Assisted Intervention*, held in Munich Germany, 5-9 October 2015. Berlin, Germany: Springer.

Shah, S., P. Ghosh, L. S. Davis and T. Goldstein. 2018. Stacked U-Nets: A no-frills approach to natural image segmentation. Preprint, arXiv:1804.10343.

Simonyan, K. and A. Zisserman. 2014. Very deep convolutional networks for large-scale image recognition. Preprint, arXiv:1409.1556.

Sirmacek, B. and C. Unsalan. 2008. Building detection from aerial images using invariant color features and shadow information. Pages 1–5 in *23rd International Symposium on Computer and Information Sciences*, held in Istanbul, Turkey, 27-29 October 2008. Berlin, Germany: Spinger.

Tang, Z., X. Peng, S. Geng,Y. Zhu and D. N. Metaxas. 2018. CU-Net: Coupled U-Nets. Preprint, arXiv:1808.06521.

Tian, Z., C. Shen, H. Chen and T. He. 2019. FCOS: Fully convolutional one-stage object detection. Pages 9627–9636 in *Proceedings of the IEEE/CVF International Conference on Computer Vision*, held in Seoul, Korea, 27 October-2 November 2019. New York, United States: IEEE.

Wang, Z., E. P. Simoncelli, and A. C. Bovik. 2003. Multiscale structural similarity for image quality assessment. Pages 1398–1402 in *37th Asilomar Conference on Signals*, *Systems and Computers* held in Pacific Grove, United States, 9-12 November 2003. New York, United States: IEEE.

Wu, G., X. Shao, Z. Guo, Q. Chen, W. Yuan, X. Shi, Y. Xu and R. Shibasaki. 2018. Automatic building segmentation of aerial imagery using multi-constraint fully convolutional networks. *Remote Sensing* 10(3):407.

Xie, S., R. Girshick, P. Dollár, Z. Tu and K. He. 2017. Aggregated residual transformations for deep neural networks. Pages 1492–1500 in *Proceedings of the IEEE Conference on Computer Vision and Pattern Recognition*, held in Hawaii, United States, 21-26 July 2017. New York, United States: IEEE.

Yang, X., J. Yang, J. Yan, Y. Zhang, T. Zhang, Z. Guo, X. Sun and K. Fu. 2019. SCRDet: Towards more robust detection for small, cluttered and rotated objects. Pages 8232–8241 in *Proceedings of the IEEE/CVF International Conference on Computer Vision*, held in Seoul, Korea , 27 October-2 November 2019. New York, United States: IEEE.

Zhang, S., H. Shen and C. Huo. 2017. Utilizing shape-based feature and discriminative learning for building detection. *IEICE Transactions on Information and Systems* 100(2):392–395.

Zheng, Z., Y. Zhong, J. Wang and A. Ma. 2020. Foreground-aware relation network for geospatial object segmentation in high spatial resolution remote sensing imagery. Pages 4096–4105 in *Proceedings of the IEEE Conference on Computer Vision and Pattern Recognition*, held in Seattle, United States, 13-19 June 2020. New York, United States: IEEE.

Zhong, S., J. Huang and W. Xie. 2008. A new method of building detection from a single aerial photograph. Pages 1219–1222 in *9th International Conference on Signal Processing*, held in Beijing, China, 26-29 October 2008. New York, United States: IEEE.

PE&RS 2023 Advertising Rates & Specs

THE MORE YOU ADVERTISE THE MORE YOU SAVE! *PE&RS* offers frequency discounts. Invest in a three-times per year advertising package and receive a 5% discount, six-times per year and receive a 10% discount, 12-times per year and receive a 15% discount off the cost of the package.

	Sustaining Member Exhibiting at a 2023 ASPRS Conference	Sustaining Member	Exhibitor	Non Member
All rates below are for four-color advertisments				
Cover 1	$1,850	$2,000	$2,350	$2,500

In addition to the cover image, the cover sponsor receives a half-page area to include a description of the cover (maximum 500 words). The cover sponsor also has the opportunity to write a highlight article for the journal. Highlight articles are scientific articles designed to appeal to a broad audience and are subject to editorial review before publishing. The cover sponsor fee includes 50 copies of the journal for distribution to their clients. More copies can be ordered at cost.

	Sustaining Member Exhibiting	Sustaining Member	Exhibitor	Non Member
Cover 2	$1,500	$1,850	$2,000	$2,350
Cover 3	$1,500	$1,850	$2,000	$2,350
Cover 4	$1,850	$2,000	$2,350	$2,500
Advertorial	1 Complimentary Per Year	1 Complimentary Per Year	$2,150	$2,500
Full Page	$1,000	$1,175	$2,000	$2,350
2 page spread	$1,500	$1,800	$3,200	$3,600
2/3 Page	$1,100	$1,160	$1,450	$1,450
1/2 Page	$900	$960	$1,200	$1,200
1/3 Page	$800	$800	$1,000	$1,000
1/4 Page	$600	$600	$750	$750
1/6 Page	$400	$400	$500	$500
1/8 Page	$200	$200	$250	$250
Other Advertising Opportunities				
Employment Promotion	$500 (30 day web + 1 email) $300 (30 day web)	$500 (30 day web + 1 email) $300 (30 day web)	$500 (30 day web + 1 email) $300 (30 day web)	$500 (30 day web + 1 email) $300 (30 day web)
Dedicated Content Email blast	$3000	$3000	$3000	$3000
Newsletter Display Advertising	1 Complimentary Per Year	1 Complimentary Per Year	$500	$500
PE&RS Digital Edition Announcement E-Mail	$1000	$1000	$1000	$1000

A 15% commission is allowed to recognized advertising agencies

Ad Size	Width	Height
Cover (bleed only)	8.625"	11.25"
Full Page (bleed)	8.625"	11.25"
Full Page (trim)	8.375"	10.875"
2/3 Page Horizontal	7.125"	6.25"
2/3 Page Vertical	4.58"	9.625"
1/2 Page Horizontal	7.125"	4.6875"
1/2 Page Vertical	3.4375"	9.625"
1/3 Page Horizontal	7.125"	3.125"
1/3 Page Vertical	2.29"	9.625"
1/4 Page Horizontal	7.125"	2.34"
1/4 Page Vertical	3.4375"	4.6875"
1/8 Page Horizontal	7.125"	1.17"
1/8 Page Vertical	1.71875"	4.6875"

- Publication Size: 8.375" × 10.875" (W x H)
- Live area: 1/2" from gutter and 3/8" from all other edges
- No partial page bleeds
- Publication Style: Perfect bound
- Printing Method: Web offset press
- Software Used: PC InDesign
- Supported formats:
  TIFF, EPS, BMP, JPEG, PDF, PNG
  PC InDesign, Illustrator,
  and Photoshop

Send ad materials to:
Rae Kelley
rkelley@asprs.org

Ship inserts to:
Alicia Coard
Walsworth
2180 Maiden Lane
St. Joseph, MI 49085
888-563-3220 (toll free)
269-428-1021 (direct)
269-428-1095 (fax)
alicia.coard@walsworth.com

Special Advertising Opportunities

FRONT COVER SPONSORSHIP

A *PE&RS* cover sponsorship is a unique opportunity to capture the undivided attention of your target market through three premium points of contact.

1— *PE&RS* FRONT COVER

(Only twelve available, first-come, first-served)
PE&RS is world-renowned for the outstanding imagery displayed monthly on its front cover—and readers have told us they eagerly anticipate every issue. This is a premium opportunity for any company, government agency, university or non-profit organization to provide a strong image that demonstrates their expertise in the geospatial information industry.

2— FREE ACCOMPANYING "HIGHLIGHT" ARTICLE

A detailed article to enhance your cover image is welcome but not a condition of placing an image. Many readers have asked for more information about the covers and your article is a highly visible way to tell your story in more depth for an audience keenly interested in your products and services. No article is guaranteed publication, as it must pass ASPRS editorial review. For more information, contact Rae Kelley at rkelley@asprs.org.

3— FREE TABLE OF CONTENTS COVER DESCRIPTION

Use this highly visible position to showcase your organization by featuring highlights of the technology used in capturing the front cover imagery. Limit 200-word description.

Terms: Fifty percent nonrefundable deposit with space reservation and payment of balance on or before materials closing deadline.

Cover Specifications: Bleed size: 8 5/8" × 11 1/4", Trim: 8 3/8" × 10 7/8"

PRICING

	Sustaining Member Exhibiting at a 2023 ASPRS Conference	Sustaining Member	Exhibitor	Non Member
Cover 1	$1,850	$2,000	$2,350	$2,500

Belly Bands, Inserts, Outserts & More!

Make your material the first impression readers have when they get their copy of *PE&RS*. Contact Bill Spilman at bill@innovativemediasolutions.com

VENDOR SEMINARS

ASPRS Sustaining Members now have the opportunity to hold a 1-hour informational session as a Virtual Vendor Seminar that will be free to all ASPRS Members wishing to attend. There will be one opportunity per month to reach out to all ASPRS Members with a demonstration of a new product, service, or other information. ASPRS will promote the Seminar through a blast email to all members, a notice on the ASPRS web site home page, and ads in the print and digital editions of *PE&RS*.

The Virtual Seminar will be hosted by ASPRS through its Zoom capability and has the capacity to accommodate 500 attendees.

Vendor Seminars	
Fee	$2,500 (no discounts)

DIGITAL ADVERTISING OPPORTUNITIES

EMPLOYMENT PROMOTION

When you need to fill a position right away, use this direct, right-to-the-desktop approach to announce your employment opportunity. The employment opportunity will be sent once to all ASPRS members in our regular Wednesday email newsletter to members, and will be posted on the ASPRS Web site for one month. This type of advertising gets results when you provide a web link with your text.

Employment Opportunity	Net Rate
30-Day Web + 1 email	$500/opportunity
Web-only (no email)	$300/opportunity

Do you have multiple vacancies that need to be filled? Contact us for pricing details for multiple listings.

NEWSLETTER DISPLAY ADVERTISING

Your vertical ad will show up in the right hand column of our weekly newsletter, which is sent to more than 3,000 people, including our membership and interested parties. **Open Rate: 32.9%**

Newsletter vertical banner ad	Net Rate
180 pixels x 240 pixels max	$500/opportunity

DEDICATED CONTENT EMAIL BLAST

Send a dedicated email blast to the ASPRS email list. Advertiser supplies HTML (including images). Lead time: 14 days.

Materials	Net Rate
Advertiser supplies HTML, including images.	$3000/ opportunity

PE&RS Digital Edition

Digital Edition Announcement E-Mail: 5,800+
PE&RS is available online in both a public version that is available to anyone but does not include the peer-reviewed articles, and a full version that is available to ASPRS members only upon login.

The enhanced version of *PE&RS* contains hot links for all ASPRS Sustaining Member Companies, as well as hot links on advertisements, ASPRS Who's Who, and internet references.
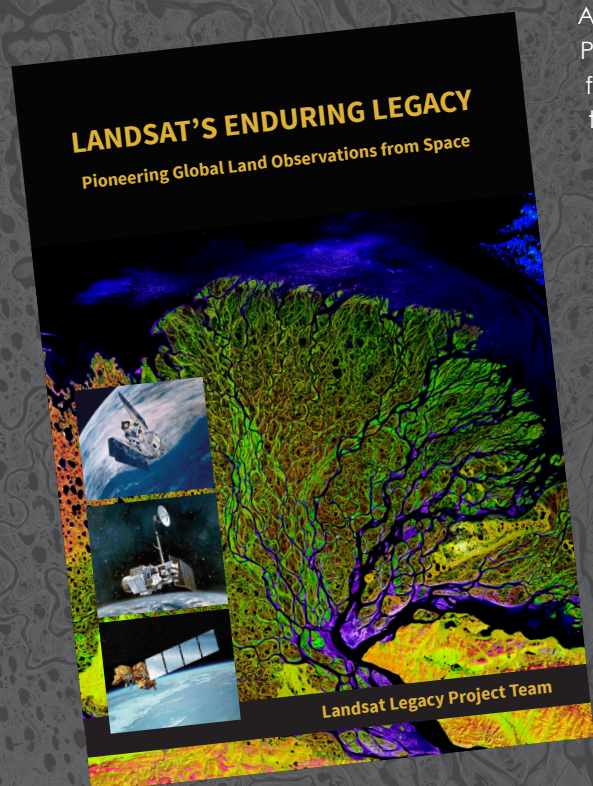
Become a sponsor today!
The e-mail blast sponsorship opportunity includes a **180 x 240 pixel ad** in the email announcement that goes out to our membership announcing the availability of the electronic issue.

Digital Edition Opportunities	Net Rate
E-mail Blast Sponsorship*	$1,000

LANDSAT'S ENDURING LEGACY
PIONEERING GLOBAL LAND OBSERVATIONS FROM SPACE

After more than 15 years of research and writing, the Landsat Legacy Project Team published, in collaboration with the American Society for Photogrammetry and Remote Sensing (ASPRS), a seminal work on the nearly half-century of monitoring the Earth's lands with Landsat. Born of technologies that evolved from the Second World War, Landsat not only pioneered global land monitoring but in the process drove innovation in digital imaging technologies and encouraged development of global imagery archives. Access to this imagery led to early breakthroughs in natural resources assessments, particularly for agriculture, forestry, and geology. The technical Landsat remote sensing revolution was not simple or straightforward. Early conflicts between civilian and defense satellite remote sensing users gave way to disagreements over whether the Landsat system should be a public service or a private enterprise. The failed attempts to privatize Landsat nearly led to its demise. Only the combined engagement of civilian and defense organizations ultimately saved this pioneer satellite land monitoring program. With the emergence of 21st century Earth system science research, the full value of the Landsat concept and its continuous 45-year global archive has been recognized and embraced. Discussion of Landsat's future continues but its heritage will not be forgotten.

The pioneering satellite system's vital history is captured in this notable volume on Landsat's Enduring Legacy.

Landsat Legacy Project Team

Samuel N. Goward

Darrel L. Williams

Terry Arvidson

Laura E. P. Rocchio

James R. Irons

Carol A. Russell

Shaida S. Johnston

Landsat's Enduring Legacy

Hardback. 2017, ISBN 1-57083-101-7

Member/Non-member $48*

Student Member $36*

* Plus shipping

Order online at
www.asprs.org/landsat

asprs — THE IMAGING & GEOSPATIAL INFORMATION SOCIETY

LEARN
DO
GIVE
BELONG

ASPRS Offers

» Cutting-edge conference programs

» Professional development workshops

» Accredited professional certifications

» Scholarships and awards

» Career advancing mentoring programs

» *PE&RS*, the scientific journal of ASPRS

asprs.org

ASPRS